

**Development and Characterization of Braze Repair Technology for  
Gas Turbine Hot Section Components**

by

**Thomas R. Henhoeffler, B.Eng.**

A thesis submitted to the Faculty of Graduate Studies and Research in partial fulfillment  
of the requirements for the degree of  
**Masters of Applied Science**

Ottawa-Carleton Institute for Mechanical and Aerospace Engineering

Department of Mechanical and Aerospace Engineering

Carleton University

Ottawa, Ontario

Canada

May 2008

©Thomas R. Henhoeffler, 2008



Library and  
Archives Canada

Bibliothèque et  
Archives Canada

Published Heritage  
Branch

Direction du  
Patrimoine de l'édition

395 Wellington Street  
Ottawa ON K1A 0N4  
Canada

395, rue Wellington  
Ottawa ON K1A 0N4  
Canada

*Your file* *Votre référence*  
*ISBN: 978-0-494-44043-8*  
*Our file* *Notre référence*  
*ISBN: 978-0-494-44043-8*

**NOTICE:**

The author has granted a non-exclusive license allowing Library and Archives Canada to reproduce, publish, archive, preserve, conserve, communicate to the public by telecommunication or on the Internet, loan, distribute and sell theses worldwide, for commercial or non-commercial purposes, in microform, paper, electronic and/or any other formats.

The author retains copyright ownership and moral rights in this thesis. Neither the thesis nor substantial extracts from it may be printed or otherwise reproduced without the author's permission.

**AVIS:**

L'auteur a accordé une licence non exclusive permettant à la Bibliothèque et Archives Canada de reproduire, publier, archiver, sauvegarder, conserver, transmettre au public par télécommunication ou par l'Internet, prêter, distribuer et vendre des thèses partout dans le monde, à des fins commerciales ou autres, sur support microforme, papier, électronique et/ou autres formats.

L'auteur conserve la propriété du droit d'auteur et des droits moraux qui protègent cette thèse. Ni la thèse ni des extraits substantiels de celle-ci ne doivent être imprimés ou autrement reproduits sans son autorisation.

---

In compliance with the Canadian Privacy Act some supporting forms may have been removed from this thesis.

Conformément à la loi canadienne sur la protection de la vie privée, quelques formulaires secondaires ont été enlevés de cette thèse.

While these forms may be included in the document page count, their removal does not represent any loss of content from the thesis.

Bien que ces formulaires aient inclus dans la pagination, il n'y aura aucun contenu manquant.

■ ■ ■  
**Canada**

## **Abstract**

Brazing is a joining process that is commonly used for the repair of gas turbine hot section components. Narrow and wide gap braze repair for cobalt-base superalloys X-40 with alternative nickel-base filler alloys were successfully developed and characterized, as outlined in this thesis. Narrow gap braze joints were found to contain a primary  $\gamma$ -Nickel phase with secondary eutectic phases and discrete carboborides. These secondary phases adversely affected the mechanical properties of the joint, particularly ductility. Isothermal heat treatment reduced the size and quantity of the secondary phases, improving the ductility. Prolonged exposure to high temperature in air however, caused a reduction in mechanical properties due to oxidation. Wide gap braze joints were also found to contain a primary  $\gamma$ -Nickel phase surrounded by secondary eutectic phases and discrete carboborides. The wide gap braze joints had comparable tensile properties to X-40 but performed poorly in high temperature fatigue testing due to the presence of small voids as a result of incomplete wetting of the IN-738 additive alloy powder particles by the braze alloy.

## **Acknowledgements**

- I must express my undying gratitude to my thesis supervisor Dr. Xiao Huang who provided me with unwavering support, guidance and a final nudge at the end to write a Master's Thesis in just over a month. Professor Huang is one of the most caring professors, not only at Carleton, but in all of academia. Thank you.
- I would also like to thank Dr. Donald Gauthier for making me comfortable with the idea of Master's research with a professor I had not had any previous relationship with. I would also like to thank Dr. Gauthier for not simply telling me, but showing me that there must be balance between work, play and family. Thank you.
- Thank you to all of the machinists, technologists, technicians and office staff of Carleton University's Mechanical and Aerospace Engineering Department, in particular Mr. Steve Truttman, master of the hydraulics. Thank you.
- I would like to thank the Department of Mechanical and Aerospace Engineering for the financial support I received throughout my master's research in the form of scholarships, teaching assistantships and research assistantships. Thank you
- I would like to thank Dr. Steen Sjolander for instilling in me the value of a vector graphic and a well prepared presentation. Dr. Sjolander taught me a great deal about project management and leadership in the two years I served the teaching assistant for his 4<sup>th</sup> year project, which happens to be the best TA assignment a grad student could ask for. Thank you.

- I would like to extend my gratitude to the staff at the National Research Council's Institute for Aerospace Research, Structures and Materials Performance Laboratory, namely the Materials Group in M-13. A substantial amount of this research was carried out at that facility and without the help of Scott Yandt, Peter Au, Dongyi Seo, Luc Lafluer, Olga Lupandina, Qi Yang, Dave Chow and Ryan MacNeil; this research would not have been possible. I would also like to thank the National Research Council for their financial contribution towards my research assistantship. Thank you.
- I would like to thank Liburdi Turbine Services Inc. for their work in kind on this project and the support they provided towards my research assistantship. A large amount of the sample preparation work was carried out at their facilities. Thank you.
- Thank you to my fellow grad students. Mr. Capurro, I am very glad you won the race, Mr. Bulmer, we will always have TurboExpo, ASM and those cheerful afternoons in the M-13 "student ghetto", Mr. Wisniewski, I am sorry my girlfriend tried to set you up with her friends and thanks for the boron nitride. Thank you.
- To my parents, Mark and Sheila Henhoeffler, I owe an enormous debt. If not for their encouragement and support I would not have made it this far (and I wouldn't be driving such a pretty car). And yes dad, "just because it looks good on paper, doesn't mean it is going to work." Thank you.

- Finally, Ashley, thanks for being Ashley. Your encouragement through the tough times, your smiling face in the good times, all those times you brought me dinner when working late, and let's not forget always putting up with my "grumpy pants." Without you I certainly would not have been able to do it. Look, you even get your own page! Thank you.

## Table of Contents

Abstract.....	i
Acknowledgements.....	ii
List of Tables .....	vii
List of Figures .....	ix
Chapter 1. Introduction .....	1
Chapter 2. Literature Review.....	4
2.1 Gas Turbines.....	4
2.1.1 Nozzle Guide Vanes .....	6
2.2 Gas Turbine Hot Section Materials .....	8
2.2.1 Nickel-base Superalloys .....	9
2.2.2 Cobalt-base Superalloys.....	10
2.2.3 Phases in Superalloys.....	12
2.2.4 IN-738 and X-40 Superalloys.....	17
2.3 Failure of Stationary Turbine Components.....	18
2.3.1 Thermal Fatigue .....	18
2.4 Repair of Superalloys.....	23
2.4.1 Fusion Welding Processes.....	24
2.4.2 Brazing Processes.....	29
2.4.3 Other Repair Processes.....	58
2.5 Joint Preparation and Formation .....	60
2.5.1 Joint Preparation.....	60
2.5.2 Joint Formation .....	60
2.6 Joint Characterization .....	65
2.6.1 Macroscopic Structure.....	65
2.6.2 Microstructure and Chemistry.....	67
2.6.3 Mechanical Properties .....	68
2.7 Summary .....	69
Chapter 3. Research Objectives.....	71
Chapter 4. Methodology.....	72
4.1 Research Materials.....	72
4.1.1 Superalloy Bars .....	72
4.1.2 Powders .....	72
4.1.3 Brazing Binder.....	73
4.2 Analytical Methods and Equipment.....	73
4.2.1 Brazing and Heat Treatment.....	73
4.2.2 Mechanical Testing Specimen Preparation .....	78

4.2.3	Mechanical Testing .....	80
4.2.4	Post Test Analysis.....	88
Chapter 5.	Experimental Results and Discussion .....	92
5.1	Baseline X-40 Bars .....	92
5.2	Narrow Gap Diffusion Brazing.....	95
5.2.1	As-Brazed Condition.....	95
5.2.2	Isothermally Exposed Condition .....	99
5.2.3	Microhardness Measurement .....	102
5.2.4	Tensile Properties .....	103
5.2.5	Examination of the Tensile Fracture Surfaces .....	106
5.2.6	Examination of the Tensile Fracture Surface Cross Sections.....	109
5.2.7	Oxidation During Isothermal Exposure.....	110
5.2.8	Summary of NGB Microstructure and Tensile Results .....	111
5.3	Wide Gap Diffusion Brazing .....	112
5.3.1	Microstructural Characteristics .....	112
5.3.2	Tensile Properties .....	126
5.4	Fatigue Testing .....	130
5.4.1	Fatigue Properties of WGB and NGB Joints.....	130
5.4.2	Fatigue Coupon Fractography.....	132
5.4.3	Summary of Fatigue Test Results.....	142
Chapter 6.	Conclusions and Recommendations for Future Work.....	143
6.1	Conclusions.....	143
6.2	Recommendations for Future Work .....	147
References	.....	149
Appendix A: Part Drawings	.....	154
Appendix B: Extensometer Calibration Report.....		158

## List of Tables

Table 2-1 - Effects of Major Alloying Elements in Nickel-Base Superalloys [19] .....	10
Table 2-2 - Function of Alloying Element Groups in Cobalt Superalloys, Adapted from [21] .....	11
Table 2-3 - Phases in Cobalt-Base Superalloys, Adapted from [22] .....	11
Table 2-4 - Isothermal Low Cycle Fatigue Results of X-40 Specimens [12] .....	23
Table 2-5 - Isothermal Low Cycle Fatigue Results of IN-738LC Specimens [12] .....	23
Table 2-6 - Comparison of Features in Welding and Brazing Repair [5] .....	30
Table 2-7 - Comparison of Different Braze Application Systems, Adapted from [5] .....	40
Table 2-8 - Brazing Temperature and Particle Size of Selected Commercial Braze Alloys	42
Table 2-9 - Tensile Test Results of WGB of X-40 Superalloy [36] .....	48
Table 2-10 - Composition of a Specific Braze Alloy System Used by Liburdi Turbine Services [49; 50; 51] .....	49
Table 2-11 - Selected Braze Alloys Used by GE for Repair of X-40 and FSX-414 [53; 54].	49
Table 2-12 - EDS Results of Commercial Pure Nickel Brazed With BNi-4 Braze Alloy [44]	50
Table 2-13 - Temperatures and Times of Brazing Experiments [55] .....	51
Table 2-14 - EDS Results of Centerline Eutectic Constituents in IN-738 Brazed With Nicrobraz 150 Presented By Chaturvedi et al. [56] .....	53
Table 2-15 - Compositional Analysis of the Phases Found in Braze of Pure Nicrobraz 150, shown in Figure 2-36 [57] .....	55
Table 2-16 - Compositional Analysis of Phases Found in Braze of 40/60 Ratio of Nicrobraz 150 / IN-738 Powder [57] .....	55
Table 4-1 - Nominal Composition of Alloys Used In This Study .....	72
Table 4-2 – Product Numbers of Alloy Powders Used in This Study .....	73
Table 4-3 - MultiPurpose TestWare Program Block Descriptions .....	87
Table 4-4 - Polishing Cloths used with Diamond and Silica Suspensions .....	90
Table 5-1 - Averaged EDS Results of Phases in X-40 Used in This Study (L, K and M Denote Energy level) .....	94

Table 5-2 - Microhardness of Various Phases in the Braze Region .....	103
Table 5-3 - Summary of High Temperature Tensile Test Results at 950°C.....	105
Table 5-4 - Averaged EDS Results and Representative EDS Spectrum of WGB with X-40 Additive Specimen Midbraze Eutectic Constituents (L, K and M Denote Energy level). 115	
Table 5-5 - Averaged EDS Results and Representative EDS Spectrum of Tungsten Boride Phase found at the X-40/Braze Interface in WGB with X-40 Additive Specimen (L, K and M Denote Energy level) .....	118
Table 5-6 - Average Nanohardness of Phases Observed in WGB joint with X-40 Additive .....	119
Table 5-7 - Averaged EDS Results and Representative EDS Spectrum of WGB with IN-738 Additive Specimen Midbraze Eutectics and Discrete Phases (L, K and M Denote Energy level).....	122
Table 5-8 - Average Nanohardness of Phases Observed in WGB joint with IN-738 Additive .....	125
Table 5-9 - WGB Tensile Test at 950°C Results.....	129

## List of Figures

Figure 2-1 - Gas Turbine Simple Cycle .....	5
Figure 2-2 - p-v and T-s Diagrams of the Idealized Brayton Cycle, Adapted from [14] .....	6
Figure 2-3 - Schematic of Temperature and Pressure Change Through a Gas Turbine Engine.....	7
Figure 2-4 – Nozzle Guide Vane and Turbine Blade Cooling Arrangement [16] .....	8
Figure 2-5 - Stress-Rupture Behaviours of Superalloy Classes, Adapted from [17] .....	9
Figure 2-6 - $\gamma'$ in IN-738 [23].....	13
Figure 2-7 – Carbides in IN-738 [23] .....	15
Figure 2-8 – Microstructure of TCP Phases in Austenitic Alloys, (A) Sigma Plates in U-500, (B) Sigma Plates in N-115, (C) Mu Plates Developing Near Degenerating MC Particle in AF-1753, (D) Laves Plates in S-590 with $M_6C$ , Scale Unknown, Adapted from [21] .....	17
Figure 2-9 - Microstructure of Cobalt-Base Superalloy X-40, Scale Unknown [22].....	18
Figure 2-10 - Terminology for High Temperature Fatigue [25] .....	19
Figure 2-11 - Thermal Fatigue Crack in a Nozzle Guide Vane [7] .....	20
Figure 2-12 - Cyclic Stress-Strain Plot for Elastic Behaviour, Adapted from [27] .....	21
Figure 2-13 - Cyclic Stress-Strain Plot for Elastic-Plastic Behaviour, Adapted from [27] .	21
Figure 2-14 - Fatigue Crack Propagation Across a Specimen Section, Adapted from [28] .....	22
Figure 2-15 – Cross-Section of a Fusion Weld Joint [29] .....	24
Figure 2-16 - Schematic of Manual GTAW Equipment [6].....	25
Figure 2-17 - Comparison of PTAW and GTAW Torch Designs [6] .....	27
Figure 2-18 - Schematic of Solid State (Nd:YAG) Laser [6] .....	28
Figure 2-19 - Semi-Automated Flame Brazing [32].....	31
Figure 2-20 - Induction Brazing Setup [32] .....	32
Figure 2-21 - Resistance Brazing Setup [32] .....	33
Figure 2-22 - Schematic of a Typical Dip Brazing Setup, Adapted from [34].....	34
Figure 2-23 - A Typical Continuous Brazing Furnace [32] .....	35

Figure 2-24 - A Typical Vacuum Furnace [34] .....	35
Figure 2-25 - Schematic of Braze Repair Process [2] .....	36
Figure 2-26 - Liquid Rise in a Narrow Capillary Gap, Adapted from [31] .....	38
Figure 2-27 – WGB Braze Alloy / Additive Alloy Configuration, Adapted from [9] .....	39
Figure 2-28 - Examples of Presintered Preforms [32].....	41
Figure 2-29 - The B-Co Phase Diagram [42] .....	43
Figure 2-30 - The B-Ni Phase Diagram [42].....	44
Figure 2-31 - Brazing Thermal Cycle (Time-Temperature), Adapted from [3; 5] .....	47
Figure 2-32 - Selected Braze Micrographs, Adapted from [55] .....	51
Figure 2-33 - Secondary Electron Micrograph of Centerline Eutectic Constituent in IN-738 Brazed with Microbraz 150 [56] .....	52
Figure 2-34 - Backscatter Electron Micrograph of Centerline Eutectic Constituent in IN-738 Brazed With Microbraz 150 [56].....	53
Figure 2-35 - Secondary Electron image of IN-738 Brazed with Microbraz 150 Showing Ni Rich Interface Boride Phase [56].....	53
Figure 2-36 - Microstructure of a Brazed Joint Produced by Pure Microbraz 150 [57] ....	54
Figure 2-37 - Microstructure of a Brazed Joint Consisting of 40/60 Ratio of Microbraz 150 / IN-738 Powder [57] .....	55
Figure 2-38 - Microstructures of Braze Joints With Different Gap Filler Contents (a) AMS 4777 Only, Brazing Temperature 1423 K, (b) AMS 4777 Only, Brazing Temperature 1523 K, (c) AMS 4777 +30% Additive, Brazing Temperature 1423 K, (d) AMS 4777 + 30% Additive, Brazing Temperature 1523 K [58] .....	56
Figure 2-39 - Effect of Additive Alloy and Brazing Temperature on Strength and Ductility of Braze Joint [58] .....	57
Figure 2-40 – Fracture Surfaces of Braze Joints With Different Gap Filler Contents (a) AMS 4777 Only, Brazing Temperature 1423 K, (b) AMS 4777 Only, Brazing Temperature 1523 K, (c) AMS 4777 +30% Additive, Brazing Temperature 1423 K, (d) AMS 4777 + 30% Additive, Brazing Temperature 1523 K [58] .....	58
Figure 2-41 - SEM Microstructure of a TLP Joint [61].....	59
Figure 2-42 - Surface and Interfacial Tensions Acting at the Periphery of a Sessile Drop Resting on a Horizontal Solid Substrate [31; 33; 34] .....	61

Figure 2-43 - Dissociation Pressures of Some Oxides, Adapted from [31] .....	64
Figure 2-44 - Ultrasonic Evaluation of as Cast 1 inch Square X-40 bar .....	66
Figure 2-45 - Creep Rupture Test at 980°C on Braze Repaired Crack in C1023, Adapted from [3] .....	69
Figure 4-1 - Vacuum Cast and Hot Isostatic Pressed X-40 Bars .....	72
Figure 4-2 - Narrow Gap Braze Test Specimen Manufacture Process, (a) Stainless Steel Shims Inserted, (b) Bars Tack Welded in Several Places and Shims Removed, (c) Bead of Braze Alloy Slurry Syringed Around Braze Gap.....	74
Figure 4-3 - X-40 Bar Cut for Slurry/Tape Insertion .....	74
Figure 4-4 - WGB X-40 Additive Specimen Prepared for Brazing .....	75
Figure 4-5 - Tape Casting Process .....	76
Figure 4-6 - WGB IN-738 Additive Specimen Prepared for Brazing.....	76
Figure 4-7 - NRC-IAR-SMPL Oxy-Gon Vacuum Furnace .....	77
Figure 4-8 - Braze Cycle.....	78
Figure 4-9 - Mechanical Testing Coupon Geometry .....	79
Figure 4-10 - Mitutoyo Digital Micrometer .....	80
Figure 4-11 - High Temperature Materials Testing Frame at Carleton University .....	80
Figure 4-12 - MTS TestStar IIs Control System at Carleton University .....	81
Figure 4-13 - High Temperature Mechanical Test Grip Assembly .....	82
Figure 4-14 - Furnace Automatic Shutoff Wiring Diagram .....	83
Figure 4-15 - Thermal Survey Coupon .....	84
Figure 4-16 - Stanford Research Systems Thermocouple Monitor .....	84
Figure 4-17 - LCF Test Loading Waveform .....	85
Figure 4-18 - MultiPurpose TestWare LCF Test Program .....	86
Figure 4-19 - Nikon SMZ1000 Stereoscope .....	88
Figure 4-20 - Buehler ISOMET 2000 Precision Saw.....	89
Figure 4-21 Struers LaboPress 3 Specimen Mounting Press .....	89

Figure 4-22 – Buehler ECOMET IV Polisher/Grinder.....	90
Figure 4-23 - Olympus PMG3 Optical Microscope.....	90
Figure 4-24 - LECO LM 247AT Microhardness Tester .....	91
Figure 4-25 – CMS Instruments Nano-Hardness Tester .....	91
Figure 5-1 - Phases of X-40 Bars Used In This Study.....	93
Figure 5-2 - Narrow Gap Braze Joint for Microstructural Examination.....	95
Figure 5-3 - Narrow Gap Braze Joint Showing Irregular Braze Region Between Two Substrate Materials.....	95
Figure 5-4 - (a) Narrow Gap Braze Joint, (b) Microstructure and Element Maps of the IN-738/Braze Interface, (c) EDS Spectrum of the Acicular Particle in the IN-738/Braze Interface, (d) Microstructure and Element Maps of the Braze Region, (e) Microstructure and Element Maps of the X-40/Braze Interface .....	99
Figure 5-5 - Microstructure of the Narrow Gap Braze Joint in the (a) As-Brazed Condition, and After Isothermal Heat Treatment at 950°C for (b) 120 hours, (c) 480 hours, (d) 840 hours – Red Arrows Indicate Carbides, Blue Arrows Indicate Eutectic Phases Surrounding the Primary $\gamma$ -Ni in the Braze Region .....	101
Figure 5-6 - (a) Narrow Gap Braze Region Between IN-738 and X-40 after 840-hour Heat Treatment at 950°C, (b) Microstructure and Element Maps for the IN-738/Braze Region Interface, (c) Microstructure and Element Maps for the Braze Region, (d) Microstructure and Element Maps for the X-40/braze interface .....	102
Figure 5-7 - NGB Tensile Properties.....	105
Figure 5-8 - Fracture Surfaces of Brazed Specimens in the As-Brazed and Heat Treated Conditions, (a) As-Brazed, (b) 120 hours, (c) 480 hours, (d) 840 hours – Arrows Indicate Intergranular Failure Locations.....	106
Figure 5-9 - Isothermal Tensile Test Fracture Surfaces of Narrow Gap Braze Specimens in the As-Brazed and Heat Treated Conditions, (a) As-Brazed Specimen Showing Mixed Mode IG and TG Fracture Modes, (b) 120 hour Heat Treated Sample Showing Predominantly TG Fracture Mode, (c) 480 hour Heat Treated Sample Showing Mixed TG and IG Fracture Modes, (d) 840 hour Heat Treated Sample Showing Mixed TG and IG Fracture Modes, Red Arrows Indicated IG Mode, Blue Arrows Indicated TG Mode .....	108
Figure 5-10 - Crack Initiation Within the Discrete Carbides (Blue Arrows) and Eutectic Phases Surrounding the Primary $\gamma$ -Ni Phase (Red Arrows).....	109
Figure 5-11 - IG Fracture in the As-Brazed Condition, (a) Optical, (b) SEM, Red Arrows Identify Eutectic Phases, Blue Arrows Identify Discrete Carbide Phases .....	110

Figure 5-12 - Cross Section of the Tensile Fracture Surface of Specimen Heat Treated for 840 hours at 950°C.....	110
Figure 5-13 - Cross Section of Tensile Fracture Surface of 840 hour Isothermally Exposed Narrow Gap Braze Specimen Illustrating Oxide Formation.....	111
Figure 5-14 - Regions of Interest in Wide Gap Braze Specimens .....	112
Figure 5-15 – Example of Porosity at the Midbraze of a WGB Joint with X-40 Additive	113
Figure 5-16 - Prominent Phases Found at Midbraze of WGB Specimen with X-40 Additive .....	114
Figure 5-17 - Midbraze Element Maps of WGB Specimen with X-40 Additive Alloy.....	116
Figure 5-18 - Prominent Phases at Interface of WGB Specimen with X-40 Additive .....	117
Figure 5-19 - Interface Element Maps of WGB Specimen with X-40 Additive .....	118
Figure 5-20 – Example of Porosity at the Midbraze of WGB with IN-738 Additive Alloy	120
Figure 5-21 - Prominent Phases Found at Midbraze of WGB with IN-738 Additive .....	121
Figure 5-22 - Midbraze Element Maps of WGB with IN-78 Additive.....	123
Figure 5-23 - Prominent Phases Found at Interface and in the Substrate of WGB Specimen with IN-738 Additive .....	124
Figure 5-24 - Interface Element Maps of WGB Specimen with IN-738 Additive.....	124
Figure 5-25 - Tensile Curves of WGB with X-40 Additive.....	127
Figure 5-26 - Cracking in WGB with X-40 Additive Alloy Tensile Tested Coupon.....	127
Figure 5-27 - Tensile Curves of WGB Joint, Tape Filled, IN-738 Additive .....	128
Figure 5-28 - Average WGB Tensile Test at 950°C Results .....	130
Figure 5-29 - WGB and NGB Fatigue Test Results .....	131
Figure 5-30 - Baseline X-40 Low Cycle Fatigue Coupon Fracture Surface .....	133
Figure 5-31 - Features of Baseline X-40 Low Cycle Fatigue Coupon Fracture Surface (A) Possible Initiation Site, (B) Fatigue Striations In High Crack Growth Region, (C) Cracking Between Eutectic Arms in Overload Region of Fracture Surface .....	134
Figure 5-32 - As-brazed Narrow Gap Braze Low Cycle Fatigue Coupon Fracture Surface .....	136

Figure 5-33 - Features of an As-brazed Narrow Gap Braze Low Cycle Fatigue Coupon Fracture Surface (A) Possible Initiation Site, (B) Exposed Eutectic in Overload Region of Fracture Surface, (C) Partially Unmelted Braze Alloy Powder Particles ..... 137

Figure 5-34 - WGB Joint With X-40 Additive Alloy Low Cycle Fatigue Coupon Fracture Surface ..... 138

Figure 5-35 - Initiation Site of WGB Joint with X-40 Additive Alloy Low Cycle Fatigue Coupon Fracture Surface ..... 139

Figure 5-36 - Fatigue Portion of WGB Joint with IN-738 Additive Alloy Low Cycle Fatigue Coupon Fracture Surface ..... 140

Figure 5-37 - Features of a WGB Joint with IN-738 Additive Alloy Low Cycle Fatigue Coupon Fracture Surface (A) Possible Initiation Site Showing Fatigue River Pattern, (B) Fatigue Striations Near High Crack Growth Rate Zone, (C) Secondary Cracking in High Crack Growth Zone, (D) Exposed Eutectic Pattern in Overload Region of Fracture Surface (not shown in overview image) ..... 141

## **Chapter 1. Introduction**

The development of cobalt-base superalloys came with the advent of the aircraft turbo-supercharger in the 1930s [1]. Currently, cobalt-base superalloys are used in gas turbine hot section components such as combustor casings, transition ducts and turbine vanes for both aerospace and industrial applications. These hot section components suffer damage as a result of thermal fatigue, creep, hot corrosion, erosion or a combination of these mechanisms [2; 3; 4; 5; 6]. When damaged components are removed from gas turbines at overhaul there is a significant opportunity for cost savings if they can be repaired, as the cost of hot section components can be substantial. Successful repair techniques can effectively double the life of hot section components at a cost of only 10 to 20% of a replacement part [7]. Due to the limited understanding of the properties of repaired components, repair is typically limited to static components, such as vanes, and low stress regions of rotating components, such as blade tips.

Unlike nickel-base superalloys, cobalt-base superalloys have reasonably good weldability and are traditionally repaired by fusion welding processes such as gas tungsten arc welding [2]. Fusion welding however has several limitations for repair of gas turbine hot section components. The available filler materials for fusion welding repair have, for the most part, inferior properties to that of the substrate, resulting in a joint that is weaker than the substrate. Also, the high heat input used for fusion welding causes distortion of the substrate and the formation of a heat affected zone of altered microstructure and inferior mechanical properties.

An alternative repair method to fusion welding is the brazing process. Brazing makes use of a braze alloy that is similar in composition to the substrate. This braze alloy is alloyed with melting point depressants such as boron or silicon which reduce the melting point of the braze alloy to below that of the substrate, allowing it to flow into capillary gaps, such as cracks, upon melting. Diffusion brazing occurs when the melting point depressants diffuse into the substrate, causing the braze alloy to solidify isothermally [8]. There are several advantages to braze repair over fusion welding repair. Brazing is a batch process which allows multiple components with multiple defects to be repaired during one brazing cycle. Thermal distortion does not occur in braze repair as the entire component is heated isothermally. Finally, braze joints of comparable tensile properties to that of the substrate can be achieved through proper alloy and process parameter selection [2].

Brazing processes can be designated as either narrow gap brazing, with braze gaps less than 200  $\mu\text{m}$  or wide gap brazing, with braze gaps greater than 200  $\mu\text{m}$ . In narrow gap brazing the braze alloy is applied to the substrate by means of a powder, paste or foil. The braze gap is typically limited to 200  $\mu\text{m}$  in narrow gap brazing because of brittle eutectic boride and silicide chains that can form at the centerline of the braze region with gaps of excessive width[2; 3]. These brittle centerline phases severely compromise the mechanical integrity of the joint. In wide gap brazing, an additive alloy with composition the same as or similar to that of the substrate is combined with the braze alloy. The additive alloy aids the capillary action of the braze alloy and can act as a diffusion sink for the melting point depressants, enhancing the bridgeability of the braze

alloy by reducing the occurrence of brittle boride or silicide. Wide gap diffusion brazing of superalloys was pioneered by Pratt and Whitney (TLP<sup>TM</sup> – transient liquid phase bonding) [5] and GE (ADH<sup>TM</sup> – activated diffusion healing) [9]. Other successful variations of wide gap braze repair have been developed by Liburdi Engineering Ltd. (LPM<sup>TM</sup> – Liburdi Powder Metallurgy)[10] and by Avco Lycoming (M-Fill<sup>TM</sup>) [11]. Despite the development of braze repair at various engine manufacturers, there is very little information available in the literature.

The purpose of this research is to develop and characterize a braze repair process for cobalt-base superalloy X-40 using alternative filler alloys. It is postulated that a wide gap braze scheme for X-40 implementing nickel-base IN-738 additive alloy with commercially available nickel-base ternary braze alloy BNi-9 will produce superior joints compared to joints made with X-40 additive alloy as the fatigue and creep properties of IN-738 are superior to those of X-40[12]. Braze joints were prepared and subsequently characterized to evaluate the microstructure and mechanical properties at elevated temperatures.

This thesis begins with a review of the relevant literature and background information in the areas of gas turbines, superalloys, thermal fatigue and gas turbine component repair in Chapter 2. The objectives of this research are explained in Chapter 3 followed by detailed information on the research materials and procedures used to generate the experimental results, in Chapter 4. The results of this research are presented and discussed in Chapter 5. Finally the conclusions drawn from this research and recommended future studies were presented in Chapter 6.

## **Chapter 2. Literature Review**

In this chapter, the repair of gas turbine nozzle guide vanes will be reviewed. The fundamentals of gas turbines and the environment to which nozzle guide vanes are exposed will be discussed, followed by an introduction to gas turbine hot section materials, namely superalloys. The failure modes experienced by stationary turbine components will be presented with emphasis on thermal fatigue followed by discussion of the techniques often used for gas turbine nozzle guide vane repair, and the methods of joint characterisation.

### **2.1 Gas Turbines**

A gas turbine is a rotary engine that extracts energy from the flow of combustion gases. Gas turbines can be divided into two categories, aeroengines and industrial gas turbines. Aeroengines are used to produce thrust and shaft rotation, while industrial engines are typically used for shaft rotation in power generation applications. Aeroengines are typically smaller, having a higher pressure ratio than industrial engines as weight is a prime concern for aircraft manufacturers. Gas turbine engines have high thrust-to-weight ratios, and in the case of industrial engines, high output power-to-size ratios, when compared to internal combustion engines. Advances in materials science and aerodynamics have led to turbine inlet temperatures surpassing 1650 K and pressure ratios over 35 [13]. These and other advances have led to thermal efficiencies approaching 40% for the simple cycle and 60% for combined cycles.

As shown in Figure 2-1, the two main components of a gas turbine engine are the compressor and turbine, which rotate on a common shaft. Air enters the simple cycle gas turbine engine at the inlet, travelling to the compressor where the pressure is raised, fuel is added to the compressed air and this mixture is ignited. The energy of the hot combustion gases is extracted in the turbine finally the combustion gases are exhausted. The energy that is extracted from the combustion gases by the turbine is greater than the energy required to compress the air in the compressor, the remaining energy can then be used to provide thrust through an expansion nozzle in the case of an aeroengine or rotate a shaft in the case of an industrial turbine.

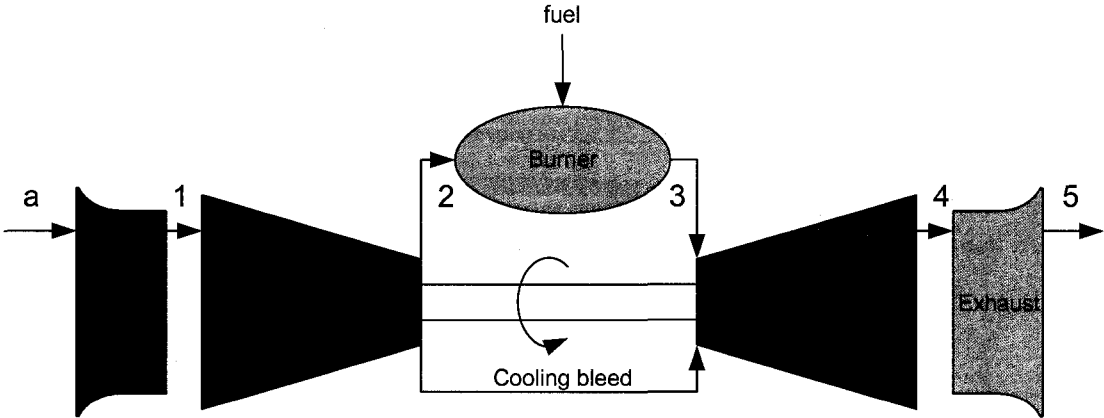


Figure 2-1 - Gas Turbine Simple Cycle

A simple cycle gas turbine is effectively a Brayton cycle, for which the idealized pressure-volume ( $p-v$ ) and temperature-entropy ( $T-s$ ) diagrams are shown in Figure 2-2. When applying the Brayton cycle model to a typical open cycle gas turbine engine, the connection between points 1 and 4 of Figure 2-2 are removed as these two points are open to the atmosphere.

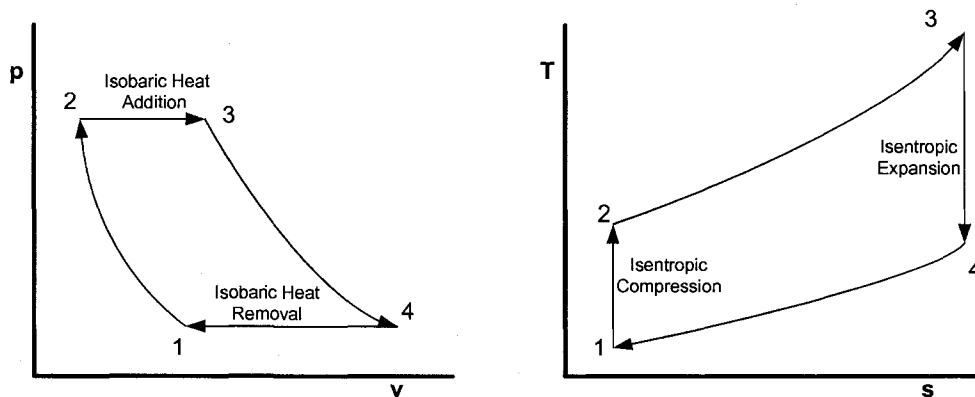


Figure 2-2 - p-v and T-s Diagrams of the Idealized Brayton Cycle, Adapted from [14]

Gas turbines can be comprised of a plethora of different components. Other than the main components, compressor, burner and turbine, there are inlets, exhausts, nozzles, shafts, bearings, ducting, gear boxes, generator, control systems and a wide range of auxiliary components.

### 2.1.1 Nozzle Guide Vanes

The conditions following combustion, at the entrance of the turbine are the harshest and most damaging to components. The maximum temperature in a gas turbine engine occurs at the entrance of the turbine and the pressure at this point is also near the maximum, as shown in Figure 2-3. Axial turbines have two types of airfoils, stators and rotors. The rotor is the portion of the turbine which moves, extracting energy from the high temperature and velocity combustion gases, rotating the shaft. The stator is designed to direct the flow into a favourable direction for the rotor, and as such is positioned upstream from the rotor. The first stage stator is often termed the nozzle guide vane (NGV), an example of which is shown in Figure 2-4. These NGVs are made of superalloys in modern gas turbines. For example, in the Rolls Royce T56 gas turbine

engine, which is used in many military cargo aircraft [15], the NGV is made of cobalt-base superalloy X-40.

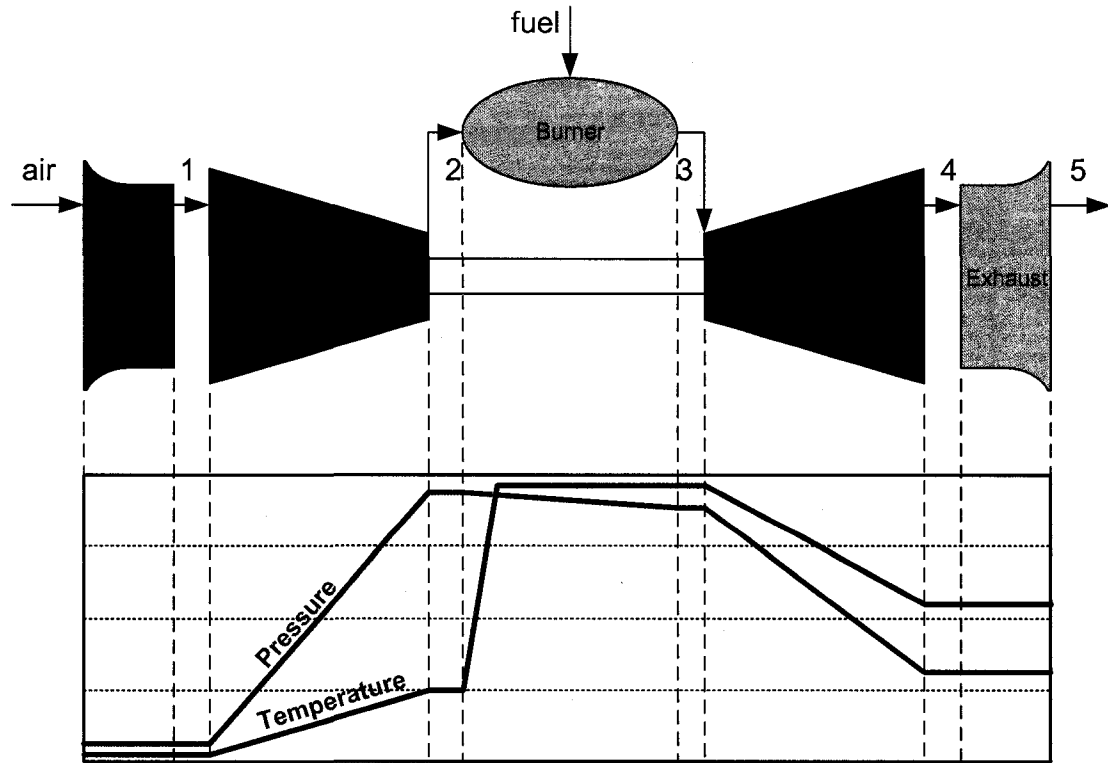


Figure 2-3 - Schematic of Temperature and Pressure Change Through a Gas Turbine Engine

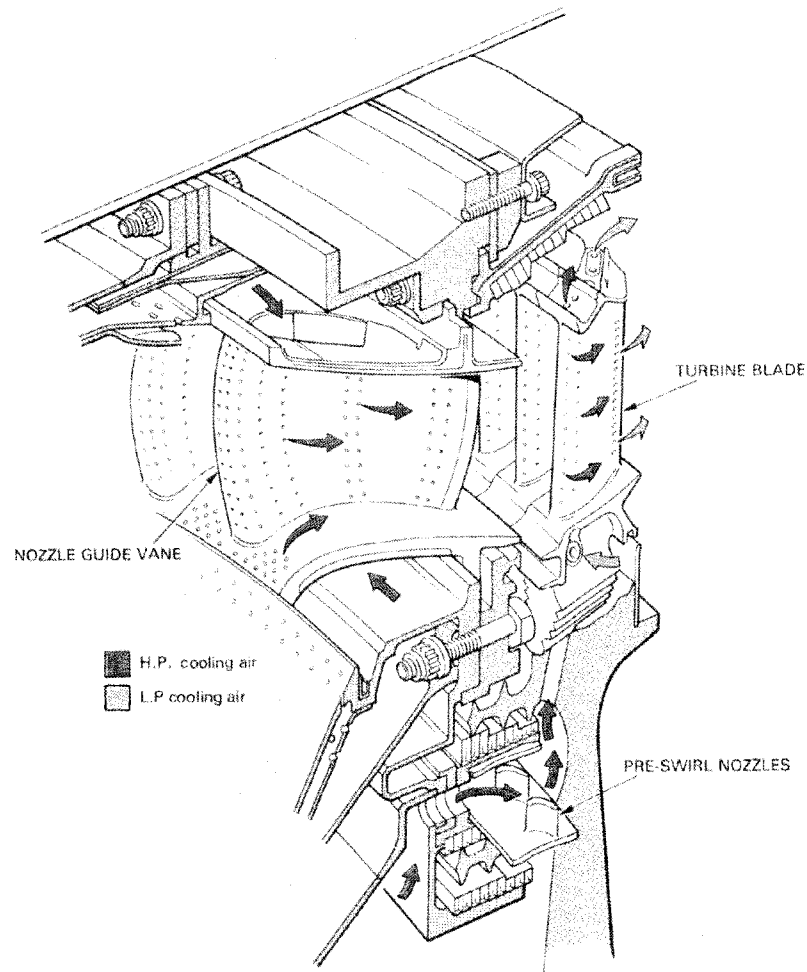


Figure 2-4 – Nozzle Guide Vane and Turbine Blade Cooling Arrangement [16]

## 2.2 Gas Turbine Hot Section Materials

Cobalt and nickel-base superalloys are a class of materials that are able to maintain their properties at elevated temperatures, making them ideally suited for gas turbine hot section applications. Superalloys can be specifically designed to provide high temperature strength, creep resistance, oxidation resistance and resistance to hot-corrosion. The microstructure and resulting properties of superalloys are highly dependent on the chemistry of the alloy, processing, final heat treatment, and service exposure. Cobalt and nickel-base superalloys may be wrought or cast, depending on the

application and composition required. As shown in Figure 2-5, a significant range of mechanical properties are available for superalloys at temperatures ranging from 650 to 1200°C.

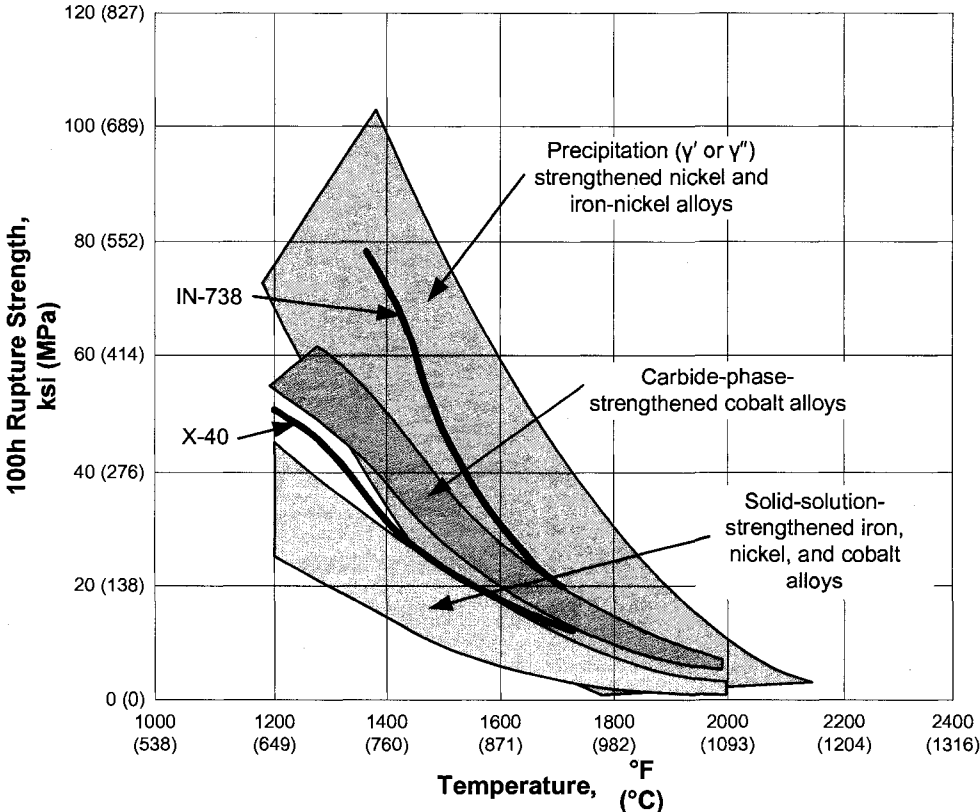


Figure 2-5 - Stress-Rupture Behaviours of Superalloy Classes, Adapted from [17]

**2.2.1 Nickel-base Superalloys**

The most commonly used superalloys in modern gas turbines are the nickel-base superalloys. Nickel-base superalloys are complex combinations of elements that have been carefully selected to achieve desired properties. The matrix of nickel-base superalloys is a face centered cubic (FCC) austenitic structure, commonly referred to as the gamma ( $\gamma$ ) phase, consisting mainly of nickel. In excess of ten different alloying elements are often added to achieve the desired mechanical and environmental properties [18], the effect of some important alloying elements are summarized in Table

2-1. Nickel-base superalloys are strengthened by a combination of solid solution strengthening, carbide precipitation and the precipitation of geometrically close packed phases gamma prime ( $\gamma'$ ) or gamma double prime ( $\gamma''$ ), depending on the alloy. Some earlier nickel-base alloys contained a significant amount of iron in the  $\gamma$  phase, these typically wrought alloys, termed nickel-iron-base superalloys.

**Table 2-1 - Effects of Major Alloying Elements in Nickel-Base Superalloys [19]**

	Matrix Strengthening	Increase in $\gamma'$ Volume Fraction	Grain boundaries	Other important effects
Cr	Moderate	Moderate	$M_{23}C_6$ and $M_7C_3$	Improves corrosion resistance, promotes TCP formation
Mo	High	Moderate	$M_6C$ and MC	Promotes TCP formation
W	High	Moderate		Promotes TCP formation
Ta	High	Large		
Nb	High	Large	NbC	
Ti	Moderate	Very large	TiC	
Al	Moderate	Very large		Improves oxidation resistance
Co	Slight	Moderate		
Re	Moderate			Retards coarsening
C	Moderate		carbides	
B Zr				Inhibit carbide coarsening, improve grain boundary strength, improve creep strength and ductility

### 2.2.2 Cobalt-base Superalloys

Structural cobalt-base superalloys generally consist of an FCC matrix that is hardened by carbide formations and solid solution strengthening. The chemistry of a cobalt-base superalloy is also quite complex, containing elements such as nickel, chromium, tungsten, titanium, zirconium, niobium, tantalum, molybdenum and carbon. The effects of these alloying elements on the microstructure of cobalt-base superalloys and the problematic effects associated with their excess additions are listed in Table 2-2, and the

phases found in several cobalt-base superalloys are listed in Table 2-3. No strengthening geometrically close packed intermetallic phase, such as the  $\gamma'$  phase in nickel-base superalloys, exist for cobalt-base superalloys. Regardless of the limited strength, cobalt-base superalloys have continued to find use for three main reasons [20]: (i) cobalt alloys exhibit higher melting temperatures which produces a flatter creep rupture curve and higher absolute temperature capabilities than nickel-base superalloys, (ii) cobalt-base superalloys provide superior hot corrosion resistance in gas turbine environments due to their higher chromium content, and (iii) cobalt-base superalloys exhibit superior weldability to nickel alloys. X-40, a cast cobalt-nickel-chromium-tungsten alloy, was invented by R.H. Thielemann in 1943. This alloy is still used in gas turbine vanes today and has acted as a model for newer generations of cobalt-base superalloys.

**Table 2-2 - Function of Alloying Element Groups in Cobalt Superalloys, Adapted from [21]**

Element	Principal Function	Problems When Added in Excess
Nickel	Austenite stabilizer	Lowers corrosion resistance
Chromium	Surface stability and carbide former	Forms TCP phases
Tungsten, Molybdenum	Solid solution strength	Forms TCP phases
Titanium, Zirconium, Tantalum, Niobium	Carbide formers	Harms surface stability
Carbon	Carbide formation	Decreases ductility

**Table 2-3 - Phases in Cobalt-Base Superalloys, Adapted from [22]**

Alloy Name or Trademark	Phases
X-40	$M_7C_3$ , $M_6C$ , $M_{23}C_6$
S-816	$M_{23}C_6$ , $Cb(C,N)$ , $M_6C$ , Laves
L-605	$M_6C$ , $M_{23}C_6$ , laves
MAR-M 509	$MC$ , $M_{23}C_6$ , $(Co,Cr,W)^*$
HA-188	$M_6C$ , $M_{23}C_6$ , Laves, La compound

\* Denotes complex intermetallic compound

## **2.2.3 Phases in Superalloys**

### ***2.2.3.1 Matrix and Solid Solution Strengthening***

Depending on the alloy system, the matrix of a superalloy can be Ni, Ni-Fe, or Co. The matrix is strengthened by the addition of solid solution elements. The majority of solid solution strengthening in both nickel- and cobalt-base superalloys is achieved by refractory elements tungsten, molybdenum and chromium. Tantalum, niobium, zirconium and hafnium are also used for solid solution strengthening, however their effectiveness as solid solution strengtheners is hampered significantly because they are strong carbide-formers. Elements in solid solution impart benefits to the alloy other than strengthening, chromium for example provides hot-corrosion and oxidation resistance, nickel and cobalt stabilize the FCC matrix, eliminating any dimensional and mechanical property variations associated with the hexagonal close-packed (HCP) transformation.

### ***2.2.3.2 $\gamma'$ and $\gamma''$ Strengthening***

Gamma prime ( $\gamma'$ ) is the principal strengthening phase for nickel-base superalloys. The  $\gamma'$  phase forms as a precipitate phase which is often coherent with the  $\gamma$ -matrix, an example is shown in Figure 2-6. This precipitate has the general chemical formula  $\text{Ni}_3(\text{Al,Ti})$  though other elements, namely niobium, tantalum and chromium also enter  $\gamma'$ .  $\gamma'$  also forms films along grain boundaries in some wrought and cast nickel alloys, which is believed to be beneficial to creep rupture properties [17]. Nickel-iron superalloys are often strengthened by the gamma double prime ( $\gamma''$ ), in which nickel and niobium combine in the presence of iron to form  $\text{Ni}_3\text{Nb}$ , a phase which is, like the  $\gamma'$

precipitate, coherent with the  $\gamma$  matrix.  $\gamma''$  however only provides strength in the low to intermediate temperatures as it is unstable at temperatures above 649°C (1200°F) [17]. The intermetallic compounds that exist in the cobalt-base system do not offer the same extent of strengthening as the  $\gamma'$  precipitate.

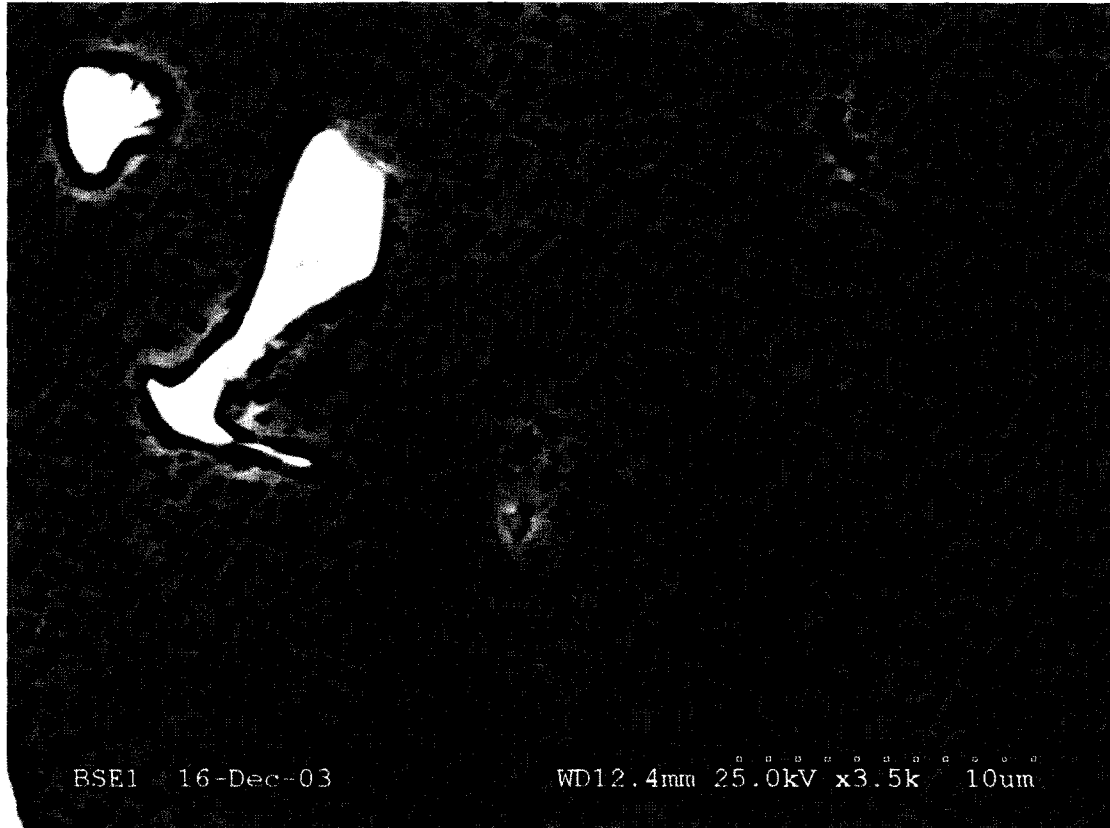


Figure 2-6 -  $\gamma'$  in IN-738 [23]

### 2.2.3.3 Carbides and Borides

FCC carbides are found in virtually all types of superalloy. In cobalt-base superalloys, carbide precipitation is the primary strengthening mechanism. Carbides have a number of morphologies including globular, blocky and script, and tend to precipitate on the grain boundaries of the matrix phase. Carbon and boron combine with reactive elements such as chromium, titanium, tantalum, hafnium, and niobium to form metal

carbides and borides such as MC,  $M_3C_2$ ,  $M_6C$ ,  $M_7C_3$ ,  $M_{23}C_6$ , and  $M_3B_2$  where M represents one or more metal atom. The carbides that form in superalloys can essentially be divided into two groups, chromium rich and refractory rich carbides.  $M_3C_2$ ,  $M_7C_3$ , and  $M_{23}C_6$  carbides are basically chromium carbides, also containing cobalt, tungsten or molybdenum in substitution of chromium [22].  $M_6C$  and MC carbides are typically refractory rich carbides that find use for strengthening both wrought and investment cast nickel-base alloys.

In nickel-base systems, MC carbides form most readily but can decompose to  $M_{23}C_6$  and  $M_6C$  carbides during heat treatment or in service. It has been observed that the MC carbide, which is typically rich in titanium, tantalum and hafnium (as they are strong carbide formers), precipitates at high temperatures from the liquid phase and consequently these carbides can be found in interdendritic regions with no distinct orientation relationship with the matrix [18].  $M_{23}C_6$  forms at lower temperatures (approximately 750°C) during retracted periods of service exposure and has been attributed to the breakdown of the MC carbides [18].  $M_6C$  carbides are usually found in low chromium content alloys which have molybdenum and tungsten levels 4 at% and higher [20]. An example of carbides in a nickel-base superalloy is shown in Figure 2-7.

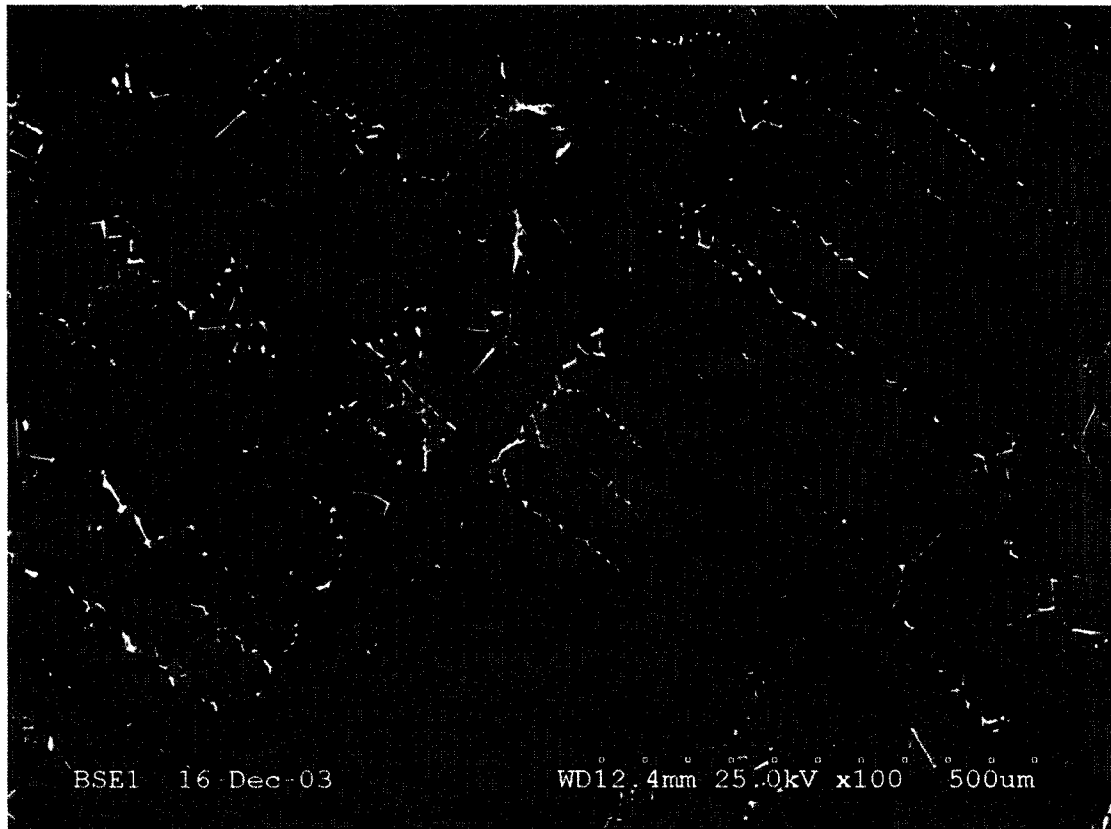


Figure 2-7 – Carbides in IN-738 [23]

In cobalt-base systems, higher chromium-to-carbon ratios favour  $M_{23}C_6$  formation while lower ratios favour  $M_7C_3$  [22].  $M_{23}C_6$  carbides in cobalt-base superalloys have been found to have the atomic formula  $Cr_{17}Co_4W_2C_6$  [20] and have been found in the interdendritic region in most commercial alloys though its primary role is as a secondary precipitate particle throughout the matrix. MC carbides are an extremely important in strengthening of cobalt-base alloys, even more so when combined in the right proportions with  $M_{23}C_6$  carbides. MC carbides tend to form with hafnium, zirconium, tantalum, niobium and titanium and generally have a discreet blocky shape.

#### **2.2.3.4 TCP Phases**

The addition of certain elements in excess can lead to the formation of undesirable topologically close packed (TCP) phases. The chemistry of superalloys however is typically chosen to avoid the formation of TCP phases. TCP phases, which usually have a plate or needle like structure [17], can cause a loss of mechanical properties if present in more than trace amounts. These TCP phases form when the solubility limit of the austenitic matrix is exceeded [20], this is primarily caused by excessive addition of chromium and other elements such molybdenum, tungsten and rhenium. In general, TCP phases have the chemical formula  $A_xB_y$ , where A and B are both transition metals, some examples include the sigma ( $\sigma$ ), mu ( $\mu$ ) and Laves phases. The  $\mu$  phase for example has the ideal stoichiometry  $A_6B_7$  and a rhombohedral cell containing 13 atoms (i.e.,  $W_6Co_7$  and  $Mo_6Co_7$ ) while the  $\sigma$  phase has the ideal stoichiometry  $A_2B$  and a tetragonal cell containing 30 atoms (i.e.,  $Cr_2Ru$ ,  $Cr_{61}Co_{39}$  and  $Re_{67}Mo_{33}$ ) [18]. Some examples of the TCP phases found in superalloys are shown in Figure 2-8.

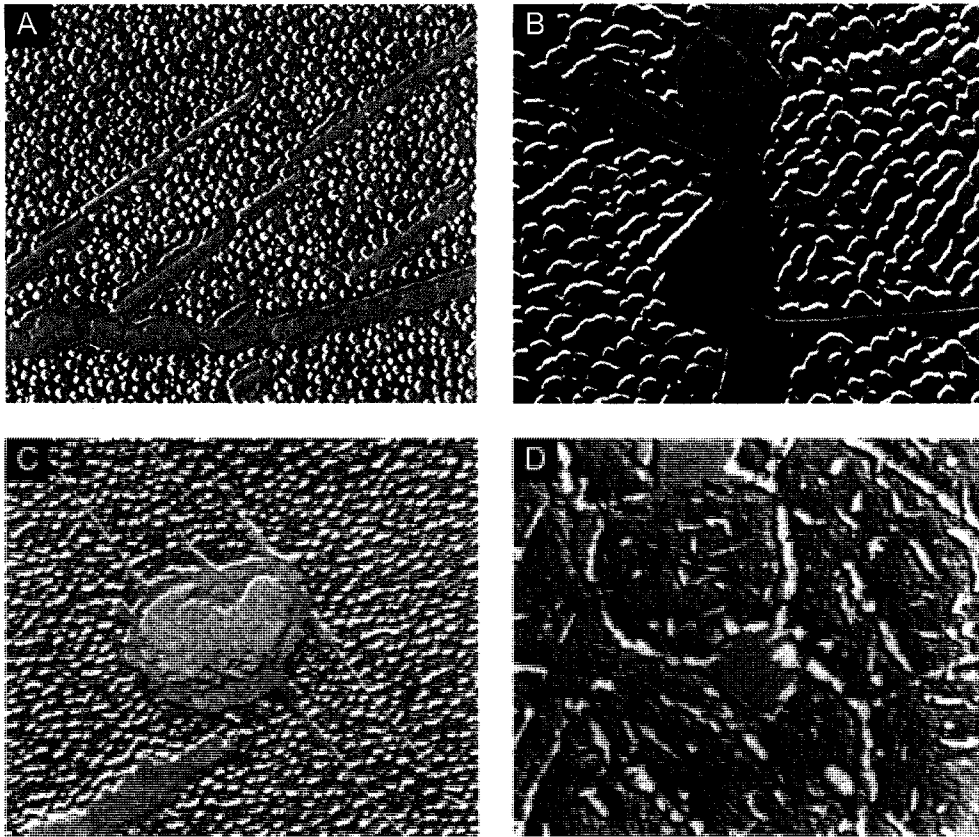


Figure 2-8 – Microstructure of TCP Phases in Austenitic Alloys, (A) Sigma Plates in U-500, (B) Sigma Plates in N-115, (C) Mu Plates Developing Near Degenerating MC Particle in AF-1753, (D) Laves Plates in S-590 with  $M_6C$ , Scale Unknown, Adapted from [21]

#### 2.2.4 IN-738 and X-40 Superalloys

Inconel 738 (IN-738) is a nickel-base superalloy which is widely used for gas turbine hot section components. IN-738 is strengthened by  $\gamma'$  and MC carbides within the  $\gamma$  matrix, the morphologies of which are shown in Figure 2-6 and Figure 2-7 respectively. Polycrystalline IN-738 in the aged condition usually contains between 40-45 vol.%  $\gamma'$  while single crystal superalloys such as CMSX-2 and PWA 1484 contain high  $\gamma'$  volume fractions (60-80%) [24].

As stated earlier, X-40 is a cobalt-base superalloy which has been used extensively in the past and is still used today for the stationary gas turbine hot section components. X-40 has good oxidation resistance, thermal shock resistance, and fatigue life. The

microstructure of X-40, shown in Figure 2-9, consists of a  $\gamma$  matrix strengthened mainly by the  $M_{23}C_6$  carbide which forms plates interlaid in the matrix.

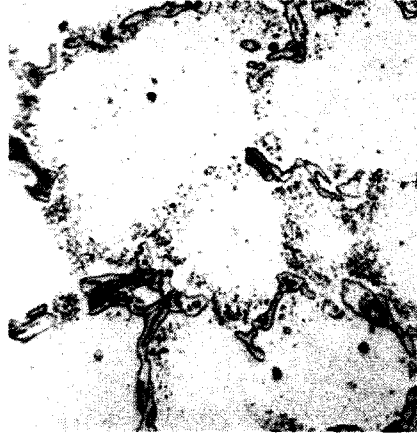


Figure 2-9 - Microstructure of Cobalt-Base Superalloy X-40, Scale Unknown [22]

## 2.3 Failure of Stationary Turbine Components

During operation, several factors can degrade the function of engine components, such as low cycle fatigue, creep, distortion, corrosion, erosion, fretting and foreign object damage [2; 3; 4; 5]. In static components, low cycle fatigue is caused by the rapid changes in the temperature of turbine components due to the rapid power changes produced during start/stop cycles, termed thermal fatigue [4]. Thermal fatigue will be the focus of the following section as it is the leading cause of stationary component failure.

### 2.3.1 Thermal Fatigue

The definition of thermal fatigue has been given by Spera [25] as “the gradual deterioration and eventual cracking of a material by alternate heating and cooling during which free thermal expansion is partially or completely constrained.” This situation presents itself in the normal operation of gas turbines, especially in the hot section of those used for aircraft propulsion. As shown in Figure 2-10, thermal fatigue is

classified under the general heading of high temperature low cycle fatigue because cracking typically starts in less than 50,000 cycles and a thermal cycle typically has significant inelastic strain. The loading in a thermal fatigue process can be either external, termed thermal-mechanical fatigue or internal, termed thermal-stress fatigue [26]. The external load in thermal-mechanical fatigue is applied by boundary forces to the surfaces of the object being heated or cooled. The internal load in thermal-stress fatigue is produced by rapid heating and cooling, usually with a working fluid, which produces large thermal gradients which in turn produce thermal stresses in the component. An example of a typical thermal fatigue crack is shown in Figure 2-11.

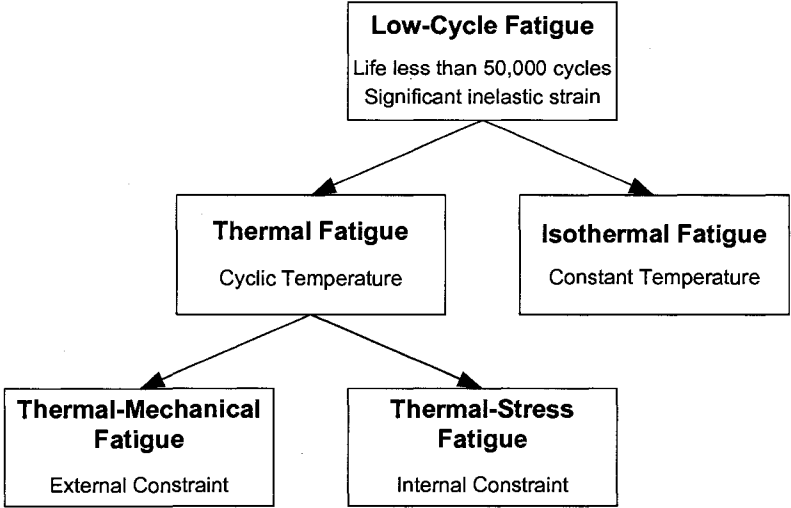


Figure 2-10 - Terminology for High Temperature Fatigue [25]

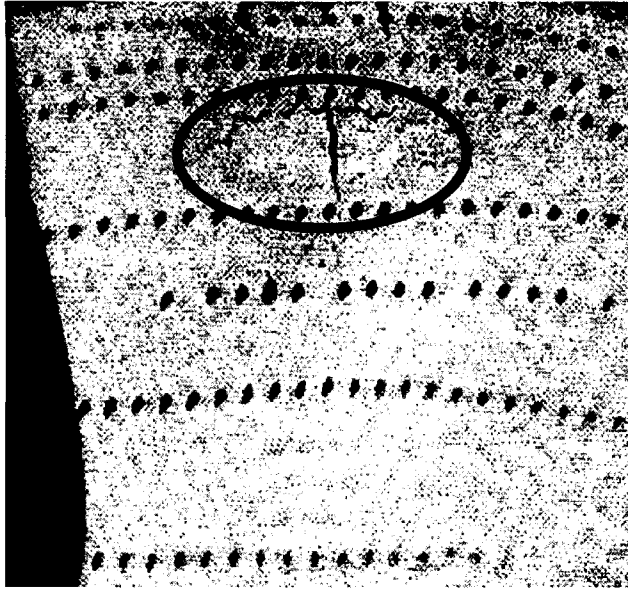


Figure 2-11 - Thermal Fatigue Crack in a Nozzle Guide Vane [7]

### ***2.3.1.1 Cyclic Loading and the Hysteresis Loop***

The hysteresis loop is the most convenient way to describe a material's behaviour when subjected to cyclic loading. When a material is cyclically loaded in the elastic range, the plotting of stress versus the strain produces a hysteresis loop that appears as a straight line, as shown in Figure 2-12 with  $\sigma$  representing stress and  $\epsilon$  representing strain. When the same axis is used to represent a material undergoing the elastic plastic range of cyclic loading, a loop of similar overall shape to that shown in Figure 2-13 is produced. The area inside this loop is the work done, or energy lost per during the loading cycle that the loop represents.

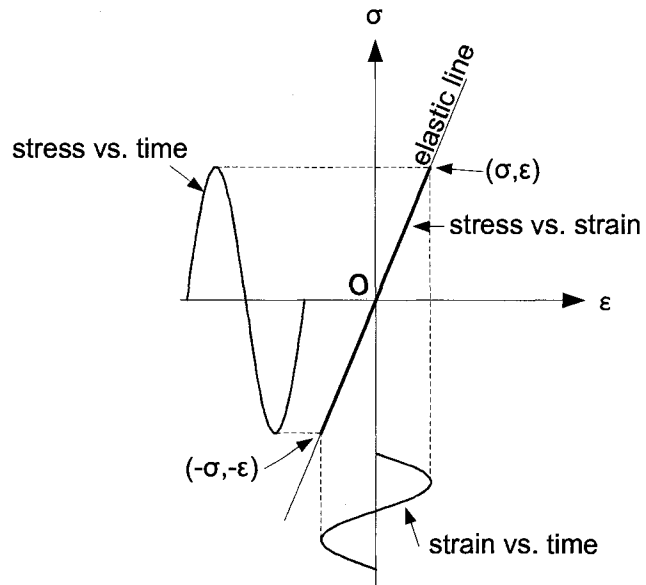


Figure 2-12 - Cyclic Stress-Strain Plot for Elastic Behaviour, Adapted from [27]

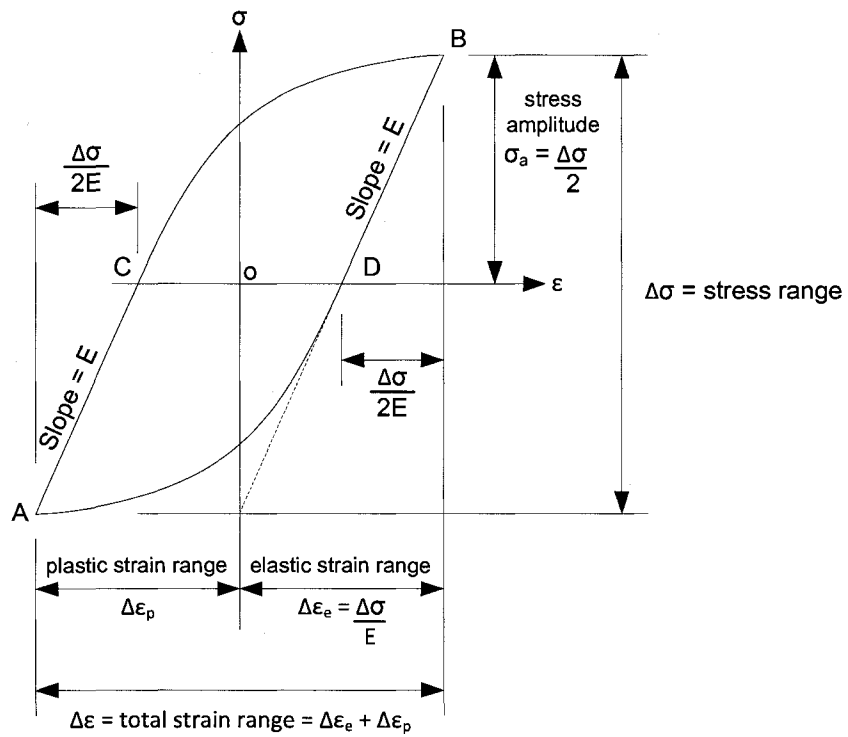


Figure 2-13 - Cyclic Stress-Strain Plot for Elastic-Plastic Behaviour, Adapted from [27]

### 2.3.1.2 Fatigue Crack Growth

As shown in Figure 2-14, as a fatigue crack progresses through a specimen, three stages of crack growth are encountered. During crack initiation, denoted Stage I in Figure 2-14, the crack advances on a microscale, based on the grain size. During crack growth, denoted Stage II in Figure 2-14 the crack grows at a much higher rate usually normal to the maximum applied tensile stress. The crack growth stage typically covers most of the fracture surface and the crack path is generally not heavily influenced by material discontinuities. Overload, denoted Stage III in Figure 2-14, is analogous to ductile tearing in simple tensile crack growth. The proportion of the fracture surface produced by Stages I through III vary with material and loading conditions. In low-cycle fatigue, Stage II dominates while in high cycle fatigue, Stage I dominates.

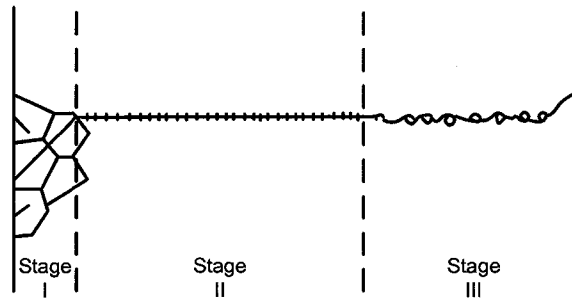


Figure 2-14 - Fatigue Crack Propagation Across a Specimen Section, Adapted from [28]

### 2.3.1.3 LCF of X-40 and IN-738

Some examples of isothermal low cycle fatigue test results for cobalt-base superalloy X-40 can be seen in Table 2-4 and results for nickel-base superalloy IN 738LC (low carbon grade) in Table 2-5. By comparing these two tables, where  $\Delta\varepsilon_t$  is the total strain range,  $N_f$  is the cycles to failure,  $\Delta\varepsilon_p$  is the plastic strain range and  $\sigma_a$  is the stress amplitude, it

can be seen that IN-738 has a superior high temperature low cycle fatigue resistance compared to X-40.

**Table 2-4 - Isothermal Low Cycle Fatigue Results of X-40 Specimens [12]**

Temp (°C)	$\Delta\varepsilon_t$ (%)	Cycles to Failure, $N_f$	$\Delta\varepsilon_p$ (%) @ $N_f/2$	$\sigma_a$ (MPa) @ $N_f/2$
980	0.235	20350	0.027	150
980	0.264	2860	0.08	162
980	0.400	1770	0.17	185
800	0.240	Run out @ 100000	0.006	185
800	0.344	7700	0.064	234
800	0.504	3980	0.165	275

**Table 2-5 - Isothermal Low Cycle Fatigue Results of IN-738LC Specimens [12]**

Temp (°C)	$\Delta\varepsilon_t$ (%)	Cycles to Failure, $N_f$	$\Delta\varepsilon_p$ (%) @ $N_f/2$	$\sigma_a$ (MPa) @ $N_f/2$
980	0.30	16520	0.009	209
980	0.40	2500	0.015	284
980	0.64	300	0.086	400
850	0.60	2700	0.02	505
850	0.648	2100	0.025	536
850	0.80	600	0.12	597
850	0.80	800	0.09	615
850	0.89	500	0.11	692
850	1.00	125	0.325	555

## 2.4 Repair of Superalloys

As previously mentioned, gas turbine hot section components, particularly vanes, are subject to severe loading conditions. Damage caused to these components requires replacement or repair. There are many processes currently used for repair of the hot section turbomachinery of gas turbine engines. Historically, fusion welding processes have been the most widely used, many superalloys are however unweldable with conventional fusion welding processes and must be repaired by other processes such as

brazing. In the following sections the main repair processes will be described, with emphasis on diffusion brazing.

**2.4.1 Fusion Welding Processes**

Fusion welding processes are the most important and widely used technique for joining metals. The cobalt-base superalloys found in many NGVs have reasonably good weldability and are usually repaired by tungsten inert gas (TIG) or plasma transferred arc (PTAW) welding [2]. Three types of heat sources are used for fusion welding processes, high-intensity combustion of gases, localized high-current electric discharges (arc welding) and more recently, laser beams. Gas combustion welding is typically unacceptable for joining of superalloy components as it introduces contamination. As shown in Figure 2-15, following fusion welding distinct regions can be identified. The fusion zone is the region in which filler metal was applied during the welding process. The heat affected zone (HAZ) is the region of the substrate that was microstructurally altered by the heat used to form the fusion zone; this microstructural change typically causes deterioration in the mechanical properties of the HAZ.

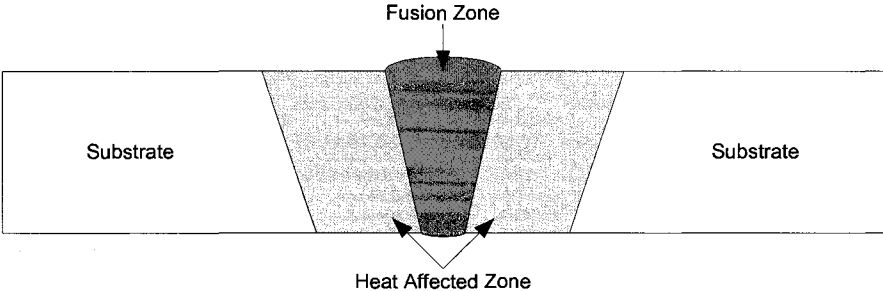


**Figure 2-15 – Cross-Section of a Fusion Weld Joint [29]**

### 2.4.1.1 Gas Tungsten Arc or Tungsten Inert Gas Welding

Gas tungsten arc welding (GTAW), also referred to as tungsten inert gas (TIG) welding is a process that is well suited for repair of thin sections because the heat input is highly localized and controllable [6]. The localized heat used to join materials is produced by passing an electric current through a non-consumable electrode made of tungsten or tungsten alloy, into the work piece. The electrode does not contact the work piece (except to create the initial arc) but the electricity passes through a shielding gas of argon or helium by ionization. Use of shielding gas is essential, as it protects the weld pool from contaminants. One of the main benefits of GTAW/TIG is that the welding equipment is readily available and relatively inexpensive. The damage found in airfoil sections is random in size, shape and location and therefore almost all repairs by GTAW/TIG are done manually [6].

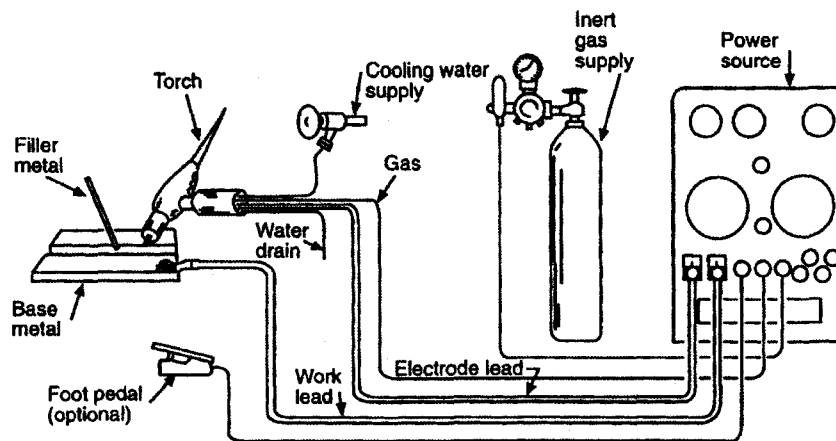


Figure 2-16 - Schematic of Manual GTAW Equipment [6]

There are several advantages to GTAW. When properly maintained, the shielding gas environment prevents the formation of refractory oxides in superalloys containing aluminum or titanium [6]. The heat input can be accurately controlled, and with pulsing

current inputs it is possible to reduce distortion in the component being welded [6]. A highly skilled operator can repair the very thin sections often encountered in a gas turbine airfoils using small diameter filler wires with compositions compatible with the base material. There are however disadvantages to this process, namely, GTAW is a relatively slow process and consumption of the tungsten electrode can contaminate the weld pool, resulting in a discontinuous weld and loss of strength and corrosion resistance. A high level of operator skill is required for this process since both the welding torch and filler metal (usually rod or wire) must be manipulated simultaneously. Unfortunately, due to the very strict manufacturing tolerances in place for gas turbine components, high reject rates are often experienced when using manual or simple automation systems with GTAW/TIG welding due to the distortion introduced during welding.

#### ***2.4.1.2 Plasma Transferred Arc Welding (PTAW)***

Plasma (or microplasma) transferred arc welding (PTAW) is similar to GTAW in that they both produce heat by ionizing an inert gas and both processes make use of tungsten or tungsten alloy electrodes. The fundamental difference between the two processes is that in PTAW the arc is constricted by an orifice assembly that surrounds the electrode. This arc constriction results in a more localized heat input which can reduce distortion and the HAZ size. Because of the higher heat input, PTAW torches are always water cooled. PTAW torches require two separate gas streams. The inner stream, or orifice gas, surrounds the electrode, constricting the arc to form an extremely hot plasma jet. The outer stream, or shield gas, surrounds the weld pool, protecting it from

contamination. The orifice gas is always argon and the shielding gas is usually a mixture of argon and helium. The purity of both gases is essential to prevent contamination of the weld pool [6]. The main differences between the GTAW and PTAW torches are shown in Figure 2-17.

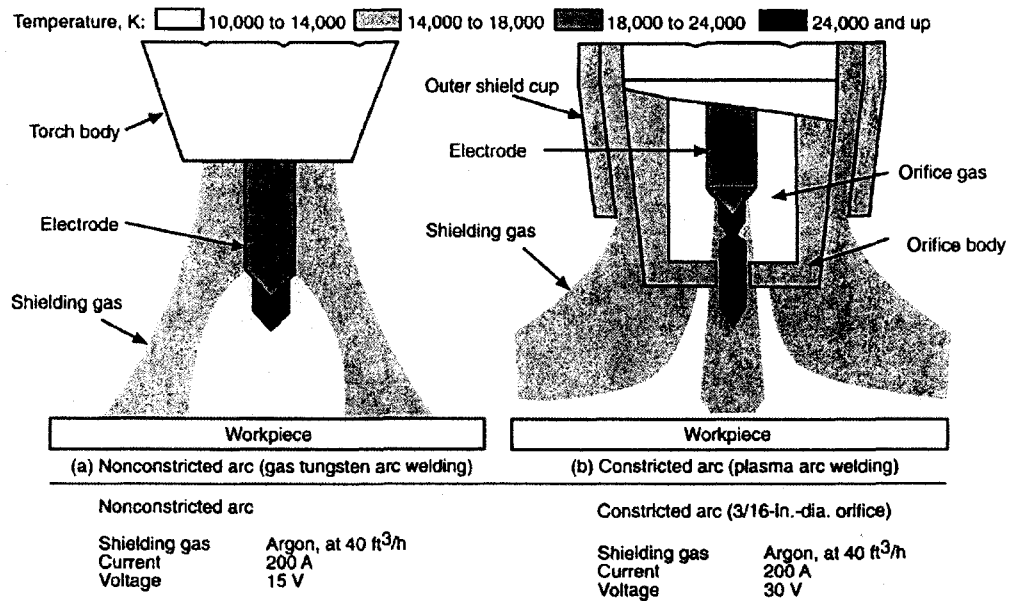


Figure 2-17 - Comparison of PTAW and GTAW Torch Designs [6]

PTAW has several advantages over GTAW. First, the plasma stream is more concentrated, resulting in higher heat transfer to the weld zone and higher arc stability for the same amount of current. Secondly, joints can be formed using less overall heat input because of the highly localized heat input, which results in a smaller heat affected zone, faster cooling and reduced distortion. Also, tungsten contamination of the weld pool is effectively eliminated since the electrode is recessed into the torch. The disadvantages of PTAW compared to GTAW, are that the cost of PTAW equipment is between 2 to 5 times that of GTAW equipment and that PTAW torches are much larger and heavier due to the requirement for water cooling [6].

### 2.4.1.3 Laser Beam Welding (LBW)

Laser beam welding (LBW) was reportedly first used for repair of gas turbine superalloys components about a decade ago. LBW uses a concentrated and columnar beam of light to produce heat in the weld joint. The light beam consists of a stream of photons which are focused by lenses and mirrors to small spot sizes in order to create the high power density required. The condition of the surface of the work piece, especially reflectivity, has a significant effect on the weldability because LBW relies on light beams for heating. A schematic of a typical (Nd:YAG) laser used in laser beam welding is shown in Figure 2-18.

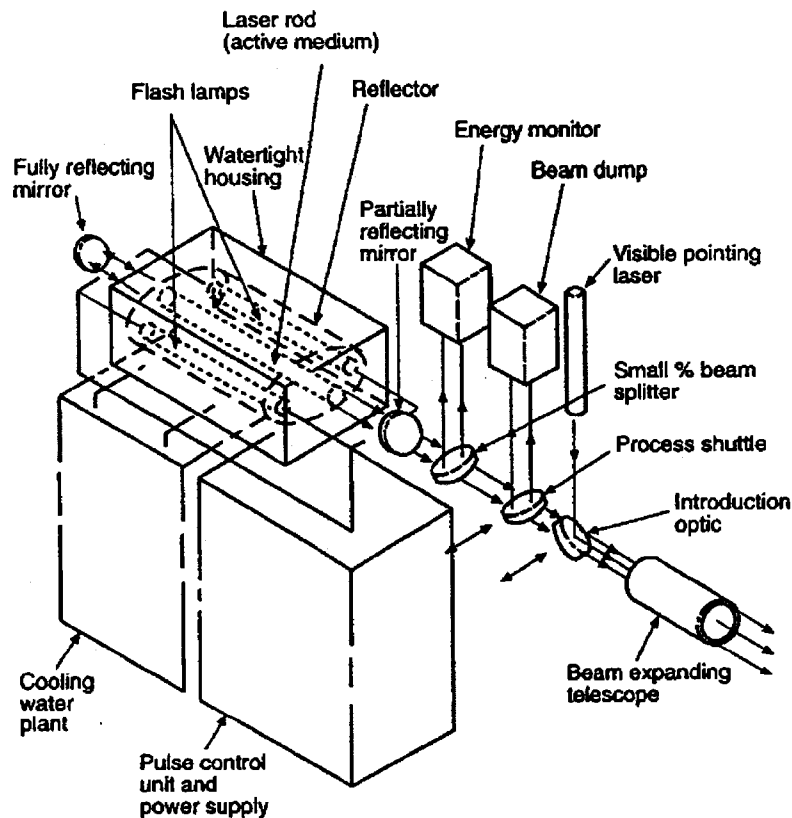


Figure 2-18 - Schematic of Solid State (Nd:YAG) Laser [6]

Heating and melting is highly localized in LBW, as such the specific energy input to the weld joint is low, resulting in a small heat affected zones. LBW is a line of sight process and does not have the contamination issues experienced in GTAW. The initial cost and operator training cost associated with LBW are much higher than GTAW and PTAW and replacement laser lamps are quite expensive [6]. Another disadvantage of LBW is the low overall electrical efficiencies which increase operating costs due to power consumption [6]. Also, the small spot size of LBW makes it generally unsuitable for wide gap repair.

#### **2.4.2 Brazing Processes**

Brazing is a joining method that has been used for over 5000 years [30]. Brazing has become a widely used industrial process for fabricating products to meet a wide range of service demands, from simple domestic utensils to complex structures for aerospace and nuclear industries [31]. Brazing offers an attractive alternative to welding processes due to its batch processing capabilities, being free of the undesirable effects of distortion and having no HAZ [2; 32]. There are two types of brazing process; (i) conventional brazing used for commercial products and (ii) diffusion brazing used for bonding and repair of gas turbine components.

A comparison of weld and vacuum braze repair for superalloy components is shown in Table 2-6. It can be argued that the reduction in cracking, distortion and residual stress combined with the batch processing capability justify the extra initial investment required for vacuum braze repair. Brazing can be used to join ceramics as well as metal components [31]; this is not the case for welding as it relies on melting of the base

material. Welding is a favoured repair method when large areas must be restored due to erosion or cracking. Welding can however have some significant technical and economical limitations due to the large amount of material that must be built up in such repairs. Some repair schemes make use of braze and weld repairs together, while other use a braze-weld-braze sequence to repair cracks [3].

**Table 2-6 - Comparison of Features in Welding and Brazing Repair [5]**

Property	Welding	Vacuum brazing
<b>Heating</b>	High Temperature local heating <ul style="list-style-type: none"> <li>• Distortion</li> <li>• Residual stresses</li> <li>• Cracking in HAZ</li> </ul>	Uniform heating <ul style="list-style-type: none"> <li>• No distortion</li> <li>• No stresses</li> <li>• No cracking</li> </ul>
<b>Filler metal</b>	Commercial fillers	Commercial fillers or self mixed and tailored pastes
<b>Efficiency</b>	One crack at a time / one part at a time	Multiple cracks and multiple samples
<b>Operator Requirements</b>	Skilled specialist	Less skilled operator

#### **2.4.2.1 Methods of Melting Braze Alloy**

The main techniques used to melt braze alloy involve either localized heat application by flame torches, electrical resistance, electrical induction, or the generalized heating of the entire component in either molten salt or metal baths, or in controlled atmosphere furnaces [31; 32; 33; 34]. Capital investments in brazing installations can range greatly, from inexpensive manual gas torches to extremely costly vacuum furnaces. However the added cost of vacuum brazing equipment can often be justified by the increased joint quality that can be obtained [30]. Not all of the techniques listed in the following sections are used for repair brazing of superalloys, they are however listed for completeness.

### **2.4.2.1.1 Flame/Torch Brazing**

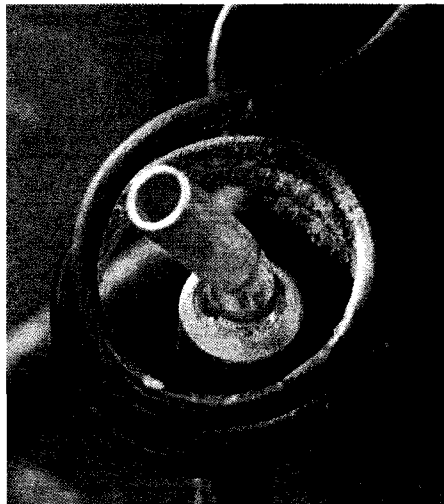
Manually operated flame brazing is arguably the simplest, and possibly the most frequently used brazing technique for joining metal components. This technique is particularly useful for one-off or small production runs and its use can be automated using linear or rotary transfer systems. A variety of gas mixtures are used, which are capable of producing flames with temperatures up to 3500°C [31], sufficient to melt most braze alloys. When performing manual torch brazing, filler metal is supplied by melting the tip of a filler rod and bringing it into contact with the component near the entrance of the joint. In order to produce a quality joint, the component surface must be clean to promote good wetting. Fluxing compounds (a mixture of alkali borates or halides), which are applied to the surface as either a powder or a paste within the filler rod are used to ensure foreign bodies and reactive materials are removed from the braze joint. Flame/torch brazing is restricted on superalloy components as the combustion gases and the use of fluxing agents would lead to contamination. An example of semi-automated torch brazing is shown in Figure 2-19.



Figure 2-19 - Semi-Automated Flame Brazing [32]

#### **2.4.2.1.2 Resistance/Induction Brazing**

Resistance and induction are fast and clean brazing processes. In resistance heating, joints are locally heated by passing an electrical current through the component which is securely clamped by electrodes which allow the current to flow. Induction heating is a non-contact alternative which relies on a high frequency electromagnetic field from water cooled induction coils to heat the braze region. Typically induction heating equipment operates in the range of 1-500 kHz, depending on the type of material being joined [30; 34]. Resistance and induction brazing processes requires substantial skill to avoid overheating the braze alloy and base material [31]. Examples of induction and resistance brazing are shown in Figure 2-20 and Figure 2-21 respectively.



**Figure 2-20 - Induction Brazing Setup [32]**

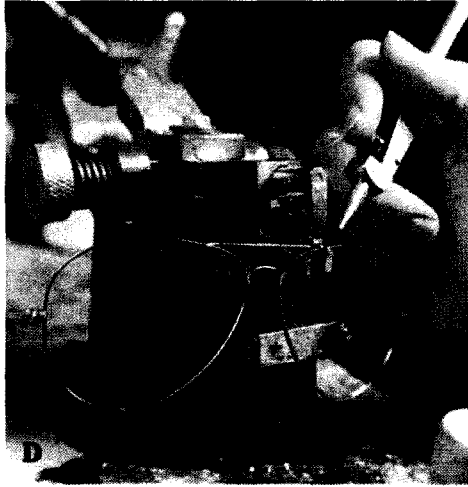


Figure 2-21 - Resistance Brazing Setup [32]

#### **2.4.2.1.3 Immersion Brazing**

Immersion brazing has two main forms, dip brazing and furnace brazing. Both of these processes lend themselves to batch or continuous operations. Unlike flame, induction and resistance brazing methods, the entire component is heated in immersion brazing, avoiding component distortion due to non-uniform heating. Dip brazing is performed by immersing the components in a bath of molten salt, metal or flux. The temperature of the bath is maintained constant by external gas torches or internal electric heating elements. A schematic of a dip brazing setup is shown in Figure 2-22.

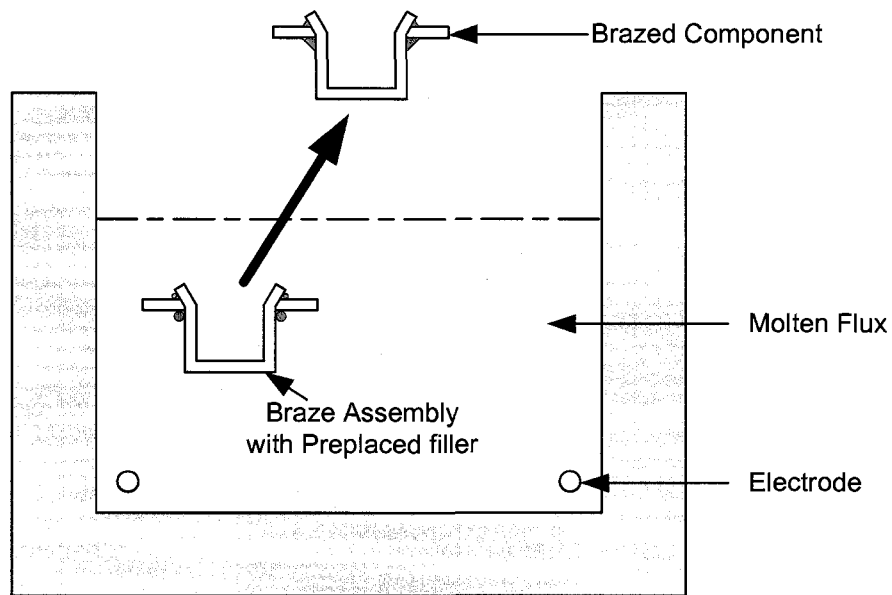


Figure 2-22 - Schematic of a Typical Dip Brazing Setup, Adapted from [34]

#### 2.4.2.1.3.1 Furnace Brazing

Furnace brazing can be performed in either continuous or batch furnace chambers. Continuous furnace chambers are usually filled with a controlled atmosphere such as argon; batch furnaces can also be filled with an inert or reducing gas or be under vacuum. Continuous furnace brazing lends itself towards mass production of small items, particularly for the automotive industry while batch furnaces are mainly used in applications with short production runs for large components or components with high value, such as gas turbine hot section component repair [3; 31]. Most brazing of gas turbine hot section components is carried out using a vacuum furnace with pressure in the order of  $10^{-4}$  mbar [3; 35]. The use of a vacuum chamber eliminates the need to flux for oxide removal [31]. An example of a typical continuous brazing furnace is shown in Figure 2-23 and a typical vacuum furnace in Figure 2-24.

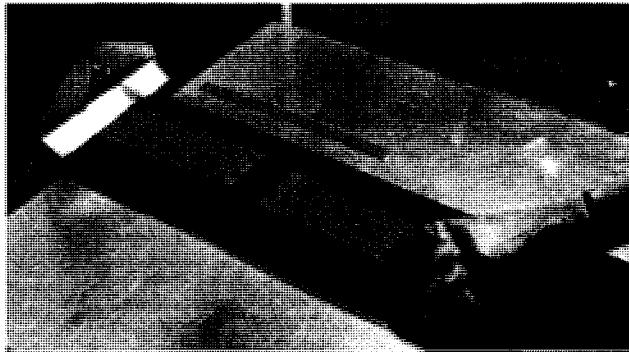


Figure 2-23 - A Typical Continuous Brazing Furnace [32]

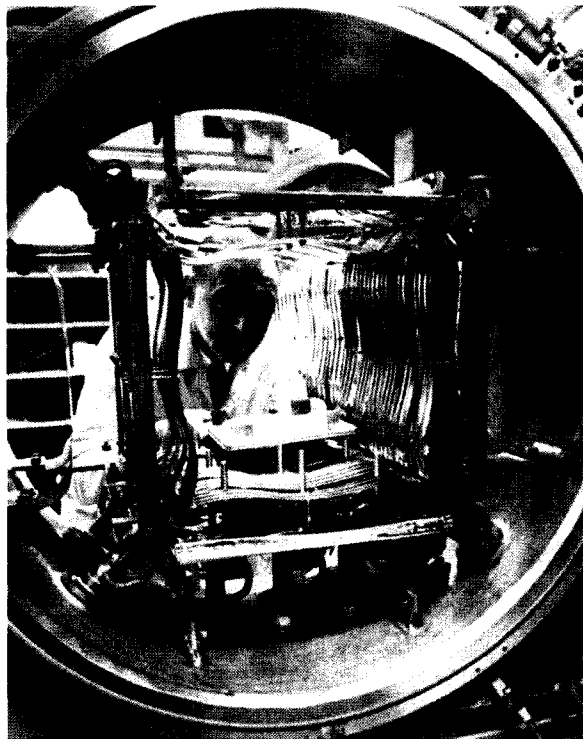


Figure 2-24 - A Typical Vacuum Furnace [34]

#### ***2.4.2.2 Diffusion Braze Repair***

Diffusion brazing is a process used to join superalloy components. Diffusion brazing employs a braze alloy which has composition similar to the base metal but also contains a melting point depressant (such as B, Si, Hf). Repair brazing can be performed to fill cracks or restore dimensions and shapes. Repair of cracks is divided into two categories, narrow gap ( $< 200 \mu\text{m}$ ) and wide gap ( $> 200 \mu\text{m}$ ). The gap size of narrow gap brazing

(NGB) is limited by the capillary forces which draw the liquid braze alloy into the joint and by the formation of brittle centerline phases which form when the gap is excessively large. For the most part, all braze repair techniques follow the same process sequence in order to form a high quality joint. As shown in Figure 2-25, the process begins by removal of the remaining protective coating covering the vane, followed by straightening or retwisting, a surface cleaning process, braze repair and subsequent heat treatments, machining to the specified dimensions, recoating, and inspection.

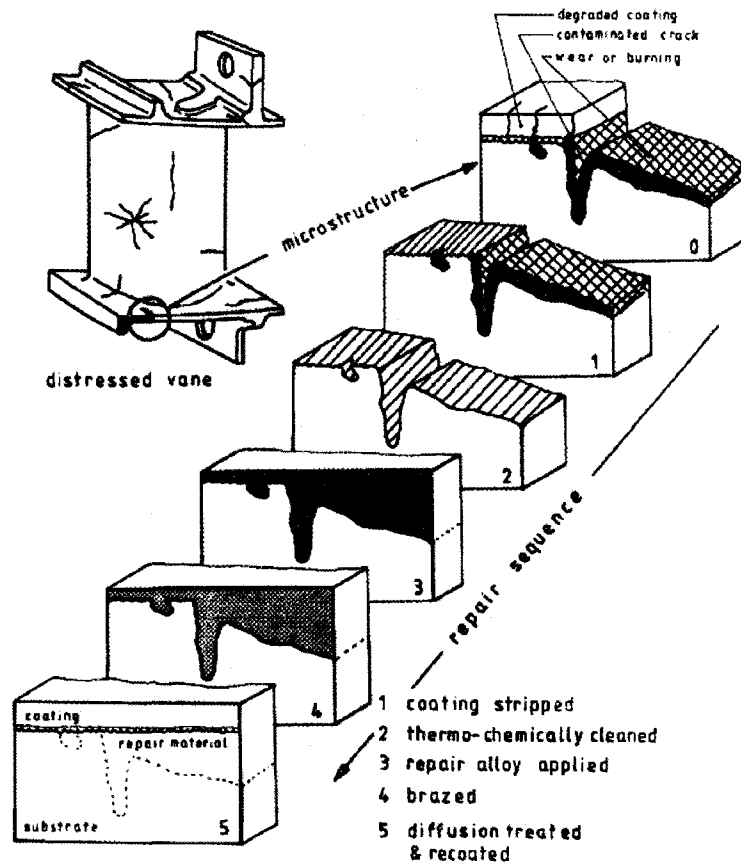


Figure 2-25 - Schematic of Braze Repair Process [2]

Because of the high affinity for oxygen of the alloying additions of superalloys (i.e., Al, Ti, Cr), brazing of gas turbine superalloy components is performed in a vacuum furnace.

This produces a high strength, corrosion resistant joint without cracking the base material [4]. Regardless of the application, the requirements for a successful braze are generally the same, the braze alloy must melt and flow over the substrate surfaces, wetting them completely to form a solid, permanent bond upon solidification [31; 35].

#### **2.4.2.2.1 Narrow Gap Brazing**

In narrow gap brazing (NGB), the joint is formed by introducing a braze alloy that melts below the solidus temperature of the substrate. During brazing the molten braze alloy is drawn into the gap created in the substrate by capillary forces. Good wetting and flowability of the braze alloy are essential to the formation of a high quality joint. The flow of the molten braze alloy into a vertical gap between the substrate, as shown in Figure 2-26 can be derived as:

$$2\gamma_L \cos\theta = h\rho_L gW \quad \text{Eqn. 2-1}$$

where  $g$  is the acceleration due to gravity and  $\rho_L$  is the liquid density and as shown in Figure 2-26,  $\gamma_L$  is the surface tension of the braze alloy,  $W$  and  $h$  are the gap width and the height of the liquid metal being drawn into the gap and  $\theta$  is the contact angle between the liquid and the capillary wall [31]. Ideally, the flow of liquid into the capillary gap of wettable components will be impeded only by viscous and gravitational forces, thus joints can fill in mere seconds, however in practice filling of the capillary gap is impeded by oxide films on the component surface. The joint region must be clean to avoid contamination and oxide formation in the braze, improving braze alloy flow [5; 30; 31].

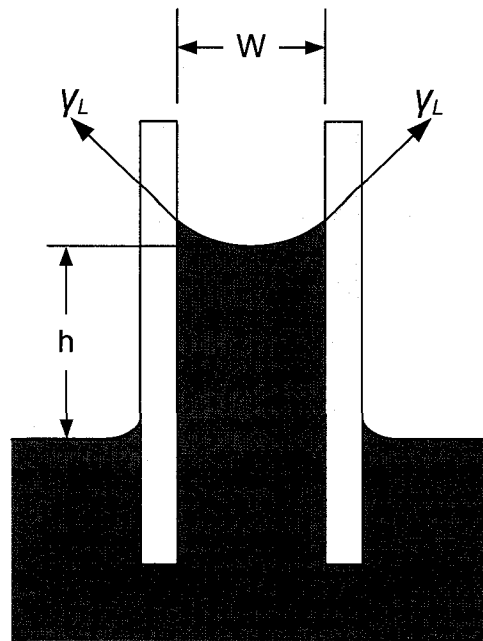


Figure 2-26 - Liquid Rise in a Narrow Capillary Gap, Adapted from [31]

#### 2.4.2.2.2 *Wide Gap Brazing*

Wide gap brazing (WGB) is a process that is often used in the repair of defects too large to be repaired by the standard, NGB process. In WGB, the braze alloy is combined with an additive material having a composition the same or similar to the substrate, as shown in Figure 2-27. This braze alloy/additive alloy configuration provides the opportunity to develop braze joints with enhanced properties by using alternative additive alloys. The use of WGB has increased substantially for the repair of gas turbine components over the last decade because gas turbine components have become increasingly more difficult to weld due to the complex designs and use of less weldable materials. Traditional wide gap joint filler metals consist of up to 60% additive alloy with about 40% braze alloy [36]. Most current braze repair is performed on non-critical stationary parts, though the use of brazing on low stress regions of rotating components is increasing.

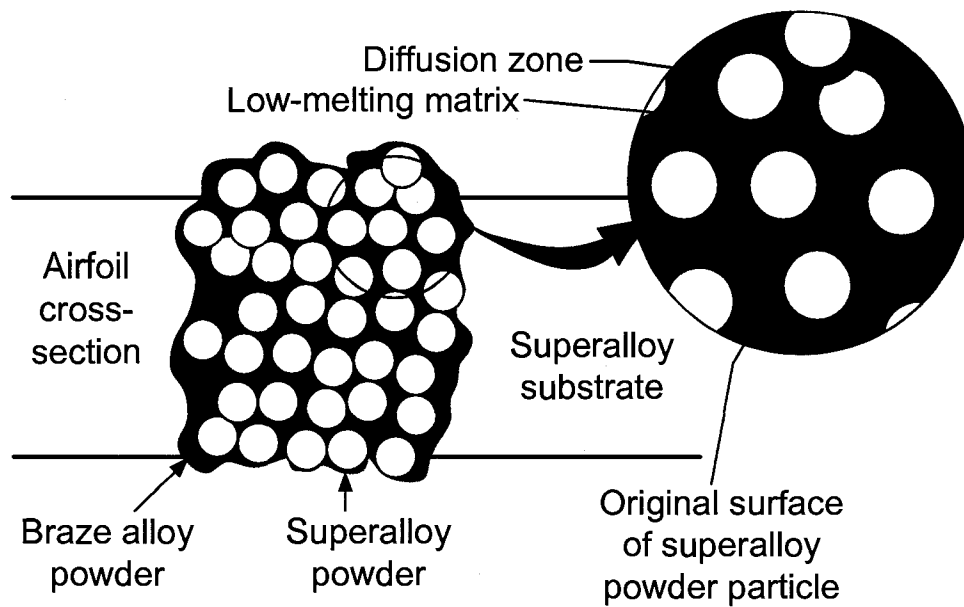


Figure 2-27 – WGB Braze Alloy / Additive Alloy Configuration, Adapted from [9]

#### 2.4.2.2.3 Diffusion Brazing Materials

Brazing materials are widely available throughout the industrialized world as thin rods, sheets, powders or pastes [37; 38; 39]. Diffusion brazing processes are typically performed with gas atomized metal powders.

##### 2.4.2.2.3.1 Methods of Filler Application

The filler metals (braze alloy and additive alloy) used for diffusion brazing of gas turbine components come in the form of powders, extruded pastes, tapes or plates, presintered preforms (PSP) or amorphous foils [5]. Powders are normally produced by inert gas atomization and sieved to a narrow range of particle sizes to ensure consistent melting during the braze cycle [3]. Pastes can be made by adding organic binders and solvents to powder particles and are generally applied by brushing, syringe or made into a putty-like consistency to fill large gaps. Pastes must be dried completely before the brazing cycle begins to avoid disruption of the filler due to gas evolution from the binding agent

[3]. Tapes are manufactured by forming a suspension containing the filler metal powders and an organic binder agent which is then drawn into a thin film using a tape casting machine and allowed to cure. Typical applications for tapes include bonding combustors and honey comb panels. Preforms are produced by sintering a mixture of braze alloy and additive alloy. Braze joints using preforms are capable of producing very high quality joints due to the reduced braze alloy content [5], mitigating the undesirable effects of melting point depressants. Brazing foils are produced by melt spinning or rolling (in the case of more ductile materials). Foils are available in a range of thickness from 0.025 to 0.6 mm with widths up to 50 mm [3]. Foils are typically used for joints with large surface areas that do not require extensive gap filling and for manufacturing. A summary of the various braze application systems can be seen in Table 2-7.

**Table 2-7 - Comparison of Different Braze Application Systems, Adapted from [5]**

<b>Property</b>	<b>Paste</b>	<b>Tape</b>	<b>PSP</b>	<b>Foil</b>
<b>Form of the FM</b>	Powder + organic binder	Powder + organic binder drawn into tape and dried	Homogeneous Sintered composite of brazing alloy and additive alloy	Amorphous foil with homogeneous composition
<b>Typical flaws</b>	Shrinkage, voids, surface cracks	Shrinkage, voids, surface cracks	Porosity < 2%	High quality possible
<b>Application characteristics</b>	Operator skills required, timely, best for crack filling	Cut to shape, good for customized shapes, adding material	Sheets of 0.010" to 0.1" thick. Tack welding or cement in place. Adding material or wide gap brazing	Lap joints, increase of material thickness or filling cracks, limited thickness
<b>Health Concerns</b>	Toxic binders	Toxic binders/tape	None	None
<b>Costs</b>	Low	Mid	High	Low/mid

As mentioned previously, presintered preforms (PSPs) are a homogeneous mixture of braze and additive alloys, typically with a minimum 1:1 ratio of additive alloy to braze alloy for wide gap brazing operations. PSPs can have a density of up to 98%, thus little or no shrinkage of the braze region, limiting the quantity of and size of voids, greatly increasing the physical soundness of the joint [40]. Preforms are also easily handled and environmentally safe, as no organic binder is needed in their manufacture. Preforms of various shapes and sizes can be easily obtained by preparing plates of sintered material followed by machining practices such as punching, laser cutting, water jet cutting or electrical discharge machining. After cutting the preforms to the required shape, they can be tack welded onto the repair region and undergo brazing [41]. Though the cost of producing PSPs is comparatively high (as they require sintering), it can be argued that the benefits from low porosity attained by using PSPs outweigh these cost in aeroengine repair applications [5]. Examples of such preforms are shown in Figure 2-28.

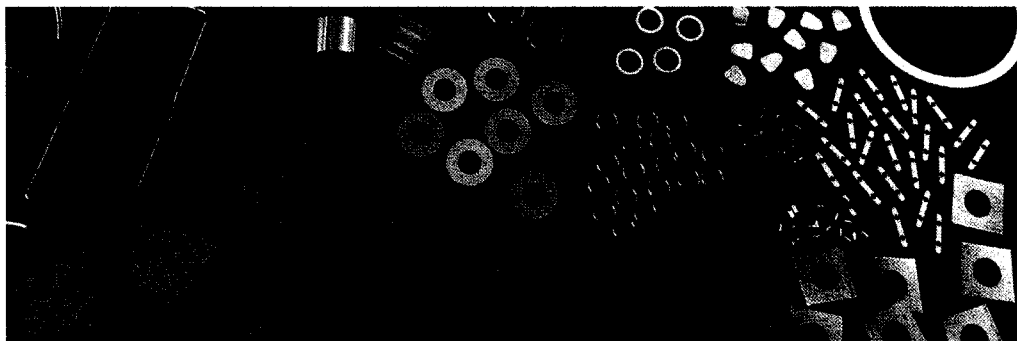


Figure 2-28 - Examples of Presintered Preforms [32]

#### **2.4.2.2.3.2 Nickel and Cobalt Fillers**

Braze material selection must take into consideration factors such as the melting temperature of the substrate and braze alloy, the mechanical properties at the service

temperature as well as the chemical, physical and mechanical compatibility between the substrate, additive and braze alloys [31; 33; 34].

Nickel-base braze alloys were originally developed from nickel hard-facing alloys which contained carbon, silicon and boron in order to produce hard nickel and chromium compounds on surface layers for high wear and corrosion resistance [30]. The particle sizes and suggested brazing temperatures for some commercial nickel and cobalt-base braze alloys can be seen in Table 2-8.

**Table 2-8 - Brazing Temperature and Particle Size of Selected Commercial Braze Alloys**

Nominal Composition	Product Name	Brazing Temp. (°C)	Particle Size (µm)
<b>Sulzer Metco [39]</b>			
Co-0.4C-19Cr-8Si-4W-17Ni	AMDRY 400	1150 – 1230	-140 /+ 45
Co-22Cr-21Ni-14W-2B-2Si-0.03La	AMDRY 788	1220-1260	-106 /+ 45
Ni-18.5Cr-18Fe-5(Cb+Ta)-3Mo-2.5B-1Ti	AMDRY 718B	1230 - 1275	-125 /+ 45
Ni-19Cr-10Si	AMDRY 100	1150 - 1205	-106 /+ 45
<b>Wall Colmonoy [37]</b>			
Co-8Si-19Cr-17Ni-4W-0.8B	Nicrobraz 210	1205	104
Ni-14Cr-3B-4.5Si-4.5Fe-0.7C	Nicrobraz 125	1175	104
Ni-6W-4.5Si-0.06C-3.2B-3Fe-7Cr	Nicrobraz 200	1120	104
<b>Praxair [38]</b>			
Co-8Si-19Cr-17Ni-4W-0.8B	Co-216	1149-1232	-106 /+ 45
Ni-0.8C-4.5Si-14.5Cr-3.3B-4.5Fe	Ni-167	1066-1204	-106 /+ 45
Ni-4.5Si-14Cr-3B-4.5Fe	Ni-510	1077-1204	unavailable

Additional modifications can be made to braze alloy compositions to enhance wetting behaviour, mechanical properties and corrosion resistance by employing multiple alloying elements in the alloy. However most braze alloys are designed to have a narrow two phase solid-liquid temperature range, or mushy zone. Eutectic alloys undergo a direct phase change from solid to liquid at a specific temperature. Examples of eutectic reactions for the B-Ni and B-Co binary phase diagrams are shown in Figure

2-29 and Figure 2-30. Eutectic braze alloys are used in the majority of commercial brazing operations because their lower melting temperatures reduce the possibility of macroscopic distortion and microstructural degradation of components while being heated to the brazing temperature. Another important benefit to eutectic alloys in brazing is that their direct transition from solid to liquid states, eliminating premature flow of liquid during heating [31].

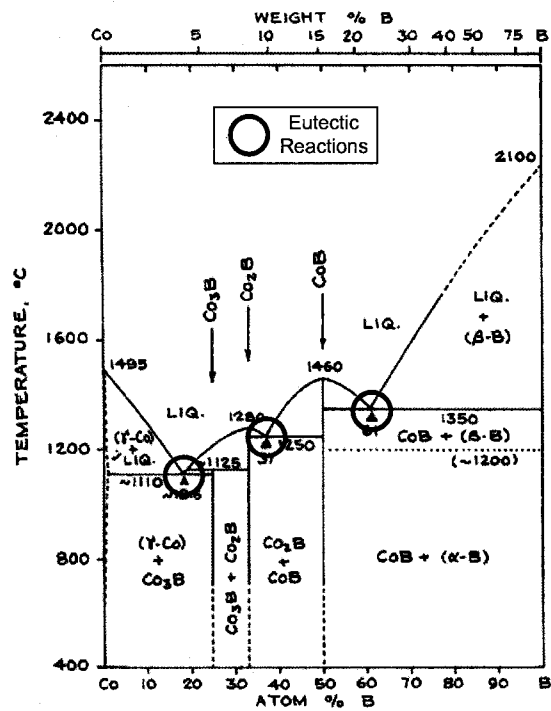


Figure 2-29 - The B-Co Phase Diagram [42]

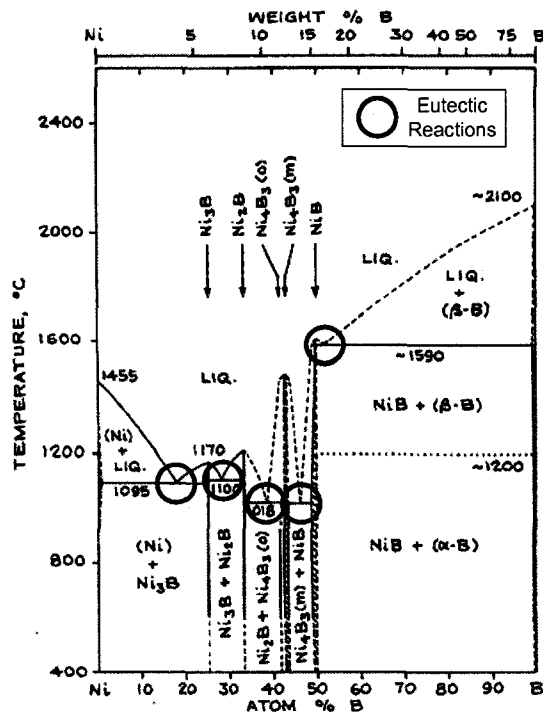


Figure 2-30 - The B-Ni Phase Diagram [42]

### 2.4.2.2.3.3 Melting Point Depressants

The liquidus temperature of nickel-base braze alloys is reduced by the use of melting point depressants. After solidification, the melting point depressant can diffuse away from the braze region, eliminating the possibility of re-melt upon reheating [7; 3; 43]. Early nickel-base braze alloys used silicon as a melting point depressant. Phosphorus and boron were introduced in braze alloys later [44]. Boron is generally preferable to silicon as a melting point depressant because it diffuses more readily and thus has a reduced tendency of forming long brittle eutectic chains [3]. Recent research has examined the possibility of using hafnium as a melting point depressant [45]. Hafnium is attractive as a melting point depressant because it produces a more ductile joint than the traditional boron or silicon alloys and it also provides some resistance to high temperature corrosion [45]. The use of traditional melting point depressants typically

presents problems such as the formation of eutectic chains [7; 3; 31; 30]. These brittle eutectic chains may act as easy crack propagation paths [46] and as such post braze heat treatments must be applied to sufficiently diffuse the melting point depressants away from the joint.

#### **2.4.2.2.4 Braze Cycles and Heat Treatment**

The flowability of the braze alloy is what determines the distance it will penetrate into a capillary gap, this property is dependent on the action of capillary forces, viscosity and density of the liquid metal, as well as the geometry of the joint to be filled [5]. While it is important to have sufficient flowability in NGB joints, it is also essential in WGB joints to an even distribution of the braze alloy and additive alloy components and to promote wetting of the additive alloy particles. One means of increasing the flowability of the braze alloy is to increase the brazing temperature. Increasing the brazing temperature will also increase the diffusion rate of alloying elements in the braze joint, resulting in a more homogeneous braze joint with improved mechanical properties [5].

Brazing temperature and time have a direct effect on the extent of interdiffusion that occurs during brazing. Temperature is by far the most important process parameter during brazing, it is essential that the braze alloy be fluid enough to have sufficient flowability [31]. The minimum brazing temperature is generally only 6°C above the liquidus temperature of the braze alloy while the maximum overheat is generally 95°C [31; 34]. Theoretically, only a few seconds are required for the molten braze alloy to flow into capillary gaps, experimental observations however suggest that short dwell times of several minutes at the brazing temperature are needed to disrupt surface oxide

films [31]. In NGB contact between the faying surfaces during the brazing process is necessary to ensure a capillary gap is formed. Jigs and deadweights may be used to ensure contact and part alignment is maintained during brazing [31].

#### ***2.4.2.2.4.1 Braze Cycle***

Although only a short dwell period at the brazing temperature is required to melt and allow for adequate flow of braze alloy, additional dwell periods at intermediate temperatures are often introduced to the brazing cycle. These dwell times often make up the majority of the braze cycle and are imperative when brazing superalloys to achieve a homogeneous joint microstructure free of embrittling phases which form in the presence of binder [31]. A typical brazing cycle begins with a brief hold at an intermediate temperature for degassing followed by heating to the braze temperature. Evaporation of the organic binder typically takes place between 400 and 600°C [4; 5]. A dwell period of 10 to 20 minutes at the brazing temperature is usually employed to ensure full melting and flow of the braze alloy and promote interdiffusion. Upon completion of brazing, the joint can be brought to a lower temperature for further diffusion heat treatment, as shown in Figure 2-31a or be cooled and be brought back up to brazing temperature again as shown in Figure 2-31b. During this subsequent heating, no re-melting should occur, as sufficient melting point depressant will have diffused into the base material. This additional heating serves to further diffuse the melting point depressants into the substrate and additive alloy. Diffusion within a liquid metal is quite fast, and as the melting point depressant diffuses away, the melting temperature of the braze alloy is increased, causing the formation of the  $\gamma$  matrix and the

precipitation of carbides and borides as well as the centerline segregation of alloying elements in NGB joints of excessive gap size [5].

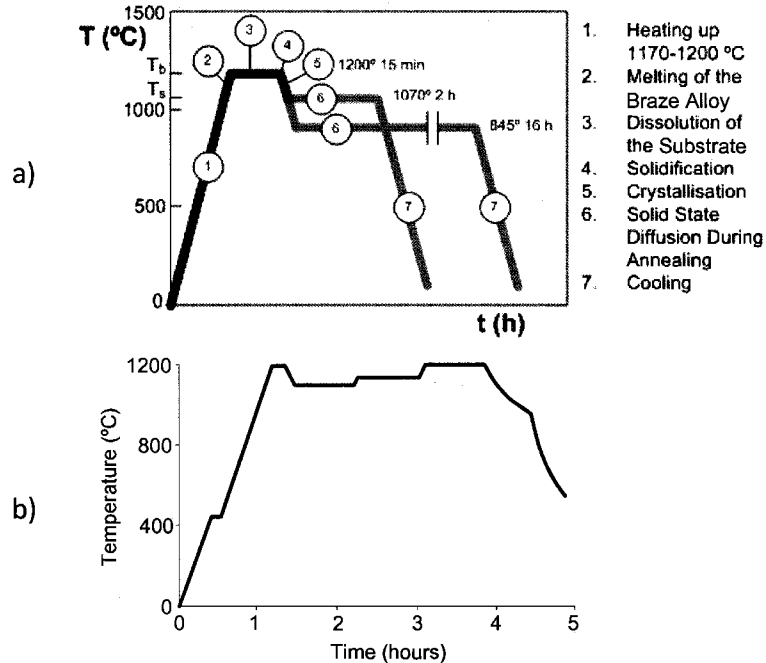


Figure 2-31 - Brazing Thermal Cycle (Time-Temperature), Adapted from [3; 5]

#### 2.4.2.2.4.2 Post Braze Heat Treatment

Following brazing it is general practice to perform a post-brazing heat treatment, especially in the case of superalloy brazing. This heat treatment is performed to ensure the substrate is restored to its fully heat treated condition before returning the part to service. Hot isostatic pressure (HIP) in some cases can be used to close voids in the substrate and braze joint [5].

#### 2.4.2.2.5 Examples of Braze Repair for Gas Turbine Components

There are many repair shops that offer overhaul services for gas turbine hot components. Repair processes such as those employed by Liburdi Turbine Services [47] and Standard Aero Engine Services [48] are quite promising, they are however, for the

most part proprietary. Regardless of the company performing the WGB repair, the filler consists of a mixture of powdered superalloy (additive alloy) and braze alloy. The importance of WGB as a repair process can be readily seen by the increasingly diverse selection of available materials developed specifically for braze repair.

As shown in Table 2-9, the strength of a brazed joint is generally lower than the strength of the base material, however these reductions are largely based on the joints quality and the materials selected for the repair, and thus can be adjusted by using different alloys and process parameters.

**Table 2-9 - Tensile Test Results of WGB of X-40 Superalloy [36]**

Temperature (°C)	Yield Strength (MPa)		
	X40	Braze A	Braze B
21	525	449.5*	499.7*
540	275	273.5*	319.5*
650	260	222.4*	260.1*

\*average of source data points  
 Braze A: 60/40 ratio of X-40/braze alloy (Co-40Ni-24.5Cr-3B)  
 Braze B: Proprietary – not reported

Liburdi Turbine Services [47] has implemented several processes for the repair of gas turbine components. Table 2-10 summarizes the base, additive and braze alloys used in a patented process which employs a nickel-base additive and braze alloy for the repair of a cobalt-base vane.

**Table 2-10 - Composition of a Specific Braze Alloy System Used by Liburdi Turbine Services [49; 50; 51]**

Element	Cobalt-base Vane Alloy	Filler Alloy (~325 mesh)	Braze Alloy (~325 mesh)
Ni	10.5	Balance	Balance
Cr	25.5	16.0	14.0
Co	Balance	8.5	10.0
Al		3.5	3.5
Ti		3.5	
W	7.5	2.6	
Mo		1.75	
Ta		1.75	2.5
Nb		0.85	
C	0.25	0.10	
B	0.01	0.01	2.7
Zr		0.06	
Y			0.06

General Electric Company (GE) has a number of repair processes which are described in US Patents. In addition to having processes for repair of polycrystalline components, GE has developed repair processes for directionally solidified and single crystal alloys [52]. Some of the braze alloys used by GE for the repair of cobalt-base superalloys X-40 and FSX-414 are listed in Table 2-11. GE has also patented the various processes which they follow for the repair of gas turbine hot section components.

**Table 2-11 - Selected Braze Alloys Used by GE for Repair of X-40 and FSX-414 [53; 54]**

Element	Braze Alloy		
	A	B	C
Ni	10	10	10
Cr	29	29	29
W	7	3.5	7.5
C	0.1	0.1	0.25
B	2.5	1	0.015
Si	2.5	7	0.9
Mn	0.6	0.6	0.6
Co	Bal.	Bal.	Bal.

#### 2.4.2.2.5.1 Examples of Narrow Gap Braze Repair Microstructures

Tung, et al.[44] performed a NGB study, using BNI-4 (Ni-3.5Si-1.9B) braze alloy pure nickel additive. The braze microstructure consisted of a  $\gamma$ -nickel solid solution near the joint substrates with  $\gamma$ -nickel nodules, bulky nickel borides, a binary eutectic of  $\gamma$ -nickel and nickel boride and a fine ternary eutectic of  $\gamma$ -nickel, nickel boride and nickel silicide as well as a nickel silicide within  $\gamma$ -nickel nodules. The constituents found in this study are listed in Table 2-12 along with the relative composition of nickel and silicon in the phases. The energy dispersive spectroscopy (EDS) equipment used in this study was unable to measure boron.

Table 2-12 - EDS Results of Commercial Pure Nickel Brazed With BNI-4 Braze Alloy [44]

Phase	Relative Weight (%)	
	Ni	Si
$\gamma$ -nickel	96.0	4.0
Nickel boride	99.7	0.3
Nickel silicide	89.5	10.5

Miglietti [55] performed a study on the process parameters for NGB of nickel-base superalloy MAR-M247 (Ni-10Co-10W-8.25Cr-5.5Al-1Ti-3Ta-0.7Mo-0.2Si-0.5Fe-1.5Hf-0.05Zr-0.015B-0.15C), using the nickel-base braze alloy Microbraz 150 (Ni-15Cr-3.5B) with a 100  $\mu$ m braze gap. The purpose of the study was to evaluate the influences of braze time and temperature on the resulting braze microstructure. The brazing temperature was varied between 1125° (specified by the braze alloy manufacturer) and 1200°C and brazing time was varied between 20 and 14,400 minutes, as listed in Table 2-13. Miglietti found that at 1125°C and 1150°C, regardless of the brazing time, the joint microstructure was undesirable due to the presence of hard, brittle boride phases,

an example of this is shown in Figure 2-32a. This hard brittle boride phase appeared at the centerline of the braze, regardless of brazing time. For the specimens brazed at 1200°C, with braze time increasing from 3540 (Figure 2-32b) to 14,400 (Figure 2-32c) minutes, it was observed that no centerline or brittle hard boride phases were present in the joint, equiaxed grains formed in the joint area, the volume fraction of the  $\gamma'$  precipitates in the joint increased and excessive coarsening of the  $\gamma'$  precipitates in the parent metal occurred. It was shown that increasing the time at temperature played a beneficial role in improving the joint microstructure, as it reduced the size of the brittle centerline boride.

**Table 2-13 - Temperatures and Times of Brazing Experiments [55]**

Temp (°C)	Time (min)								
	20	60	120	X	240	X	X	X	X
1125	20	60	120	X	240	X	X	X	X
1150	20	60	120	X	X	360	X	X	X
1200	20	60	120	180	X	360	3540	10080	14400

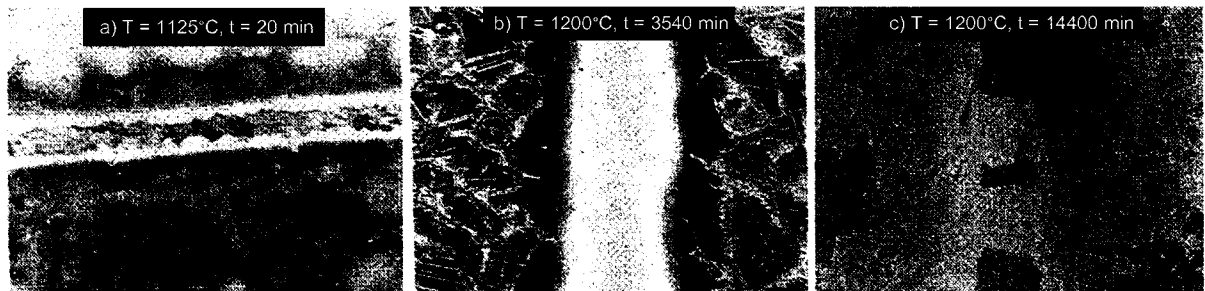


**Figure 2-32 - Selected Braze Micrographs, Adapted from [55]**

Chaturvedi et al. [56] performed a NGB study on cast IN-738 (Ni-16Cr-8.5Co-3.4Al-3.4Ti-2.6W-1.75Mo-1.75Ta-0.9Nb-0.17C-0.1Zr-0.01Mn-0.01B-0.01Si) superalloy using Microbraz 150 (Ni-15Cr-3.5B) braze alloy. Fixed gap widths of 30, 60 and 75  $\mu\text{m}$  were examined and brazing was performed at 1070, 1100 and 1130°C for 10, 20, 40 and 60 minute durations. It was found that regardless of the brazing temperature or holding

time, a continuously distributed centerline solidification band formed which was bordered on both sides by a nickel solid solution phase, as shown in Figure 2-33. Three distinct phases were observed, a nickel-base solid solution, nickel rich boride/carbon-boride and a chromium rich boride/carbon-boride, shown in Figure 2-34, with compositions shown in Table 2-14. A uniform distribution of fine globular precipitates was observed in the base metal, an example of this is shown in Figure 2-35.

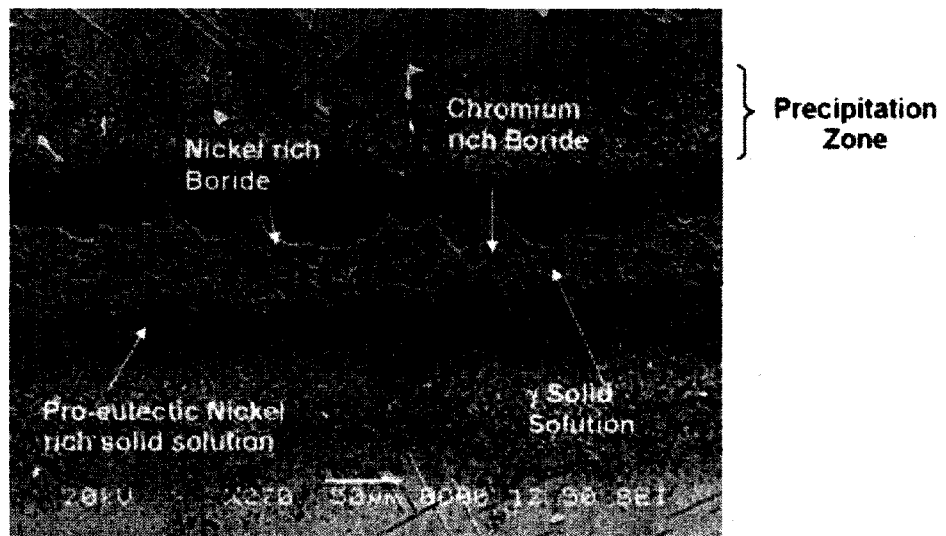


Figure 2-33 - Secondary Electron Micrograph of Centerline Eutectic Constituent in IN-738 Braze with Microbraz 150 [56]

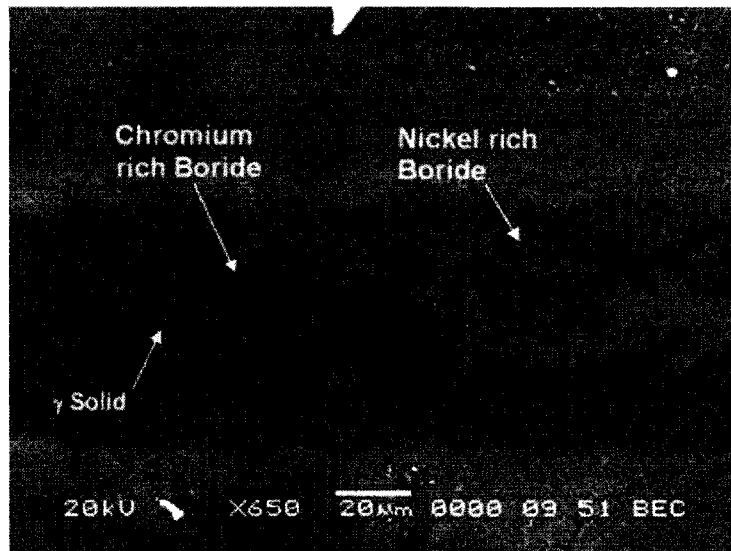


Figure 2-34 - Backscatter Electron Micrograph of Centerline Eutectic Constituent in IN-738 Brazed With Microbraz 150 [56]

Table 2-14 - EDS Results of Centerline Eutectic Constituents in IN-738 Brazed With Microbraz 150 Presented By Chaturvedi et al. [56]

Element	Al	Ti	Cr	Co	Ni	Mo	W
Solid Solution Phase	1.34	0.38	18.54	2.39	76.50	0.30	0.54
Chromium Rich Boride/ Carbon-Boride Phase	0.04	0.08	93.98	0.41	1.88	2.32	1.29
Nickel Rich Boride/ Carbon-Boride Phase	0.81	1.63	11.40	2.68	82.90	0.27	0.29

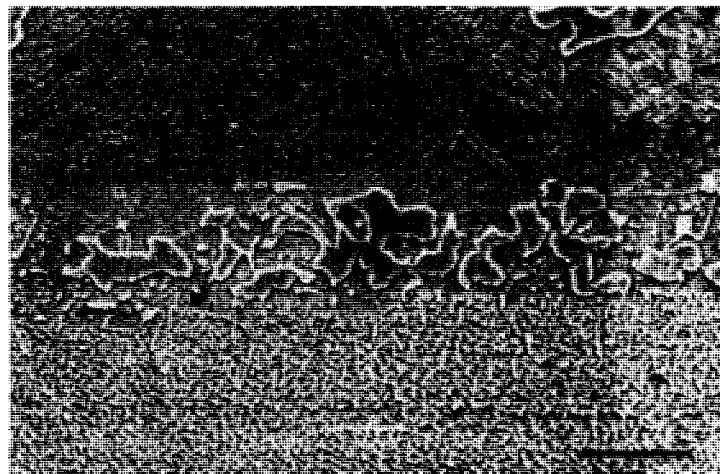
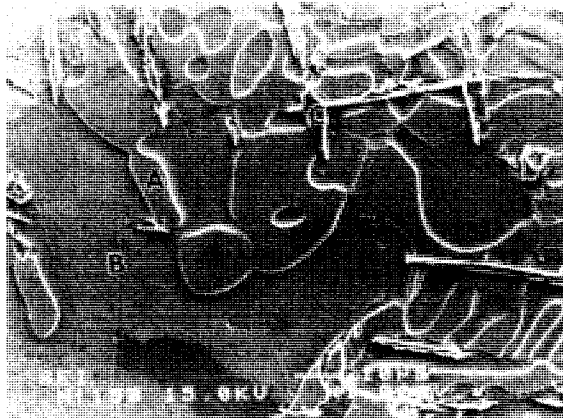


Figure 2-35 - Secondary Electron image of IN-738 Brazed with Microbraz 150 Showing Ni Rich Interface Boride Phase [56]

#### **2.4.2.2.5.2 Examples of Wide Gap Braze Repair Microstructures**

Su et al. [57] studied WGB repair of IN-738 using Nicrobraz 150 braze alloy and IN-738 additive alloy. A braze joint containing only Nicrobraz 150 was also prepared for comparison purposes. It was noted that there were 3 phases present; a nickel boride phase, marked A in Figure 2-36, a  $\gamma$ -phase, marked B in Figure 2-36 and a cerose chromium boride which precipitated on the eutectic formation of the other two phases, marked C in Figure 2-36. When brazed in the wide gap configuration, shown in Figure 2-37. It was noted that the same phases exist but with slightly different composition due to the diffusion of the alloying elements in IN-738, as shown in Table 2-15 and Table 2-16.



**Figure 2-36 - Microstructure of a Brazed Joint Produced by Pure Nicrobraz 150 [57]**

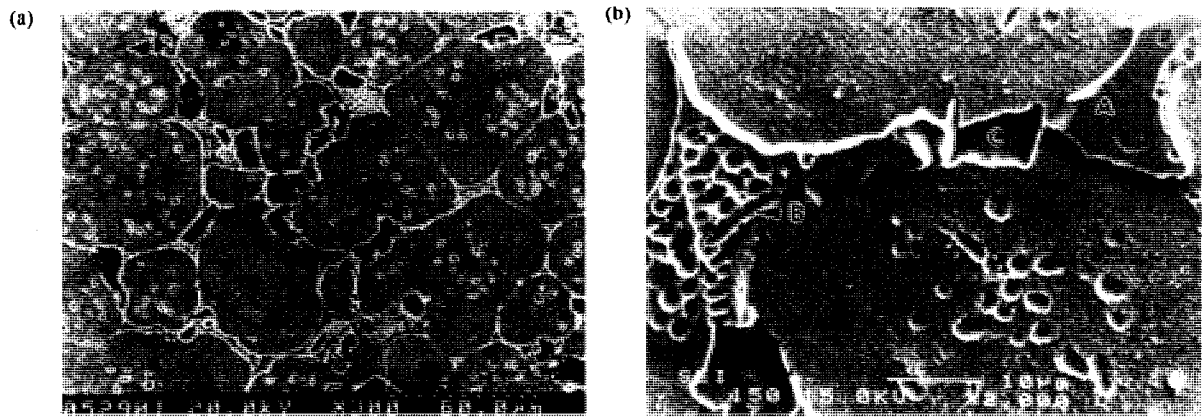


Figure 2-37 - Microstructure of a Brazed Joint Consisting of 40/60 Ratio of Nicrobraz 150 / IN-738 Powder [57]

Table 2-15 - Compositional Analysis of the Phases Found in Braze of Pure Nicrobraz 150, shown in Figure 2-36 [57]

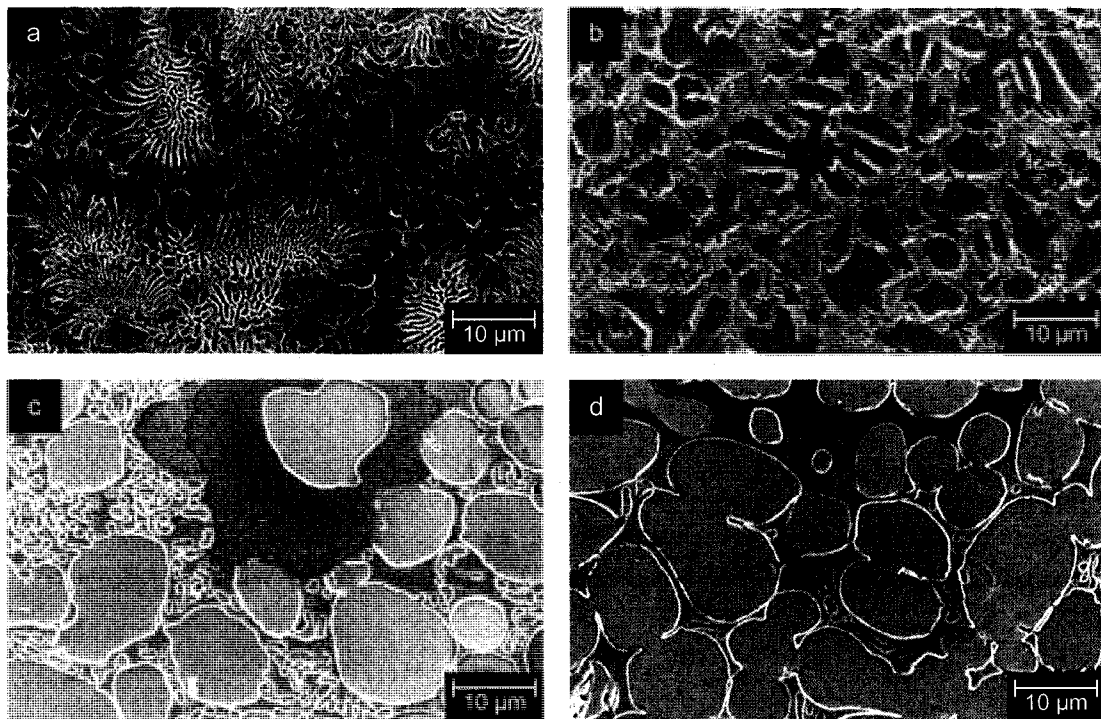
Element	A		B		C	
	wt. %	at. %	wt. %	at. %	wt. %	at. %
Ni	79.94	72.33	87.05	70.42	2.75	1.52
Cr	18.01	18.38	7.44	6.79	80.55	50.16
B	0.51	2.50	2.42	10.59	11.15	33.36
C	1.53	6.80	3.09	12.20	5.54	14.96

Table 2-16 - Compositional Analysis of Phases Found in Braze of 40/60 Ratio of Nicrobraz 150 / IN-738 Powder [57]

Element	B		C	
	wt. %	at. %	wt. %	at. %
Ni	76.248	67.473	4.753	2.957
Cr	4.789	4.783	68.858	48.349
Co	5.833	5.140	1.917	1.188
Al	0.594	1.144	0.006	0.008
Ti	5.117	5.548	0.257	0.196
Ta	2.276	0.654	0	0
Mo	0.248	0.134	5.978	2.275
Nb	1.394	0.779	0.038	0.015
W	0.366	0.103	4.467	0.887
B	1.447	6.946	7.135	24.083
C	1.687	7.295	6.591	20.041

Wu et al. [58] performed a WGB study, joining 304 Stainless steel (Fe-19Cr-10.5Ni-2.0Mn-0.50Cu-1.0Si-0.08C) to Inconel X-750 (Ni-19.0Cr-18.5Fe-3.0Mo-0.2Mn-0.30Cu-

0.20Si-0.04C-5.1Nb-0.5Al-0.9Ti) using AMS 4777 (Ni-6-8Cr-2.5-3.5Fe-4.5-5.0Si-2.75-3.5B) braze alloy and pure nickel powder as an additive alloy. Microstructural analysis and tensile tests were performed on a WGB joint consisting of only the AMS 4777 braze alloy and a WGB joint consisting of the AMS 4777 braze alloy with 30% additive alloy which were brazed at various temperatures. It was shown that the braze joints consisting of only AMS 4777 braze alloy with no additive showed an almost complete eutectic structure which was continuous across the entire braze gap, as shown in Figure 2-38 a and b. The WGB joints consisting of braze alloy and additive alloy formed a eutectic structure with a discrete solid solution phase, shown in Figure 2-38c. The volume fraction of solid solution was found to increase with additive content and brazing temperature, as shown in Figure 2-38d.



**Figure 2-38 - Microstructures of Braze Joints With Different Gap Filler Contents (a) AMS 4777 Only, Brazing Temperature 1423 K, (b) AMS 4777 Only, Brazing Temperature 1523 K, (c) AMS 4777 +30% Additive, Brazing Temperature 1423 K, (d) AMS 4777 + 30% Additive, Brazing Temperature 1523 K [58]**

It was shown that the strength and ductility of the wide gap braze joints increased with increasing brazing temperature and with the amount of additive in the joint, as shown in Figure 2-39. The tensile fracture mode was found to be quasi-cleavage, as shown in Figure 2-40, with some ductile tear occurring in the braze joints containing additive alloy. Crack propagation was found to proceed through the eutectic, and in the case of the braze joints containing additive alloy, these cracks were found to terminate at the surface of the additive powder particles.

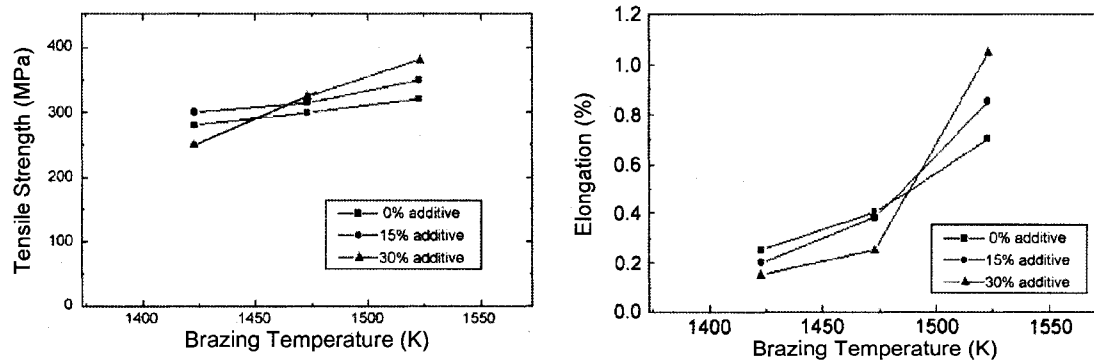


Figure 2-39 - Effect of Additive Alloy and Brazing Temperature on Strength and Ductility of Braze Joint [58]

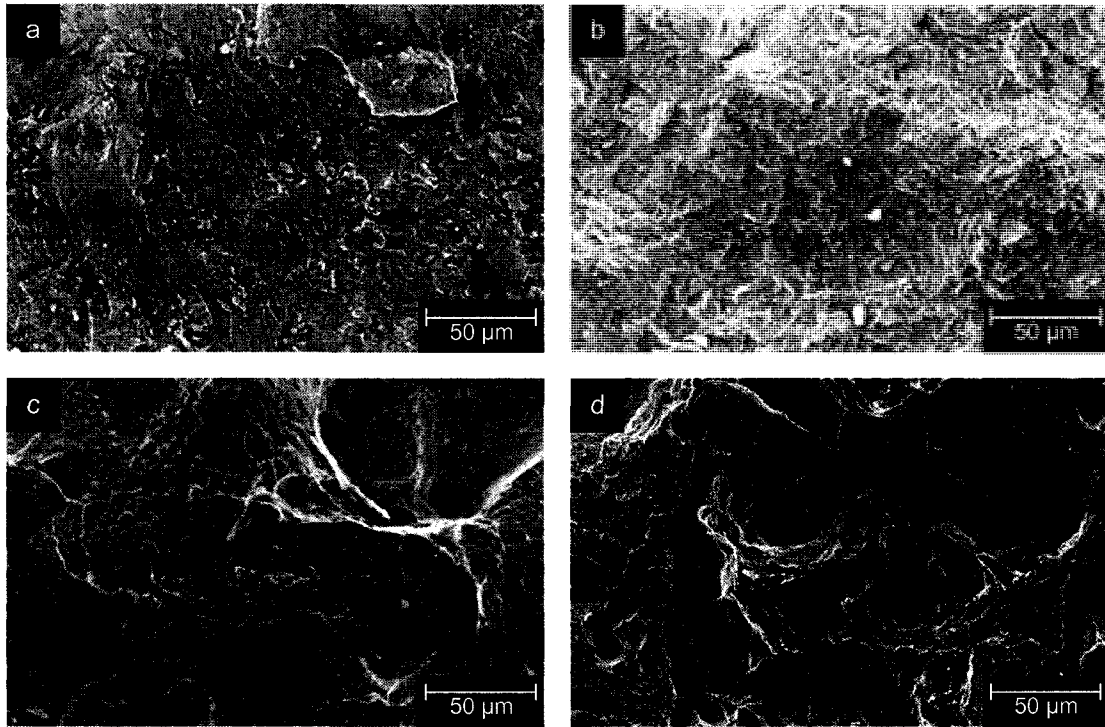


Figure 2-40 – Fracture Surfaces of Braze Joints With Different Gap Filler Contents (a) AMS 4777 Only, Brazing Temperature 1423 K, (b) AMS 4777 Only, Brazing Temperature 1523 K, (c) AMS 4777 +30% Additive, Brazing Temperature 1423 K, (d) AMS 4777 + 30% Additive, Brazing Temperature 1523 K [58]

### 2.4.3 Other Repair Processes

#### 2.4.3.1 Transient Liquid Phase Bonding (TLP)

Transient liquid phase bonding is used by many repair shops and engine manufacturers for a variety of nickel and cobalt-base superalloy applications [6]. Transient liquid phase bonding is a repair process that relies on the use of highly diffusing melting point depressants such as boron in a bonding material which usually has a composition very similar to the base metal. The process uses a thin interlayer, on the order of 0.025 to 0.100 mm (0.001 to 0.004”), placed between the components being bonded under a slight compressive stress at high temperature, 0-10 psi and 1100-1275°C respectively. The interlayer initially melts, filling the gap between components with a thin liquid layer. The alloying elements rapidly diffuse between the interlayer and the base material

causing a sound joint to be formed [59]. The joint then isothermally solidifies yielding a microstructure that generally resembles the base material. It is imperative that the composition and amount of interlayer alloy used in the joint solidify isothermally at the bonding temperature. The joint must be chemically and microstructurally homogeneous with the base metal after application of an annealing heat treatment [60]. Figure 2-41 shows an isothermally solidified TLP joint of Inconel 738LC base alloy and Microbraz 150 filler which was bonded at 1160°C for 2 hours.

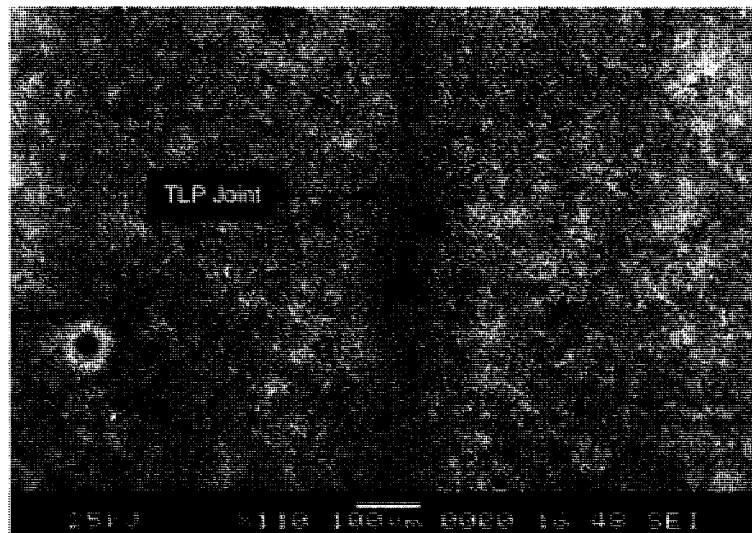


Figure 2-41 - SEM Microstructure of a TLP Joint [61]

#### ***2.4.3.2 Diffusion Bonding***

Diffusion bonding is a solid state diffusion joining process commonly used for crack repair and buildup of wall thickness [6]. No melting of the substrate occurs in this process as it relies on the diffusion of a powder mixture of substrate with a small amount of melting point depressants [6; 31]. The powder is usually applied in the form of cast tapes of various thicknesses for buildup of the wall thickness and in paste form for crack repair. Once the filler metal has been applied, low pressure and high

temperature, usually 75% of the melting point of the substrate (K), are used to achieve a smooth well matched joint with good mechanical integrity [6; 31].

## **2.5 Joint Preparation and Formation**

### **2.5.1 Joint Preparation**

The cleanliness of the component surfaces is absolutely imperative to achieve effective joint formation in all repair processes. In order for the braze alloy to flow and bond with the substrate (and additive alloy in WGB), all constituents must be free of surface oxides [2; 3; 30; 33]. Surface oxides can be removed by one or more of the following processes [30; 33]:

- Mechanical or chemical processing prior to brazing
- A preceding flux in open atmosphere brazing
- Self fluxing elements such as magnesium and phosphorus in the filler metal
- Reduction by the furnace atmosphere
- Becoming thermodynamically unstable and dissociate at temperature in vacuum furnaces

One particularly important method of joint preparation is the fluoride ion cleaning process (FIC). This method subjects the oxidized (or sulphidized) components to a highly reducing atmosphere of hydrogen and/or hydrogen fluoride at temperatures in the range of 900 to 1000°C [5]. FIC is used extensively for cleaning of wide cracks [5].

### **2.5.2 Joint Formation**

While it is important to know the specific characteristics, advantages and limitations of joining processes, it is also important to understand the kinetics of joint formation. Brazing is controlled by fast liquid flow mechanics. Solid state diffusion bonding is controlled by diffusion mechanics. Transient liquid phase bonding, on the other hand is determined by either of these mechanisms [31], and as such insight into the foundations

that govern these joining processes can be obtained by considering the kinetics of joint formation in various material systems. The success of brazing in particular depends on the ability of the liquid braze alloy to effectively wet the components that are to be joined, flowing over their surfaces and filling the gaps to form a joint free of voids.

### 2.5.2.1 Wetting

The most widely accepted method of establishing wetting behaviour is the contact angle. The Young equation [31; 33; 34], which can be derived on the basis that contact angle depends solely on the “surface tensions” of the materials states that:

$$\gamma_S = \gamma_L \cos \theta + \gamma_{SL} \quad \text{Eqn. 2-2}$$

Where  $\gamma$  is the surface tension and the suffixes S and L refer to the solid and liquid surfaces and SL refers to the solid-liquid interface, as illustrated in Figure 2-42.

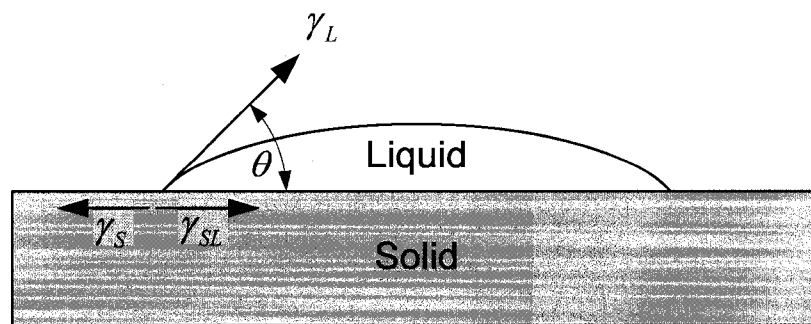


Figure 2-42 - Surface and Interfacial Tensions Acting at the Periphery of a Sessile Drop Resting on a Horizontal Solid Substrate [31; 33; 34]

#### 2.5.2.1.1 Wetting Kinetics

The initial flow of liquid metal in the channel is turbulent but as it penetrates further it slows, eventually becoming laminar and streamlined, as the flow becomes fully developed [31]. The advance of liquid in a horizontal channel of length  $t$  can be shown to follow:

$$p^2 = (W\gamma_L \cos\theta / 3\eta)t \quad \text{Eqn. 2-3}$$

Where  $p$  is the pressure applied,  $\theta$  is the equilibrium contact angle,  $W$  is the channel width and  $\eta$  is the fluid viscosity [31].

Detrimental interactions can occur that alter the surface energies and viscosities, changing the wetting and flow characteristics of the filler metal, these include:

- Alloy formation between the braze alloy and substrate
- Diffusion of substrate constituents into braze alloy
- Diffusion of braze alloy into the substrate
- Penetration of braze alloy along grain boundaries in the substrate
- Formation of intermetallic compounds such as TCP phases

These effects are strongly dependent on brazing temperature, brazing time and the materials involved, as such the effects can be minimized by [33]:

- Proper selection of braze and additive alloys
- Utilizing the lowest possible brazing temperature (but high enough to still produce flow)
- Ensuring the brazing time is short
- Cooling the brazed joint as quickly as possible without causing cracking or distortion

### ***2.5.2.2 Liquid Metal Properties***

The predictions of the behaviour of brazing methods previously described are heavily dependent on physical properties of the braze alloy. As temperature increases, the atom-atom distance also increases; this has the effect of reducing the surface energy, viscosity and density of liquid metals. Though small, these changes can have noticeable effects on penetration rates into horizontal and vertical capillary gaps [31]. Even greater variations in the physical properties of liquid metals can be produced by alloying. The liquidus temperature of binary alloys can be calculated from the Clausius-Clapeyron equation;

$$\Delta H_f(1/T_M - 1/T_L) = -R \ln N_A \quad \text{Eqn. 2-4}$$

Where  $T_L$  is the liquidus temperature of the alloy,  $\Delta H_f$  is the enthalpy of fusion of the pure solvent metal,  $T_M$  is its melting temperature and  $N_A$  is its atomic fraction, assuming there are no preferential attraction or repulsion of the solute atoms [31].

### 2.5.2.3 Oxide Removal

The wettability and capillary gap filling of braze filler by capillary action are dependent on the nature of the liquid-solid interface. Usually both the liquid and solid metals are covered with unwettable oxide films that effectively block the metal-metal contact and alter the physical properties of the liquid and solid at the interface. The most widely used methods of disrupting these oxide films are the use of fluxes, dissociation in low oxygen environments or dissolution of oxides into the substrate [31; 33]. Dissociation in low oxygen atmospheres is of particular interest in vacuum brazing where the low pressure inherently means that there is a low oxygen partial pressure.

#### 2.5.2.3.1 Vacuum Dissociation

The arbitrary oxide  $M_xO_y$  will dissociate when the partial pressure of oxygen is such that the reaction:



will proceed to the right [31]. The oxygen partial pressure required for equilibrium between the formation and dissociation of the oxide can be calculated using the free energy of formation of the oxide, given as:

$$\Delta G_{M_xO_y} = 0.5yRT \ln[pO_2] \quad \text{Eqn. 2-6}$$

where  $\Delta G_{M_xO_y}$  is the free energy of formation and  $pO_2$  is the partial pressure of oxygen [31]. As shown in Figure 2-43, the dissociation pressure varies with temperature, which is of particular relevance to vacuum brazing. During vacuum processing the total pressure is typically  $10^{-4}$  to  $10^{-6}$  mbar and the partial pressure of  $O_2$  remaining in the furnace is  $10^{-6}$  to  $10^{-8}$  mbar [31]. While the pressures within vacuum chambers may not be low enough to effectively dissociate all oxides, high vacuums do enhance the brazing of a wide range of metals that form chemically stable oxides because the rate at which oxygen arrives at the metal surface is much slower in high vacuum, reducing the rate of oxide film growth [31; 33].

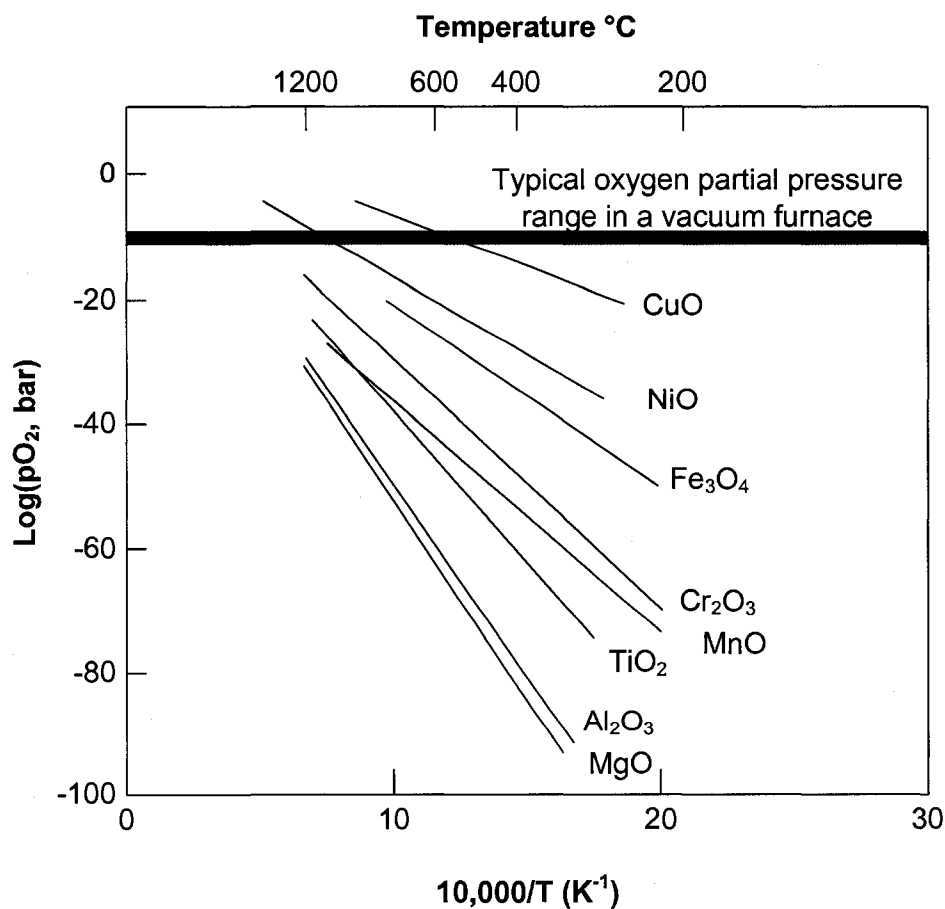


Figure 2-43 - Dissociation Pressures of Some Oxides, Adapted from [31]

## **2.6 Joint Characterization**

Repair joints must be able to withstand the various thermal and mechanical loads that caused the original damage. For the high temperature superalloys used in gas turbine engines this means the joint must have good resistance to fatigue, corrosion and creep at high temperatures. The main disadvantage to superalloy brazes is the reduced ductility of the joint due to the formation of boride and silicide chains during brazing. To ensure the performance of the repaired components, joint characterization is very important. The selection of a characterization method is highly dependent on the type of the joint and its service requirements. The three main areas of characterization are the macroscopic structure, microstructure and mechanical properties.

### **2.6.1 Macroscopic Structure**

There are essentially two types of joint. A joint can be created by direct contact of the mating surfaces of components being joined, and the more common case is a joint being created by a foreign material joining the two components together. The first type of joint is considered ideal because it is free of chemical, mechanical and physical discontinuities that would be caused by the different joining material. Shrinkage porosity, a macroscopic defect is caused by the use of excessive braze alloy, this porosity forms as a result of the temperature gradients during cooling, which cause the free surface to solidify prior to the interior [31].

#### ***2.6.1.1 Non-Destructive Inspection***

Non-destructive inspection techniques (NDT) can be used to assess the quality of the macroscopic structure of a joint, in particular the extent of filling, the degree of porosity

and the existence of large cracks [4; 31; 33]. NDT methods are particularly useful to assess the size, location and reparability of flaws, and to monitor the service conditions of parts during shut downs. Typical repair defects that can be observed using NDT methods include [5; 33]:

- Oxide residues on the brazed surfaces preventing wetting and flowing, which may cause local non-wetted pockets in the crack filling.
- Voids, microvoids, pores especially when paste type of fillers are used
- Shrinking of the brazing alloy, resulting in poor gap filling
- Cooling hole obstruction by braze alloy as a result of repair

The simplest non-destructive technique is visual inspection. The use of dye penetrants allow for smaller cracks to be detected. One particularly NDT method for characterizing braze joints is ultrasonic inspection, which can detect discontinuities such as voids and cracks as shown in Figure 2-44. Other NDT methods include liquid penetrant inspection, eddy current inspection, radiographic inspection, holographic inspection, magnetic particle inspection and microwave inspection [62].

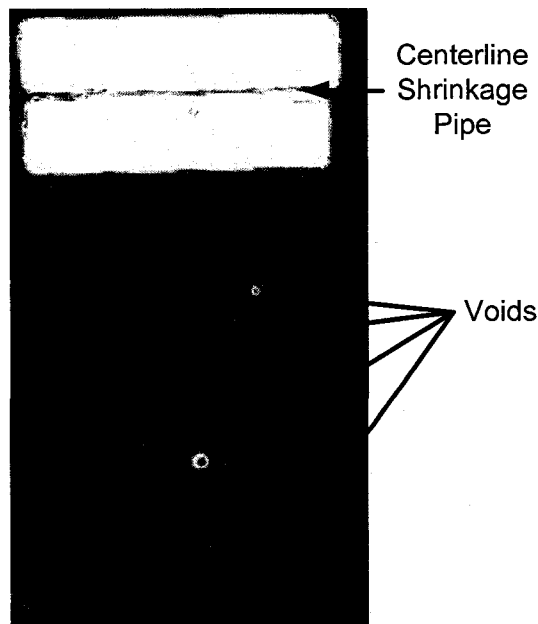


Figure 2-44 - Ultrasonic Evaluation of as Cast 1 inch Square X-40 bar

### **2.6.2 Microstructure and Chemistry**

While a joint may possess satisfactory macroscopic characteristics, its performance may still be poor due to microscopically small features such as inclusions, unbonded interfaces, cracks and chemistry, all of which strongly influence mechanical properties and environmental resistance [31]. The joint can also be much weaker than the base material; the existence of brittle boride chains in a continuous central layer produced in NGB operations can be especially detrimental. The ideal microstructure of a joint is such that it closely resembles the base material in chemistry and mechanical properties. Insight about the microstructures, microchemistry and observations of the joint formation kinetics can be made using optical and/or scanning electron microscopy with Energy Dispersive X-ray Spectrometer (EDS) or Wavelength Dispersive X-ray Spectrometer (WDS) capabilities. Such processes require the removal of sections of the joint and their subsequent mechanical and chemical polishing. Metallographic inspection is particularly useful for detection of flaws such as porosity and poor flow of braze alloy [33].

The formation of reaction product layers at interfaces often occurs when joining dissimilar component materials or when using a filler metal that differs greatly from the base metal, and are formed due to different reaction rates [31]. Eutectic structures such as those shown in Figure 2-36 can form due to the great multiplicity of elements in braze compositions, forming during solidification as the temperature falls below the liquidus of the eutectic [31]. Most brazes are based on eutectic compositions and similar microstructures can be found commonly for binary and more complex fillers [31]. Microstructural changes can form not only at the interfaces but also within the interiors

of the joint due to complex chemistries and interdiffusion at the interface, these microstructural changes can cause intermetallic layers to form [31].

### 2.6.3 Mechanical Properties

The basic requirement of a joint is that it must be strong and tough. Repair joints must endure the conditions that caused the damage to the original component. Brazed joints are generally assessed on their ability to withstand increasingly severe stresses during tensile, bend or shear tests, prolonged steady stresses at high temperatures during creep or stress rupture tests, varying or evenly oscillating stresses during fatigue tests, suddenly imposed stresses during impact tests or indentions by hardness tests [31].

Joint design can have a profound effect on the mechanical properties. The stress rupture strength of a joint is inversely proportional to the width of the joint gap, as is shown in Figure 2-45. According to Hill's slip line theory of 1950 [31], inelastic deformation of perfectly bonded joints will not occur until the stress exceeds

$$\sigma_J = 0.5\sigma_Y \left( \frac{W^*}{h^* + 3} \right) \quad \text{Eqn. 2-7}$$

where  $\sigma_Y$  is the tensile yield stress of the joint material,  $W^*$  and  $h^*$  are the width and thickness of the joint respectively [31]. Strong joints depend on perfect bonding, as such the joint strengths will peak at the smallest thickness at which perfect bonding can be achieved [31].

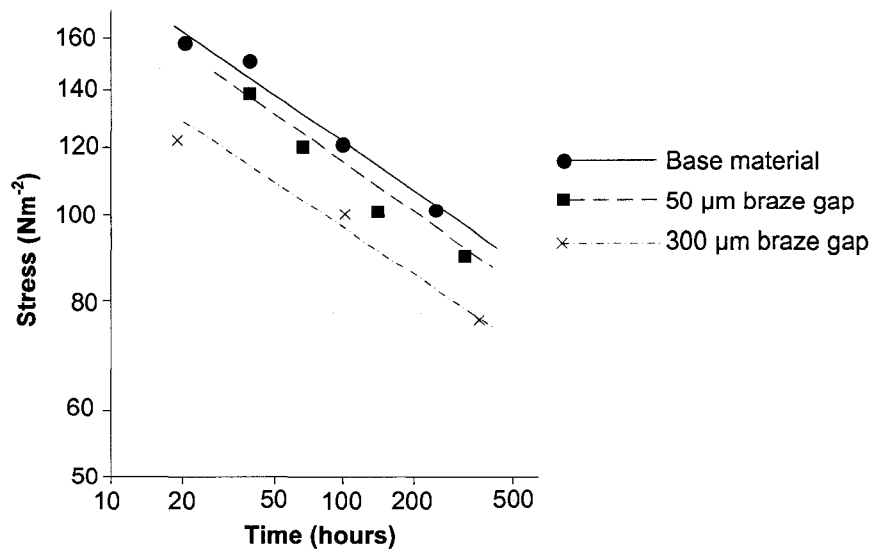


Figure 2-45 - Creep Rupture Test at 980°C on Braze Repaired Crack in C1023, Adapted from [3]

When considering the effect of material selection on joint strength it is important to consider effect of interactions between the substrate and filler metals. Usually material selection provides the widest range of possibilities for varying the mechanical properties of joints, as such attention must be paid to the effect of material selection. Removing/reducing melting point depressants from the joint means the substrate becomes alloyed with these embrittling elements, the effect of such alloying depends on the elements involved but usually is detrimental. Brazed superalloy components are usually brittle in their as received form, but their ductility can be improved by appropriate diffusion heat treatment cycles [4; 31].

## 2.7 Summary

The cost savings that can be attained by employing a gas turbine hot section component repair scheme is quite significant, especially for operators of multiple engines. The increased temperature in modern gas turbine engines has led to increased cooling techniques which in turn have led to complex geometries, making weld repair of these

components quite difficult. While solid solution hardened alloys such as cobalt-base superalloy X-40 were originally chosen due to their relatively high weldability, it can be expected that NGB and WGB repair joints can produce comparable, if not improved joint characteristics with the benefit of batch processing. As such, diffusion braze repair of the hot section components of modern and aging gas turbines can be expected to continue.

### **Chapter 3. Research Objectives**

The research work discussed in this thesis can be divided into two general headings, narrow gap brazing and wide gap brazing. The purpose of this research is to develop and assess the applicability of repairing cobalt-base superalloys with nickel-base filler alloys, with the expectation of achieving improved high temperature mechanical properties.

The purpose of the narrow gap braze work is to evaluate the suitability of nickel-base braze alloys for crack healing and attachment of airfoil inserts for hot section gas turbine components made of cobalt-base superalloy. The narrow gap braze work also provides preliminary insight into the wide gap braze work through microstructural examination of the narrow gap braze joints, high temperature tensile behaviour and morphology of the associated tensile fracture surfaces.

The purpose of the wide gap braze work is to evaluate the possibility of using nickel-base additive alloys, IN-738 in the case of this thesis, for wide gap braze repair of large defects (i.e., ground cracks and foreign object damage) in hot section gas turbine components made of cobalt-base superalloys. Evaluation of the wide gap braze joints was performed through microstructural examination, high temperature tensile and low cycle fatigue testing and fractography of the associated fatigue fracture surfaces.

The final objective of this research is to evaluate the equivalency of high temperature tensile tests to the life of a repair joint, a practice which is common in industry.

## Chapter 4. Methodology

### 4.1 Research Materials

#### 4.1.1 Superalloy Bars

Vacuum cast and hot isostatic pressed X-40 and IN-738 superalloy bars, such as those shown in Figure 4-1 were graciously made available for this research by the Institute for Aerospace Research of the National Research Council of Canada (NRC-IAR). The nominal compositions of these alloys are shown in Table 4-1. It should be noted that the X-40 bars contained a trace amount of zirconium.

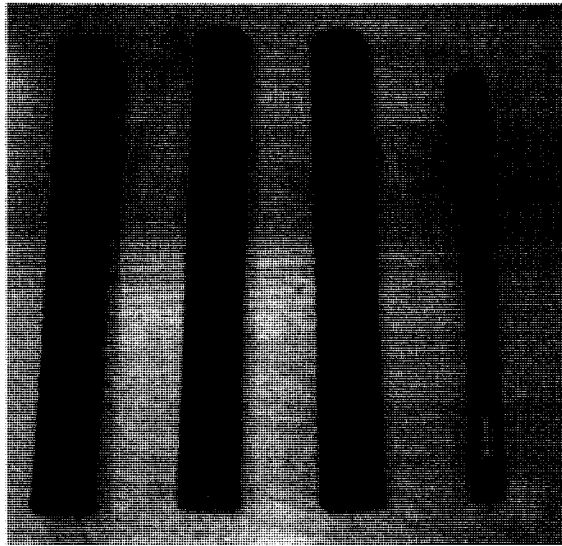


Figure 4-1 - Vacuum Cast and Hot Isostatic Pressed X-40 Bars

Table 4-1 - Nominal Composition of Alloys Used In This Study

Alloy	Al	B	C	Co	Cr	Fe	Mn	Mo	Nb	Ni	Si	Ta	Ti	W	Zr
X-40	-	-	0.5	Bal.	25	1.5	-	-	-	10	-	-	-	7.5	-
IN-738	3.4	0.01	0.17	8.5	16	-	0.01	1.75	0.9	Bal.	0.01	1.75	3.4	2.6	0.1
BNi-9	-	3.5	-	-	15	-	-	-	-	Bal.	-	-	-	-	-

#### 4.1.2 Powders

Three alloy powders were used in this study, all of which were obtained from Praxair Surface Technologies Inc. The product numbers of these gas atomized powders are

shown in Table 4-2. The braze alloy used in this study, BNi-9, has solidus and liquidus temperatures of 1020 and 1050°C respectively and a brazing temperature of 1200°C. BNi-9 was selected as a braze alloy because of its compositional simplicity and because braze alloys of similar simple composition are extensively used in industry.

**Table 4-2 – Product Numbers of Alloy Powders Used in This Study**

Alloy	Purpose	Praxair Product No.
BNi-9	Braze Alloy	NI-276
X-40	Additive Powder	CO-285
IN-738	Additive Powder	NI-284

#### **4.1.3 Brazing Binder**

Nicrobraz 520 braze cement from the Wall Colmonoy Corporation was used as a binding agent in this study. Nicrobraz 520 is a mixture of solvent (1,3-Dioxolane), plastic (5-35%) and stabilizers (1-3%). The exact chemistry of Nicrobraz 520 is protected by trade secrets.

## **4.2 Analytical Methods and Equipment**

### **4.2.1 Brazing and Heat Treatment**

#### ***4.2.1.1 Narrow Gap Braze Specimen Preparation***

Narrow gap braze specimens were prepared from X-40 and IN-738 superalloy bars with BNi-9 braze alloy in the configuration shown in Figure 4-2. Bars were machined to size and ultrasonically cleaned, to remove any contaminants. The bars were then tack welded with a nominal gap of 50  $\mu\text{m}$ , maintained by stainless steel shims. Following welding, the stainless steel shims were removed and the samples were swabbed with acetone to remove contaminants introduced during welding, then dried completely. A bead of braze paste was applied to the periphery of the bars as shown in Figure 4-2.

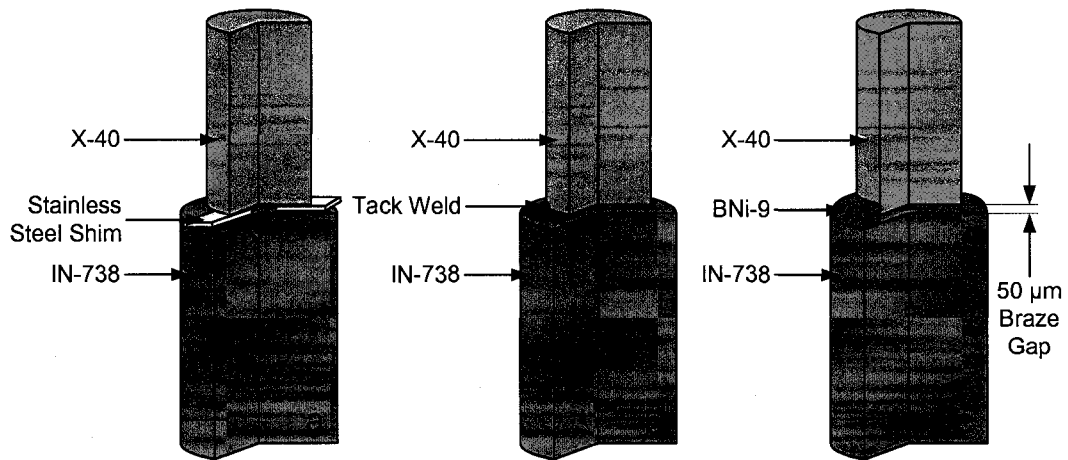


**Figure 4-2 - Narrow Gap Braze Test Specimen Manufacture Process, (a) Stainless Steel Shims Inserted, (b) Bars Tack Welded in Several Places and Shims Removed, (c) Bead of Braze Alloy Slurry Syringed Around Braze Gap**

#### **4.2.1.2 Wide Gap Braze Specimen Preparation**

Wide gap braze coupons were prepared by machining a groove into X-40 bars with a nominal thickness of 6.35 mm (1/4 in.) to a depth of approximately 75% of the diameter of the bar, as shown in Figure 4-3. Following machining the bars were thoroughly cleaned for tape (in the case of IN-738 additive alloy) or slurry (in the case of X-40 additive) insertion.

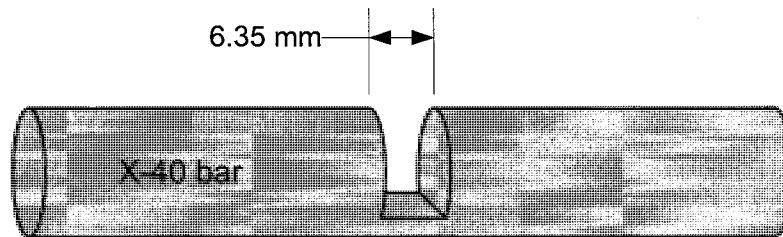


**Figure 4-3 - X-40 Bar Cut for Slurry/Tape Insertion**

In the case of wide gap brazing with X-40 additive powder, a mixture of X-40 additive alloy and BNI-9 braze alloy in a nominal 2:1 ratio were combined with binder in a mechanical mixer to form a slurry. This slurry was packed into grooved X-40 bars, as

shown in Figure 4-4, and allowed to fully dry. Excess brazing slurry was placed around packed groove to accommodate shrinkage from binder evaporation.

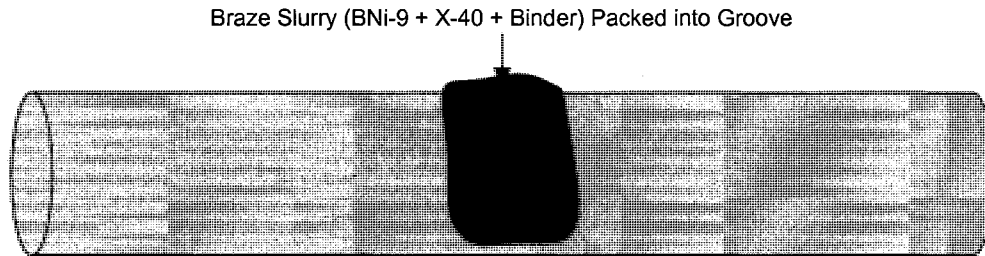


**Figure 4-4 - WGB X-40 Additive Specimen Prepared for Brazing**

In the case of wide gap brazing with IN-738 additive powder, preparing and packing the joint with a slurry was attempted, however the specimens failed during machining of test coupons due to the occurrence of high amounts of porosity. To reduce this porosity, braze tapes were produced and placed in the grooved X-40 bars for brazing. Tapes were produced by the tape casting process shown in Figure 4-5. The tape casting mould was filled with a slurry consisting of either the braze alloy or additive alloy and binder (2), this slurry was then manipulated into the length of the mould, ensuring an even fill of the mould (3). The slurry was allowed to fully dry into a tape (4) which was then extracted from the mould (5). Alternating layers of braze alloy and additive alloy tapes with a nominal thickness of 1 mm (approx 0.04 in.) were arranged in the groove according to the sequence BAABAAB, where B represents the braze alloy tapes and A represents the additive alloy tapes, as shown in Figure 4-6. Excess tape was trimmed after insertion and additional tapes were added to accommodate shrinkage.

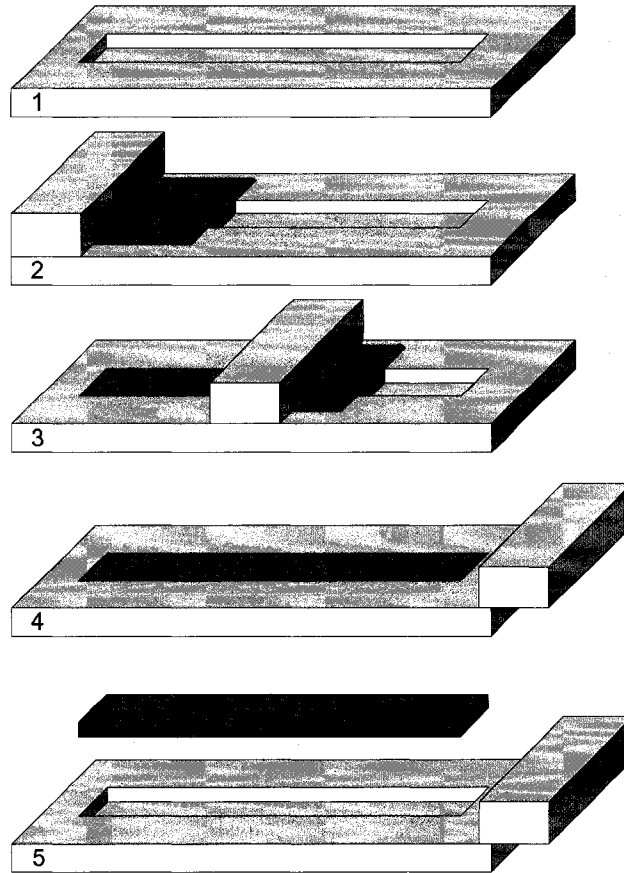


Figure 4-5 - Tape Casting Process

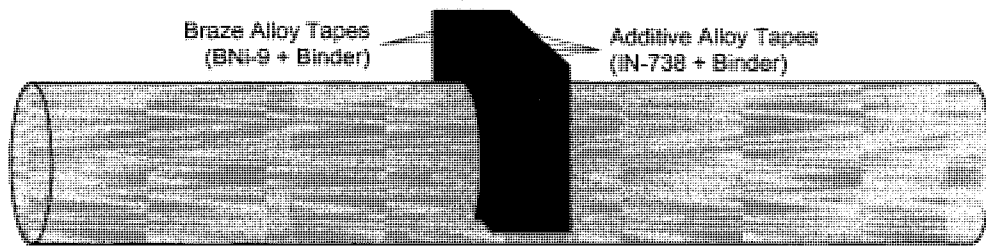
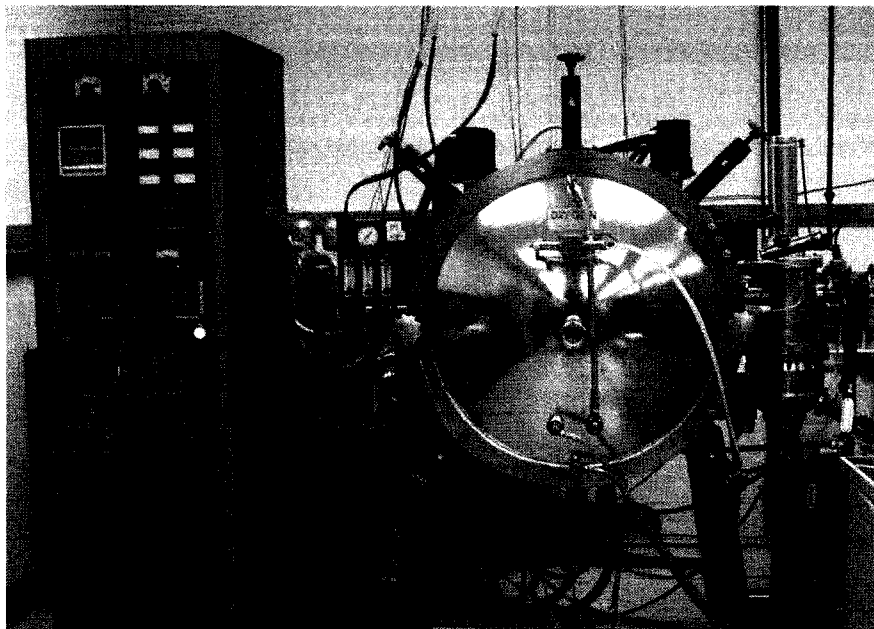


Figure 4-6 - WGB IN-738 Additive Specimen Prepared for Brazing

#### 4.2.1.3 Braze Cycle and Isothermal Heat Treatment

The narrow gap braze specimens were vacuum brazed between  $10^{-5}$  and  $10^{-6}$  Torr in an Oxy-Gon vacuum furnace shown in Figure 4-7 following the braze cycle shown in Figure 4-8. Samples were brazed in the center of the furnace in a ceramic container to ensure uniform heating. The furnace was purged with argon three times prior to brazing to

minimize contamination. Following brazing, specimens were allowed to cool to room temperature under vacuum. Brazing of the narrow gap braze specimens was carried out at the National Research Council's Institute for Aerospace Research. Isothermal exposure of the NGB specimens was performed in air in a radiation furnace at 950°C for between 120 and 840 hours. Brazing of the wide gap braze specimens was performed by Liburdi Turbine Services using a similar vacuum furnace and the same brazing cycle shown in Figure 4-8.



**Figure 4-7 - NRC-IAR-SMPL Oxy-Gon Vacuum Furnace**

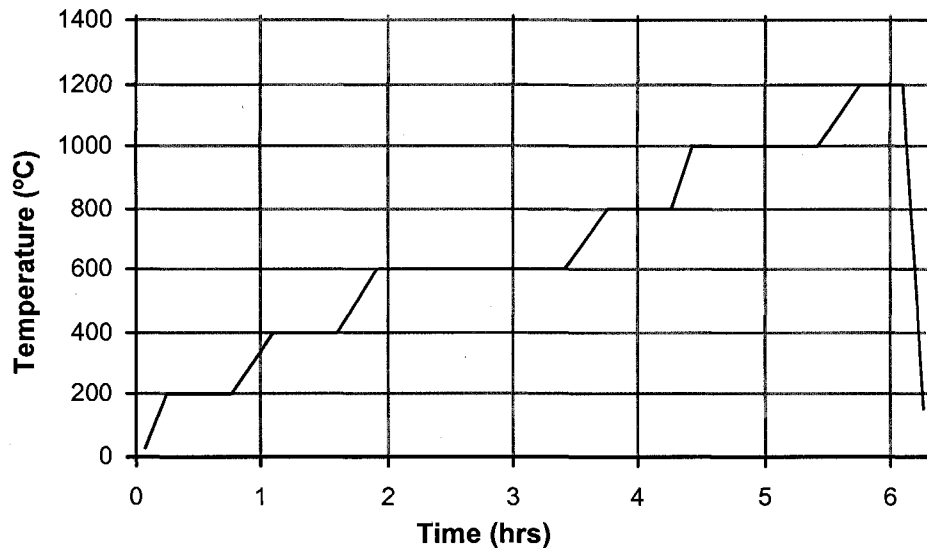
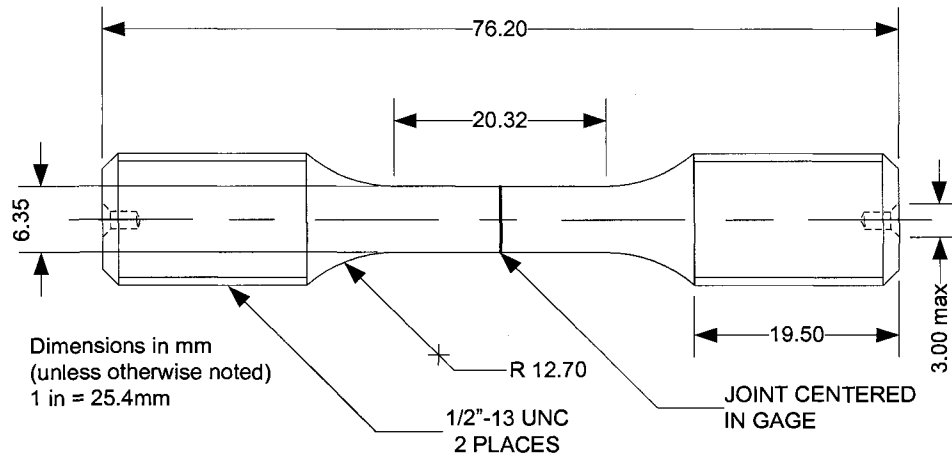


Figure 4-8 - Braze Cycle

#### 4.2.2 Mechanical Testing Specimen Preparation

Mechanical test coupons were machined from the as-brazed and heat braze NGB specimens and the as-brazed WGB specimens. The specimen geometry, shown in Figure 4-9 was developed using ASTM E606[63] as a guideline, the full specimen drawing can be seen in Appendix A. The length of the threaded region of the test coupon geometry used was slightly shorter than suggested in ASTM E606. This reduction in thread length was due to a limited amount of material available. However, as there was no intention of generating design data and the threads were more than capable of carrying the load for gripping purposes, this discrepancy was deemed acceptable.



**Figure 4-9 - Mechanical Testing Coupon Geometry**

NGB mechanical test coupons were machined on a computer numerical controlled lathe at the Carleton University Mechanical and Aerospace Engineering Department Machine Shop and WGB coupons were machined at Liburdi Turbine Services of Hamilton, Ontario. Following inspection, all test coupons were manually polished using silicon carbide sand paper grits 180, 240, 320, 400 and 600 with ultrasonic cleaning in distilled water and acetone between each polishing step. Polishing was performed in the longitudinal direction to eliminate circumferential scratches in the specimen gage section. Following the final gage section polishing step, the diameter of the specimens was measured using a Mitutoyo model 547-500 digital micrometer, shown in Figure 4-10. Extreme care was taken to ensure the specimens were not scratched during measurement.



Figure 4-10 - Mitutoyo Digital Micrometer

### 4.2.3 Mechanical Testing

Mechanical Testing was carried out on the MTS 810 test frame shown in Figure 4-11.

The main components of the test frame are the model 680.01B high temperature threaded grips, the model 653.04A high temperature furnace assembly and the model 632.41C High temperature extensometer. The load was applied by a hydraulic cylinder which was controlled by a servo valve, which in turn was controlled by the computerized system shown in Figure 4-12. The load applied to the specimen was measured by an MTS model 661.20E 25 kN load cell.

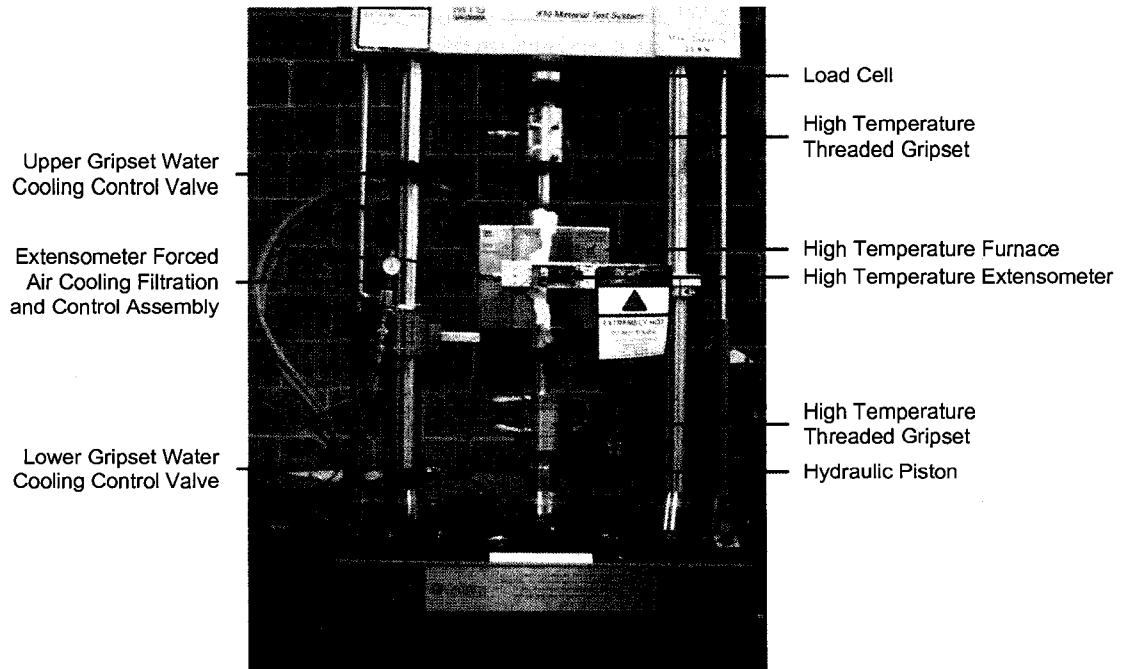
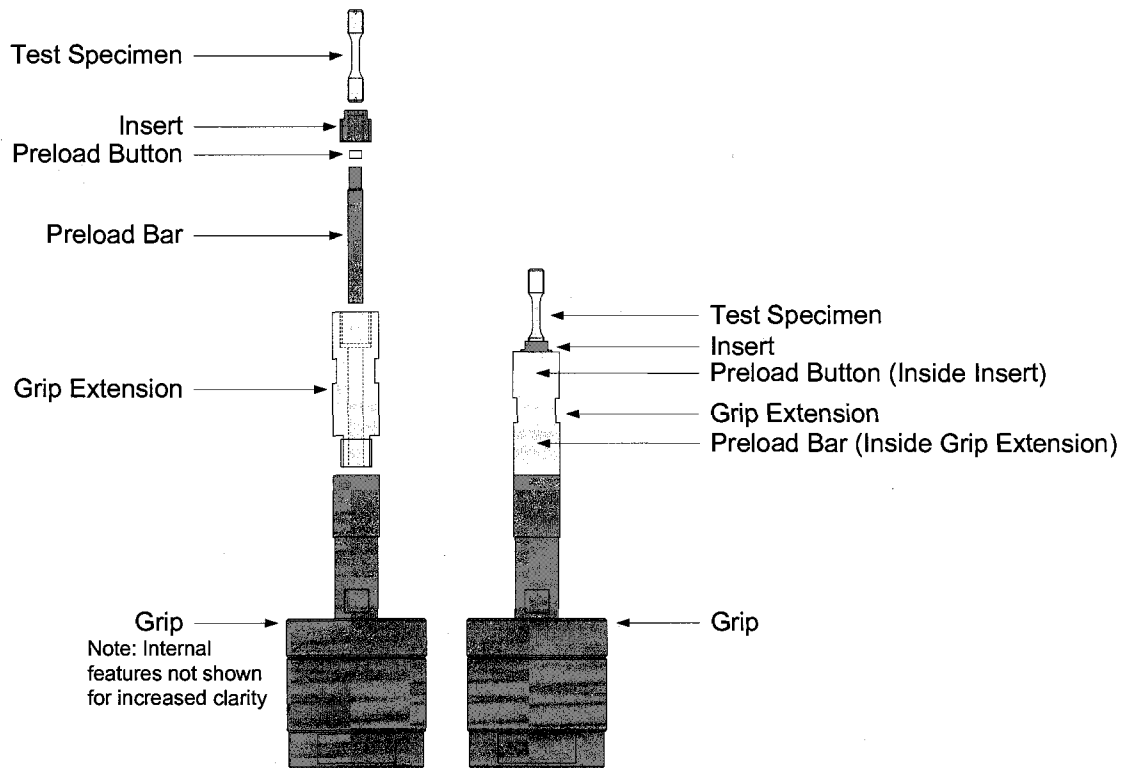


Figure 4-11 - High Temperature Materials Testing Frame at Carleton University



**Figure 4-12 - MTS TestStar IIs Control System at Carleton University**

As mentioned previously, the grips used for this work were MTS model 680.01B high temperature threaded grips. These grips have a specified maximum specimen temperature of 1000°C and while this temperature is above the test temperature of this work, efforts were made to extend the life of the grips as they are quite expensive. In addition to the water cooling system, the grip extensions shown in Figure 4-13 were borrowed from the National Research Council, limiting the amount of grip material exposed to high temperature. The configuration of the additional components used to extend the life of the grips is shown in Figure 4-13 and the full drawings of these parts are available in Appendix A.



**Figure 4-13 - High Temperature Mechanical Test Grip Assembly**

The heat source used for mechanical testing was an MTS model 653.04A high temperature furnace assembly shown in Figure 4-11. To minimize the amount of fracture surface oxidation following specimen failure, a relay system was assembled to take advantage of an unused control output of the MTS TestStar IIs controller. This relay system disabled the high temperature furnace the instant the hydraulics were switched off (which occurred when a specimen break was detected). The wiring diagram of this relay system is shown in Figure 4-14.

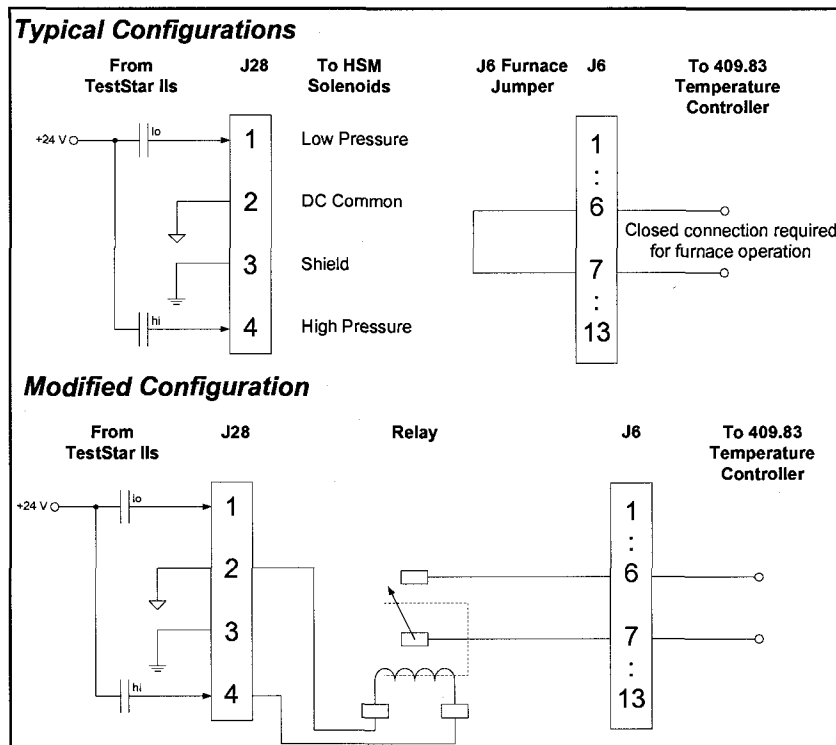
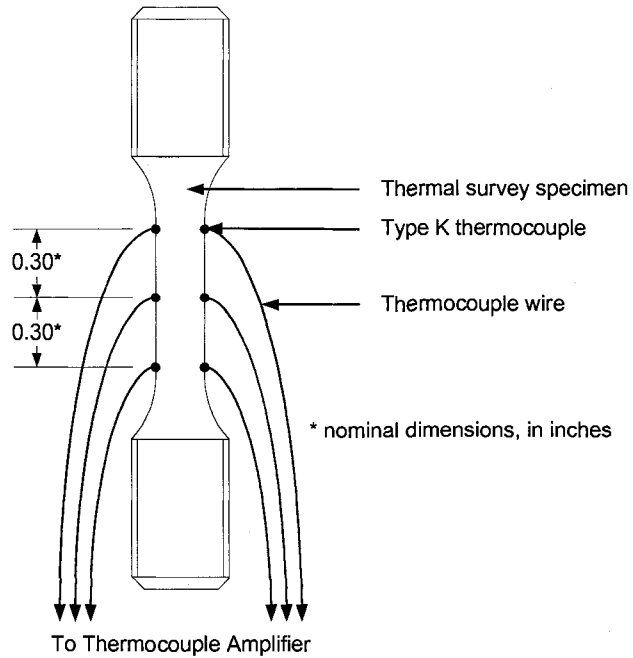


Figure 4-14 - Furnace Automatic Shutoff Wiring Diagram

#### 4.2.3.1 Thermal Survey

To achieve a uniform metal temperature of 950°C on the surface of the test specimen, a thermal survey was performed. A thermal survey is performed by matching as many of the variables as possible (other than loading) while varying the heat input by adjusting the furnace setpoints to achieve the desired steady state metal surface temperature. For this work, 6 type K thermocouples were spot welded to a 304 stainless steel specimen matching the dimensions of the test specimens as shown in Figure 4-15. The extensometer was in place and all cooling equipment was used for this thermal survey. Thermocouple output voltage was read by a Stanford Research Systems model SR630 16 Channel Thermocouple Monitor, shown in Figure 4-16. Temperature versus time data was collected on a personal computer through the thermocouple monitor's serial data

port. This data was used to determine the furnace setpoints and the time required for the specimen to reach the desired 950°C.



**Figure 4-15 - Thermal Survey Coupon**

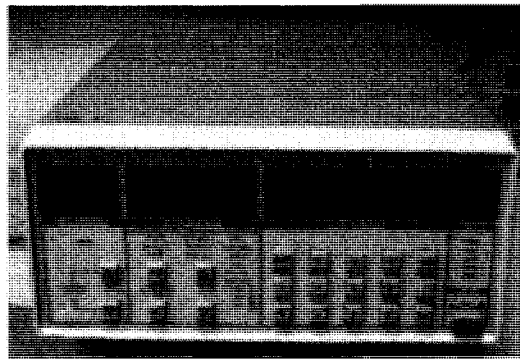


**Figure 4-16 - Stanford Research Systems Thermocouple Monitor**

#### **4.2.3.2 Extensometer Calibration**

The model 632.41C High temperature extensometer was calibrated before testing using a Mitutoyo model 3590 extensometer calibration device. The calibration report for the extensometer is available in Appendix B.

#### **4.2.3.3 Tensile Testing**

Isothermal tensile testing of NGB specimens was carried out at a loading rate of 445 N/s (100 lbs/sec) and tensile testing of WGB specimens was carried out at a loading rate of 200 N/s. The lower loading rate used for the WGB specimens was employed to reduce the amount of extensometer slip that can occur during testing. Tensile testing of NGB specimens was carried out at NRC-IAR and tensile testing of WGB specimens was carried out at Carleton University. All tensile tests were carried out at 950°C.

#### **4.2.3.4 Low Cycle Fatigue Testing**

Isothermal low cycle fatigue testing was carried out with stress amplitude,  $\Delta\sigma/2$  of 75% of the average yield strength of the baseline X-40 bars and, with a mean stress of zero. The loading was fully reversed with a frequency of 0.5Hz following a sinusoidal waveform as shown in Figure 4-17. All low cycle fatigue tests were carried out at 950°C.

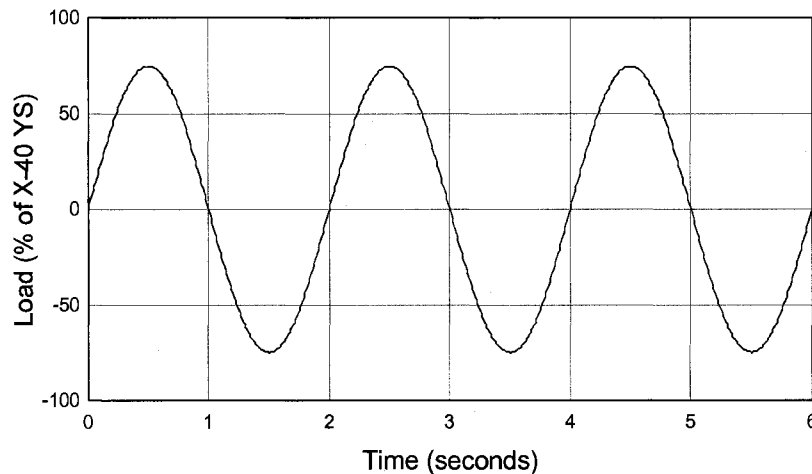


Figure 4-17 - LCF Test Loading Waveform

#### **4.2.3.5 MTS MultiPurpose TestWare® Program**

Figure 4-18 shows the MultiPurpose TestWare (MPT) program used to conduct low cycle fatigue testing and Table 4-3 describes the purpose of each of the program blocks used.

The program used to conduct tensile testing is not shown as it is somewhat simpler than the fatigue test program. It should also be noted that MPT ends its current test once any of the specified limit or error detectors is tripped. For this work, displacement limit and load error were selected as test ending situations, that is, when the vertical position of the hydraulic cylinder passed a certain point or when the difference between the command load and the actual load exceed a predetermined amount, the test would end.

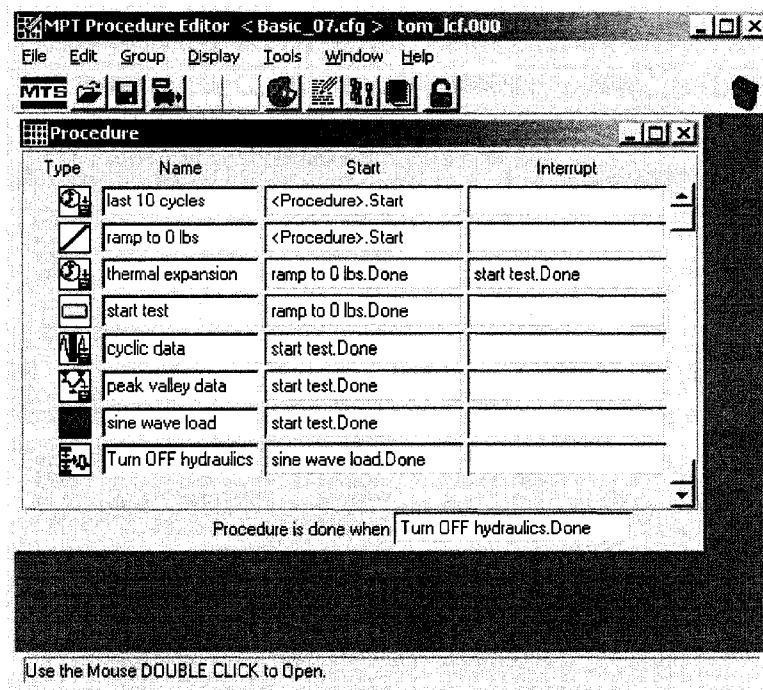


Figure 4-18 - MultiPurpose TestWare LCF Test Program

Table 4-3 - MultiPurpose TestWare Program Block Descriptions

Block Name	Symbol	Explanation
Last 10 cycles		The timed data collection feature was used to obtain data on the last 10 cycles in the life of the test specimens. This was done by selecting the circular data collection method which overwrites old data with new when a buffer is filled. Using a sampling rate of 1/50 <sup>th</sup> of the test frequency and a buffer size of 500 data points, the load, strain and displacement of the last 10 cycles were recorded.
Ramp to 0 lbs		At the beginning of the test, the ramping load feature was used to begin the test in the unloaded condition. The controller then maintains this load until another load command is called.
Thermal expansion		The timed data collection feature was used to obtain data on the thermal expansion of the test coupon as it was brought to 950°C. Heating typically took 90 minutes, thus sampling every 15 seconds produced about 360 data points, yielding a smooth curve but not taking up too much memory.
Start test		The control button feature was used to prompt the operator to turn on the furnace and press a button once the testing temperature was achieved. When the button was depressed, the thermal expansion data collection was disabled and the cyclic data, peak/valley data and sine wave loading commands were initiated.
Cyclic data		Data was collected using the cyclic data collection feature. The logarithmic data collection mode was selected, which collects data on the cycles 1, 2, 3, ..., 8, 9, 10, 20, 30, ..., 80, 90, 100, 200, 300, ..., 800, 900, 1000 and so on. This type of data collection provides valuable insight into cyclic hardening and softening.
Peak valley data		Data was also collected using the peak/valley data collection feature. A reversal limit was specified and once this limit was exceeded, the data at the maximum/minimum is recorded. This data collection feature allows for the easy plotting of the maximum and minimum load lines and provides a valuable check if any error was to occur during testing.
Sine wave load		The cyclic loading command was used to generate the load command for testing. A sinusoidal wave form with a frequency of 0.5 Hz was selected to limit the amount of extensometer slip. A maximum number of cycles was selected to be 250,000 cycles, once this cycle count is reached, the loading returns to 0 and the test was ended
Turn OFF hydraulics		The interlock command feature was used to disable the hydraulics if the test reached the maximum number of cycles. As mentioned previously, the high temperature furnace was also switched off when the hydraulics were disabled.

## 4.2.4 Post Test Analysis

### 4.2.4.1 Sample Preparation

Following removal from the grips, samples were examined optically at low magnification using the Nikon SMZ 1000 stereoscope shown in Figure 4-19. Images of the fracture surface and profile of the specimen were taken at 10, 20 and 40 times magnification to be used later for reference. Fracture surface images were used to calculate the reduction in area that occurred during tensile testing.

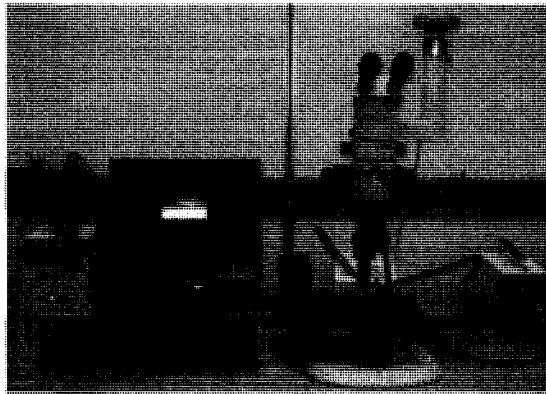
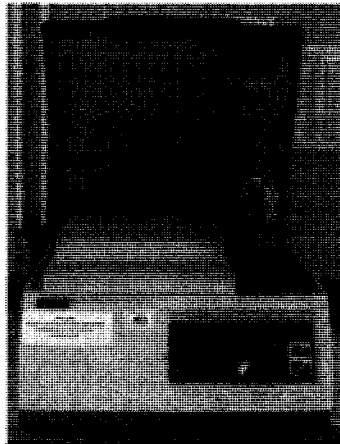
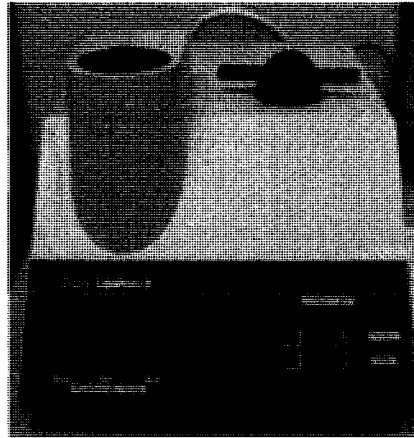


Figure 4-19 - Nikon SMZ1000 Stereoscope

Following optical examination, specimens were prepared for Scanning Electron Microscopy examination and microhardness testing. Selected specimens were shortened so the fracture surface could be examined while others were sectioned for microstructural analysis using the Buehler ISOMET 2000 precision saw shown in Figure 4-20. Microstructural analysis specimens were then mounted in Bakelite using the Struers LaboPress 3 specimen mounting press shown in Figure 4-21.



**Figure 4-20 - Buehler ISOMET 2000 Precision Saw**



**Figure 4-21 Struers LaboPress 3 Specimen Mounting Press**

Microstructural analysis specimens were polished using the Buehler ECOMET IV Polisher/Grinder shown in Figure 4-22. Sample preparation involved wet grinding using 180, 240, 320, 400 and finally 600 grit silicon carbide abrasive papers followed by polishing using 6 and 3 micron Beta Diamond Products diamond polishing suspensions followed by final polishing with a colloidal silica suspension. Specimens were ultrasonic cleaned between each polishing step in distilled water and acetone to remove particulates. The polishing cloths used with each of these suspensions can be seen in Table 4-4. While this polishing sequence was long and time consuming, it was necessary to reduce the amount of pullout that occurred during polishing. Between each polishing

step and after final polishing the specimens were inspected using the Olympus PMG3 optical microscope shown in Figure 4-23.

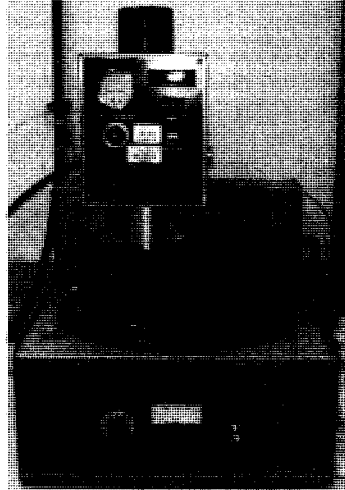


Figure 4-22 – Buehler ECOMET IV Polisher/Grinder

Table 4-4 - Polishing Cloths used with Diamond and Silica Suspensions

Suspension	Polishing Cloth
6 micron diamond	Buehler Texmet 1500
3 micron diamond	Struers DP-Dac
Colloidal Silica	Struers MD-Chem

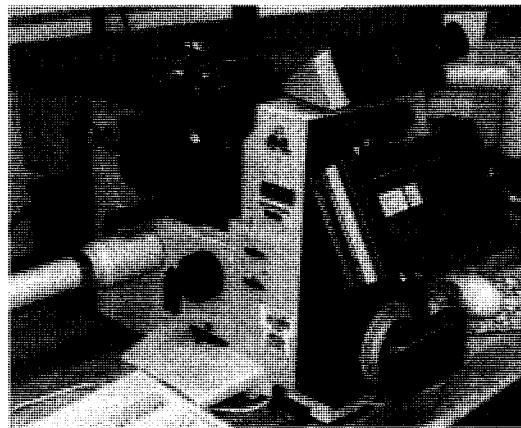


Figure 4-23 - Olympus PMG3 Optical Microscope

#### **4.2.4.2 Scanning Electron Microscopy**

Microstructural examination was carried out using a Phillips XL30-SFEG Ultrahigh resolution scanning electron microscope (SEM). Secondary electron (SE) and

backscatter electron (BSE) images were prepared and energy dispersive spectroscopy (EDS) element maps were prepared.

#### **4.2.4.3 Microhardness Testing**

Following microstructural examination, the microhardness of the as-brazed NGB and WGB specimens was measured on a LECO LM247AT microhardness tester using standard techniques. Nano-indentation testing was performed on a CMS Instruments nano-hardness tester, shown in Figure 4-25.

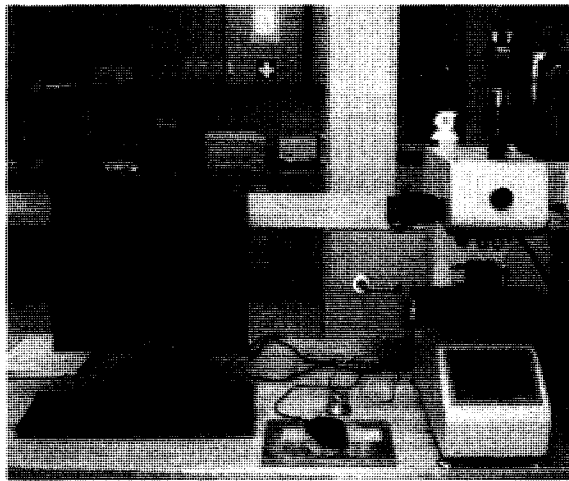


**Figure 4-24 - LECO LM 247AT Microhardness Tester**

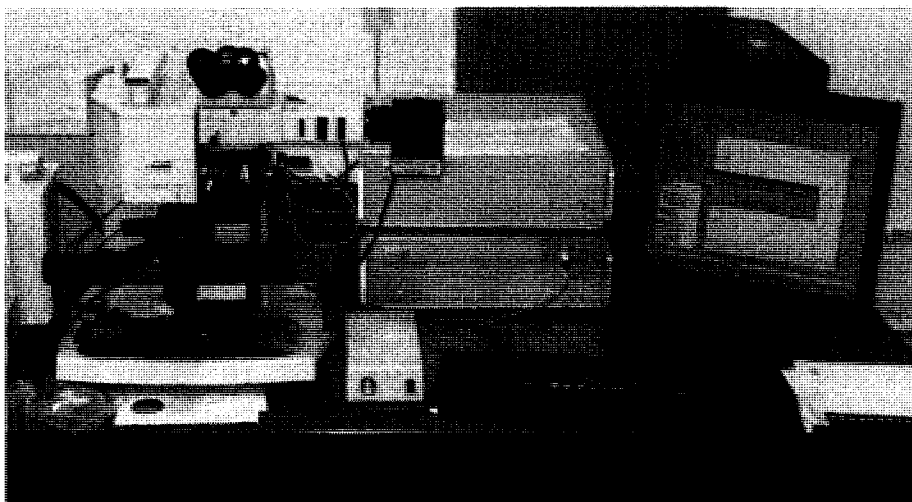


**Figure 4-25 – CMS Instruments Nano-Hardness Tester**

## **Chapter 5. Experimental Results and Discussion**

### **5.1 Baseline X-40 Bars**

The microstructure of the X-40 baseline material used in this study, includes a cobalt matrix and several carbide phases, identified in Figure 5-1. As expected, the matrix identified in Figure 5-1 contained a high concentration of cobalt, chromium and nickel, the relative amounts of which are given in Table 5-1. Of the carbides, the visually darkest, identified in Figure 5-1, contained a high concentration of chromium with moderate amounts of other elements (Co and Ni). A slightly lighter carbide phase was identified as primarily containing chromium and tungsten. The third type carbide phase identified contained a significant amount of zirconium. The averaged EDS results and representative spectrums of these phases are shown in Table 5-1. Light, nonmetallic elements (C, O and B) were included in the EDS analysis carried out in this study, the results however only provided qualitative measures as the instrument was not capable of detecting light elements. The concentration of oxygen in the phases could be significantly affected by sample surface contamination.

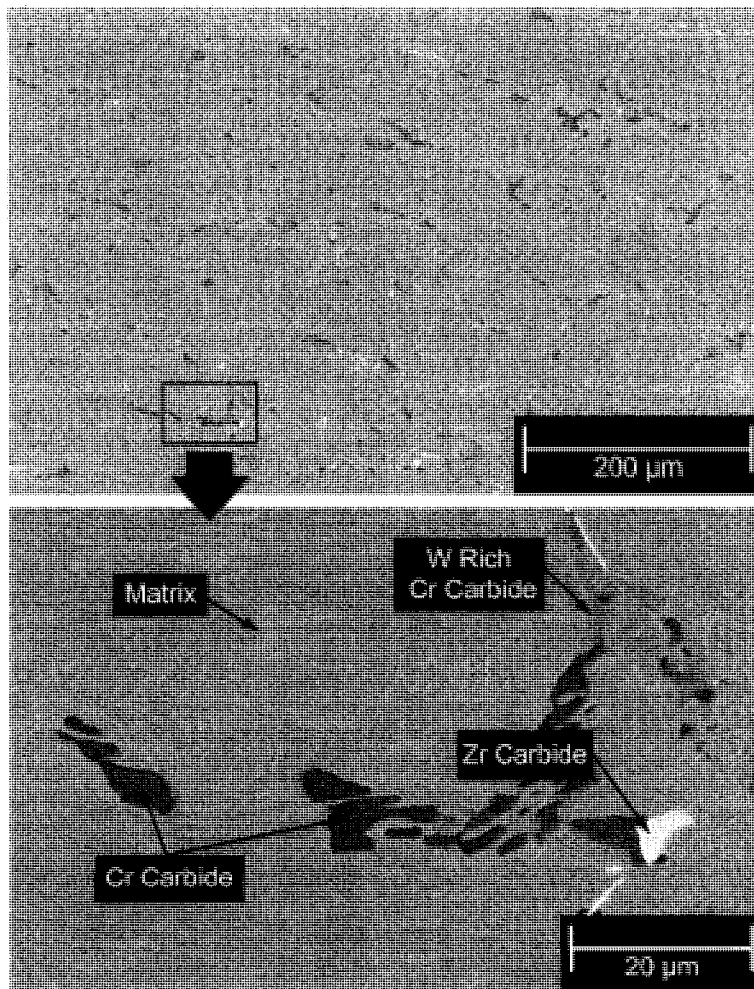
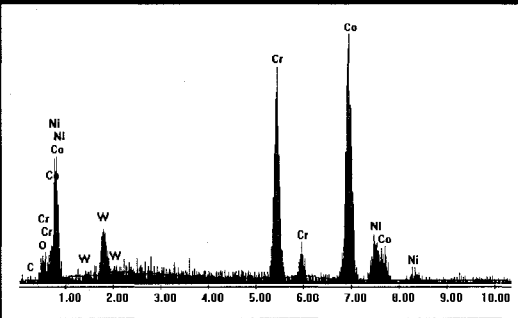


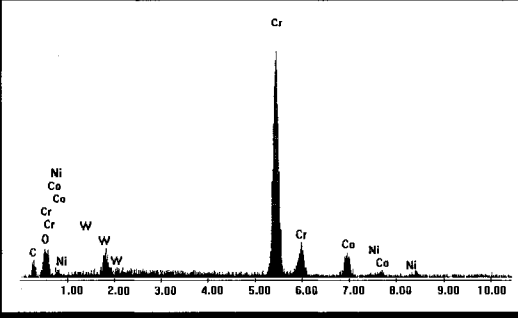
Figure 5-1 - Phases of X-40 Bars Used In This Study

Table 5-1 - Averaged EDS Results of Phases in X-40 Used in This Study (L, K and M Denote Energy level)

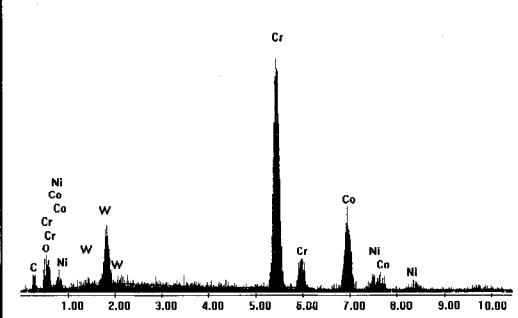
Bulk Matrix		
Element	wt%	at%
C K	1.71	7.75
O K	2.35	8.02
W M	11.98	3.57
Cr K	22.35	23.48
Co K	51.63	47.88
Ni K	10.00	9.31
Total	100.00	100.00



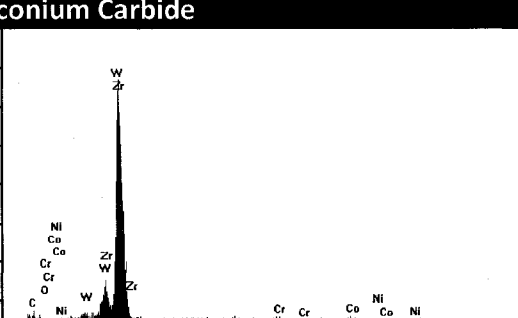
Chromium Carbide		
Element	wt%	at%
C K	12.26	36.21
O K	5.80	12.87
W M	8.30	1.61
Cr K	61.16	41.79
Co K	10.52	6.33
Ni K	1.98	1.20
Total	100.00	100.01



Tungsten Rich Chromium Carbide		
Element	wt%	at%
C K	8.00	28.46
O K	4.68	12.49
W M	17.67	4.11
Zr L	0.54	0.25
Cr K	46.79	38.44
Co K	18.16	13.22
Ni K	4.18	3.05
Total	100.01	100.01



Zirconium Carbide		
Element	wt%	at%
C K	16.04	59.36
O K	0.57	1.56
W M	14.75	3.51
Zr L	63.21	31.28
Cr K	2.08	1.76
Co K	2.48	1.87
Ni K	0.86	0.66
Total	100.00	100.00



## 5.2 Narrow Gap Diffusion Brazing

### 5.2.1 As-Brazed Condition

The as-brazed narrow gap braze joint contained no visible defects, as shown in Figure 5-2. The braze gap was completely filled by the braze alloy via capillary action during brazing. As shown in Figure 5-3, the braze region (bounded by dashed lines) was not uniform in size. This non-uniformity can be attributed to two causes: (i) surface preparation of the two substrate materials with silicon carbide sand paper and, (ii) the dendritic structure of the cast IN-738 and X-40 substrates leading to non-uniform melting of the substrate due to compositional differences following diffusion of the melting point depressant, boron.

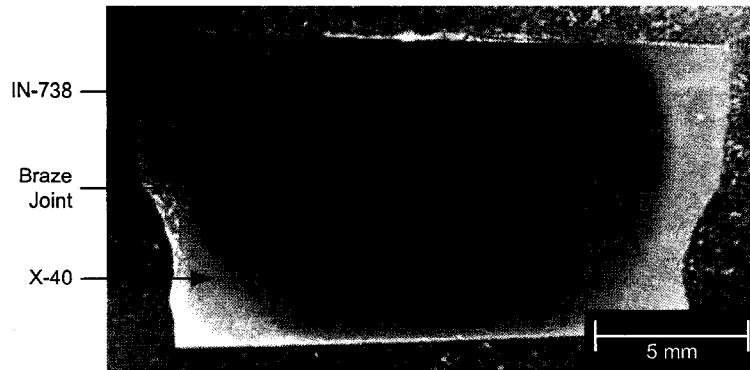


Figure 5-2 - Narrow Gap Braze Joint for Microstructural Examination

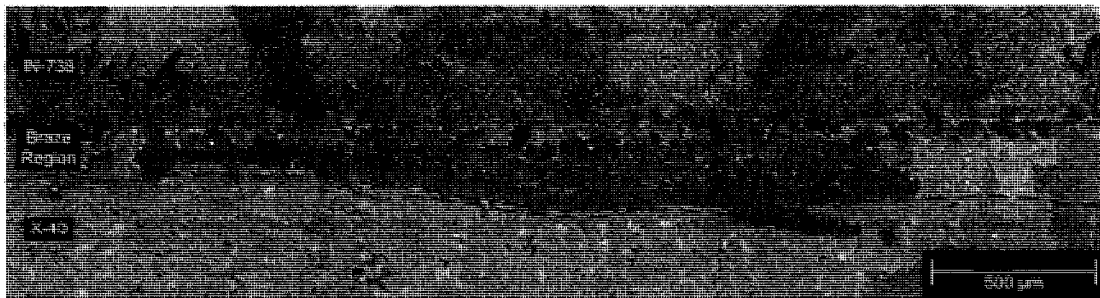


Figure 5-3 - Narrow Gap Braze Joint Showing Irregular Braze Region Between Two Substrate Materials

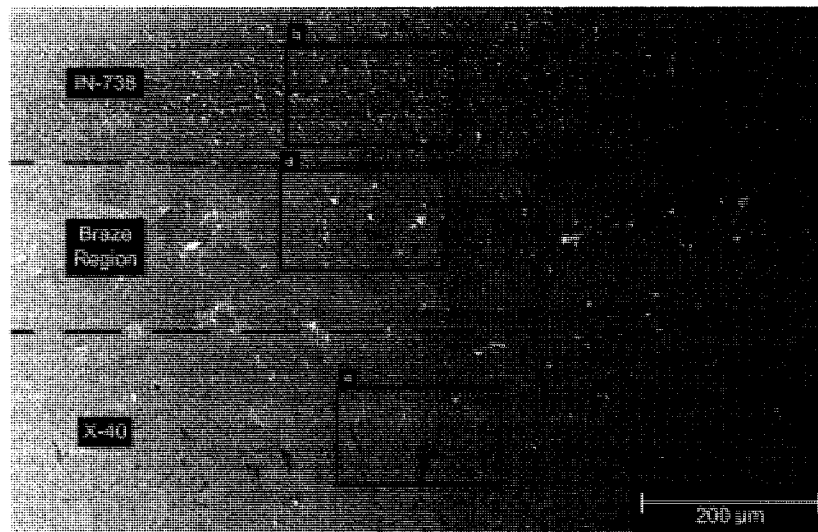
The microstructure in the braze region and the adjacent substrates were analyzed using element mapping and energy dispersive spectrometry (EDS) analysis. The regions of interest, identified in Figure 5-4a, include the interface between the IN-738 substrate and the braze joint, the braze region, and the interface between the X-40 substrate and the braze joint.

The interface region between IN-738 and the braze joint contained large amount of discrete particles. The morphologies of these particles varied significantly, however their compositions were quite similar, containing significant amounts of Ti, Ta, W and Nb and limited Ni and Cr, as shown in Figure 5-4b. As these elements are known carbide formers and the carbon peak in the EDS spectrum is distinct, shown in Figure 5-4c, these discrete particles can be assumed to be refractory-rich carbides. Since the EDS equipment used in this study lacked the sensitivity to distinguish between C and B, and because B can diffuse into the interface region during brazing, these phases may contain boron and thus it can be assumed that these discrete particles are carboborides.

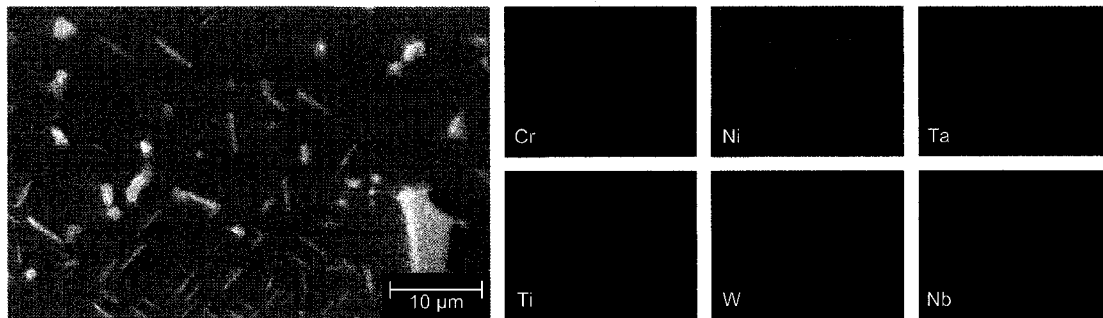
The microstructure in the braze region exhibited different features compared to that in the IN-738 interface region. As shown in Figure 5-4d, the braze region contained small grains, approximately 50  $\mu\text{m}$  in diameter, surrounded by a eutectic structures and bright discrete particles. Based on the Ni element map, the grains were determined to be the primary  $\gamma$ -Ni solid solution formed during solidification of the braze joint. From the element maps of the braze region, shown in Figure 5-4d, it can be seen that the eutectic constituents were enriched in Cr and W while the discrete phase contained primarily Ti, W, Ta and Nb. The eutectic constituents are believed be either binary Cr,W-boride-  $\gamma$ -Ni

or ternary Cr,W-boride - Ni-boride-  $\gamma$ -Ni (termed eutectic phases in the sections to follow) as the terminal eutectic product from Ni, Cr, W and B system, after [64]. The discrete particles were identified as either Ti/W/Ta/Nb-rich carbides or carboborides based on the EDS spectrum. As with boron diffusing from the braze alloy to the substrate, carbon from IN-738 and X-40 substrates can diffuse into the braze region during brazing forming carbides or carboborides. The exact nature of the discrete phases could not be determined with the EDS equipment used, and they will thus be described as discrete carbides in the following sections. It can be postulated that the solidification sequence during brazing began with the  $\gamma$ -Ni formation, which rejected Cr, W, B and C to the remainder of the molten braze. This solidification was followed by subsequent binary or ternary eutectic reaction, forming eutectic phase surrounding the primary  $\gamma$ -Ni phase. Solid state precipitation of carbides or carboborides took place along and within the primary  $\gamma$ -Ni during cooling.

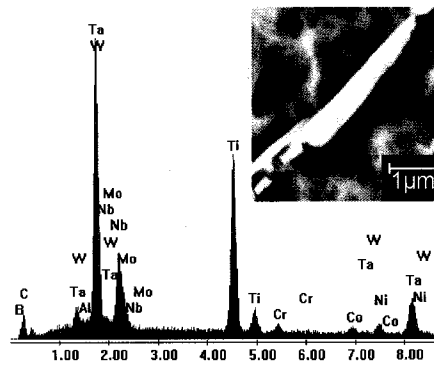
The microstructure of the interface between the X-40 substrate and the braze region, shown in Figure 5-4e, consists of a Co matrix with Cr-rich carbides and carboborides at the grain boundaries.



a



b



c

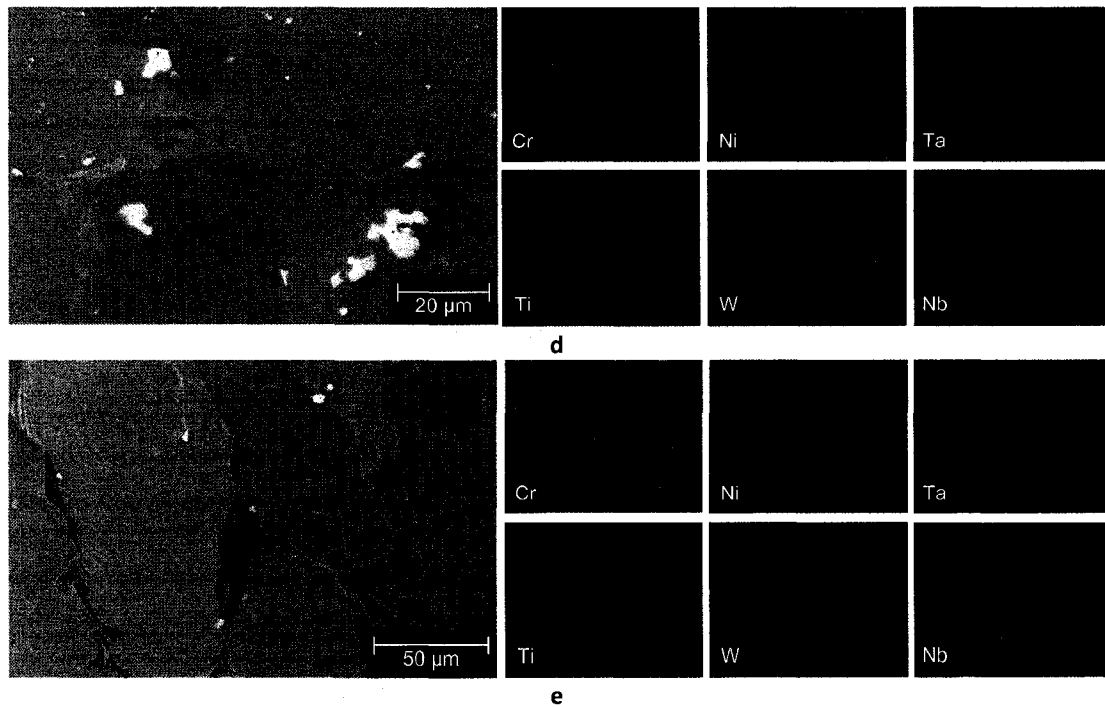


Figure 5-4 - (a) Narrow Gap Braze Joint, (b) Microstructure and Element Maps of the IN-738/Braze Interface, (c) EDS Spectrum of the Acicular Particle in the IN-738/Braze Interface, (d) Microstructure and Element Maps of the Braze Region, (e) Microstructure and Element Maps of the X-40/Braze Interface

### 5.2.2 Isothermally Exposed Condition

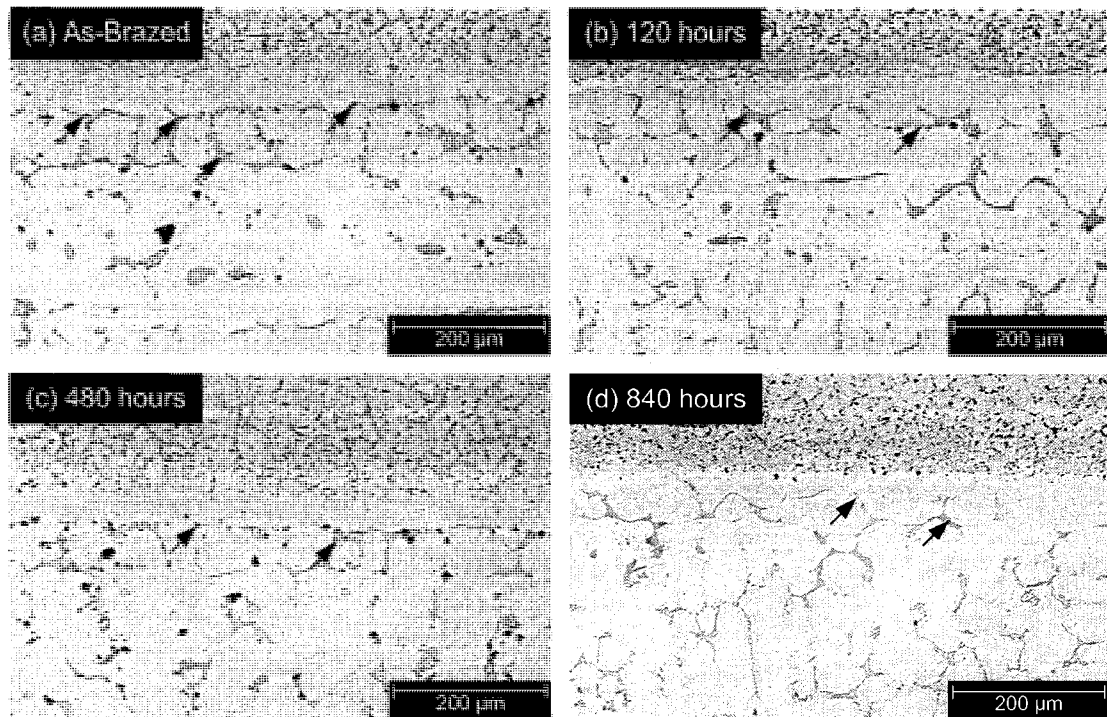
The narrow gap braze specimens were isothermally heat treated at 950°C for 120, 480 and 840 hours to study the changes in microstructure and mechanical properties. In general, the braze region became more uniform after heat treatment. It is notable that the discrete carbides and eutectic phases surrounding the primary  $\gamma$ -Ni phase were minimized as a result of heat treatment as shown in Figure 5-5. In general, the quantity and the size of these carbide and eutectic phases reduced with increased heat treatment time from 120 to 840 hours.

The microstructure of the brazed joint after 840-hour isothermal heat treatment is shown in Figure 5-6. Compared to that in the as-brazed condition, shown in Figure 5-4b, the size of the discrete globular particles in the IN-738/braze region interface increased with isothermal exposure, as shown in Figure 5-6b. The particles in the interface

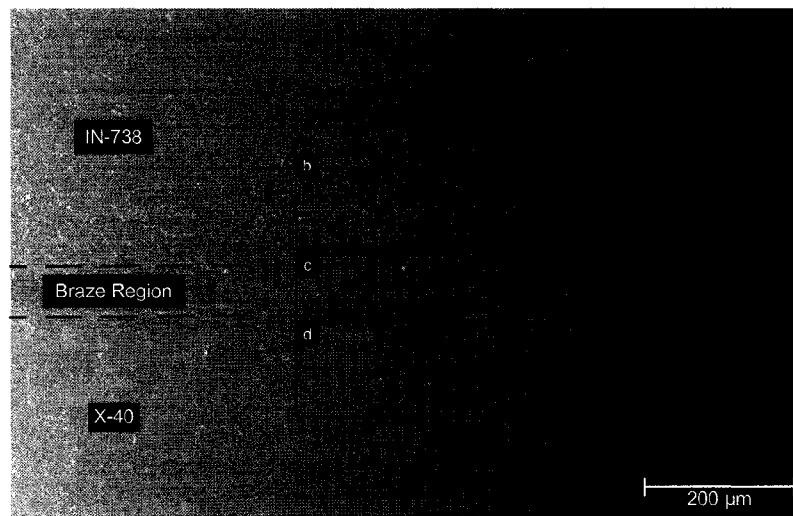
continued to be composed mainly of Ti, W, Ta and Nb. Cr was found to segregate to the outer layer of the particles compared to the as-brazed condition, evident by comparing Figure 5-4b and Figure 5-6b Cr maps. The amount of needle like acicular phase was also found to decrease considerably after heat treatment.

Comparing the microstructures of the braze regions in the as-braze and heat treated conditions, shown in Figure 5-4d and Figure 5-6c respectively, it can be seen that both the quantity and the size of eutectic phases and discrete carbides reduced substantially with heat treatment. The compositions of these eutectic and carbide phases did not change with heat treatment.

The microstructure in the interface between X-40 and braze region was also modified as a result of isothermal exposure. The microstructure became more uniform, as evident when comparing Figure 5-4e to Figure 5-6d. The quantity of the chromium carbide phase also reduced with heat treatment.



**Figure 5-5 - Microstructure of the Narrow Gap Braze Joint in the (a) As-Brazed Condition, and After Isothermal Heat Treatment at 950°C for (b) 120 hours, (c) 480 hours, (d) 840 hours – Red Arrows Indicate Carbides, Blue Arrows Indicate Eutectic Phases Surrounding the Primary  $\gamma$ -Ni in the Braze Region**



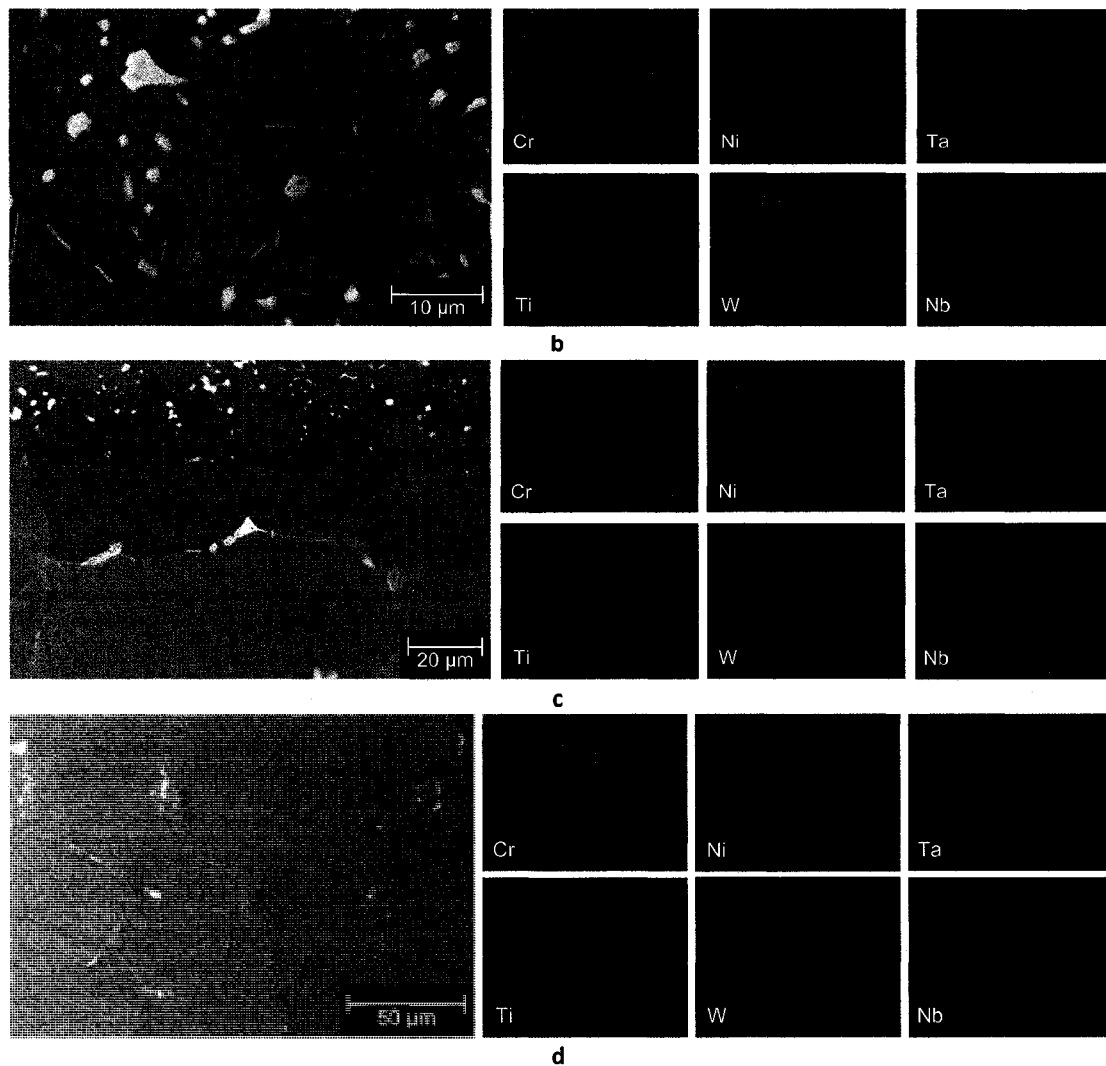


Figure 5-6 - (a) Narrow Gap Braze Region Between IN-738 and X-40 after 840-hour Heat Treatment at 950°C, (b) Microstructure and Element Maps for the IN-738/Braze Region Interface, (c) Microstructure and Element Maps for the Braze Region, (d) Microstructure and Element Maps for the X-40/braze interface

### 5.2.3 Microhardness Measurement

The hardness of the various phases found in the as-brazed narrow gap braze joint were assessed using nanoindentation. The average Vickers hardness observed from several indentations are summarized in Table 5-2. It can be seen that the hardness of both the eutectic and discrete carbide phases were significantly higher than the IN-738 substrate or the primary  $\gamma$ -Ni, as was found in other studies [65],[66]. The hardness observed for

the IN-738 substrate, the eutectics, and the primary  $\gamma$ -Ni are consistent with the results of other studies, however the hardness of the discrete Cr,W-rich carbides was found to be higher than was found in previous studies for Cr-borides commonly observed in brazing of IN-738.

**Table 5-2 - Microhardness of Various Phases in the Braze Region**

Phase	Load (mN)	Average Vickers Hardness	Reported Vickers Hardness [65],[66]
IN-738 Substrate	40	432	366-453
Primary $\gamma$ -Ni	40	419	321-378
Eutectic Phases	150	720	722-982 (Eutectic Ni boride – Cr boride – $\gamma$ -Ni)
Discrete carbide/carboboride	40	3542	1958-2210 (Cr boride)

#### 5.2.4 Tensile Properties

High temperature tensile tests at 950°C were carried out on the narrow gap braze specimens in the as-brazed condition and after isothermal heat treatment. The yield strength, ultimate tensile strength and ductility observed from these tests are summarized in Table 5-3 and graphically in Figure 5-7. The tensile properties of X-40 bars were also examined for baseline comparison. The yield strength of the braze joints was found to be greater than that of the X-40 substrate, irrespective of the heat treatment condition, suggesting that the braze joints have increased resistance to plastic deformation. The increased yield strength observed in the braze joints was likely due to the presence of the hard carbide and eutectic phases that were observed surrounding the primary  $\gamma$ -Ni in the braze joint. Similarly the ultimate tensile strength of the braze joint test coupons exceeded that of the X-40 coupons, except in the case of the as-brazed condition.

The ductility of the braze samples varied significantly with isothermal exposure. The extensometer used in this research saturated at 10% elongation, as such beyond this level the exact elongation cannot be accurately reported and will be noted as >10%. As expected, the baseline X-40 specimens had a strain at failure of far greater than 10% (as suggested by the linear variable differential transformer (LVDT) data from the MTS test machine). The as-brazed narrow gap braze specimens were far less ductile, having an average strain at failure of 2.54%. Isothermal heat treatment at 950°C resulted in a substantial increase in ductility from the as-brazed condition. As noted in Table 5-3, the observed ductility of the braze joint increased to 9.43% strain at failure with 120 hours of isothermal exposure at 950°C, however prolonging this heat treatment to 480 and subsequently 840 hours resulted in a progressive reduction in ductility. Reduction in area of the NGB coupons cannot be accurately reported due to the narrow width of the braze region. The cause of these changes in ductility will be discussed in the sections to follow.

Table 5-3 - Summary of High Temperature Tensile Test Results at 950°C

Condition	Sample	Yield Strength (MPa)	Ultimate Tensile Strength (MPa)	% Elongation
X-40	1	170	328	>10
	2	173	344	>10
	<b>Average</b>	<b>172</b>	<b>336</b>	<b>&gt;10</b>
As-Brazed	1	195	296	2.26
	2	201	330	2.81
	<b>Average</b>	<b>198</b>	<b>313</b>	<b>2.54</b>
120 hr	1	201	352	9.41
	2	195	355	9.45
	<b>Average</b>	<b>198</b>	<b>354</b>	<b>9.43</b>
480 hr	1	191	349	7.55
	2	197	345	7.56
	<b>Average</b>	<b>194</b>	<b>347</b>	<b>7.56</b>
840 hr	1	201	348	5.34
	2	200	344	7.08
	<b>Average</b>	<b>201</b>	<b>346</b>	<b>6.21</b>

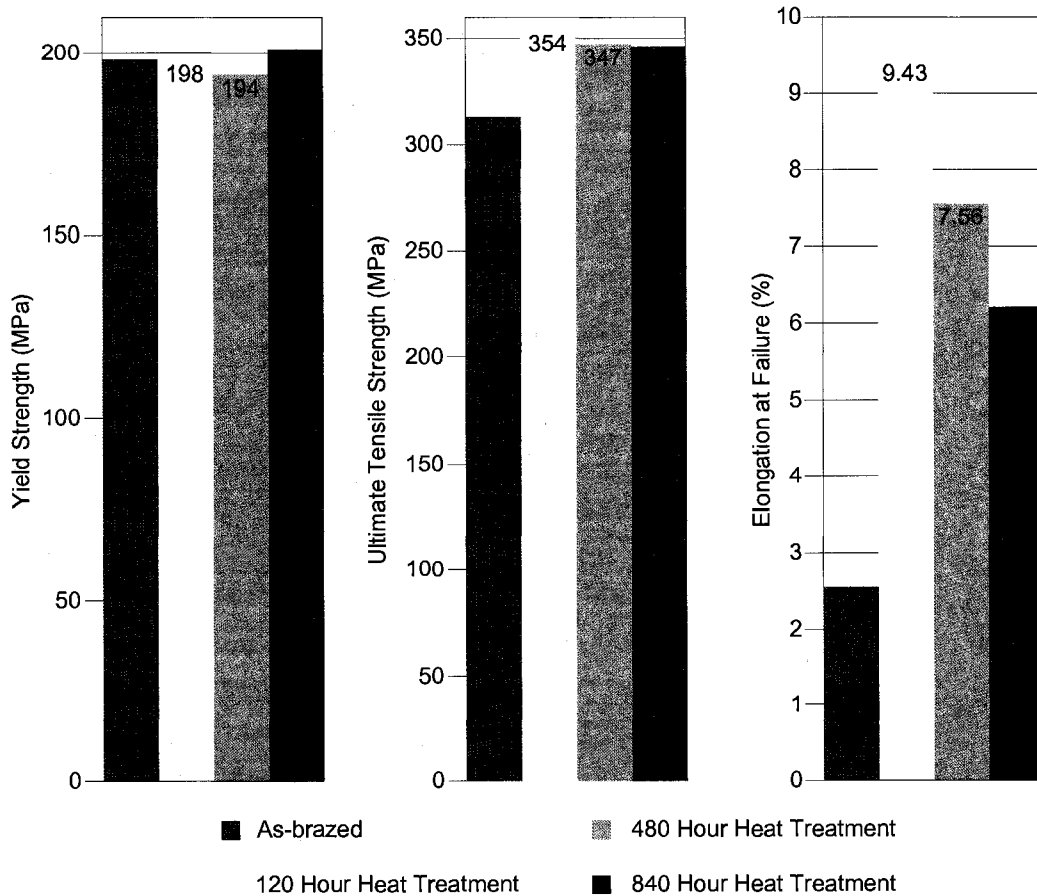


Figure 5-7 - NGB Tensile Properties

### 5.2.5 Examination of the Tensile Fracture Surfaces

Following tensile tests, the fracture surfaces of the narrow gap braze coupons were examined under SEM. Sample fracture surfaces of the X-40 side of the as-brazed and from each heat treatment condition are shown in Figure 5-8. Failure occurred within the braze region in all narrow gap braze specimens, regardless of heat treatment condition. Low magnification examination, at 100x, of the fracture surfaces revealed a trend from a relatively smooth fracture surface in the as-brazed condition with increasing roughness as isothermal heat treatment time is increased, as shown in Figure 5-8.

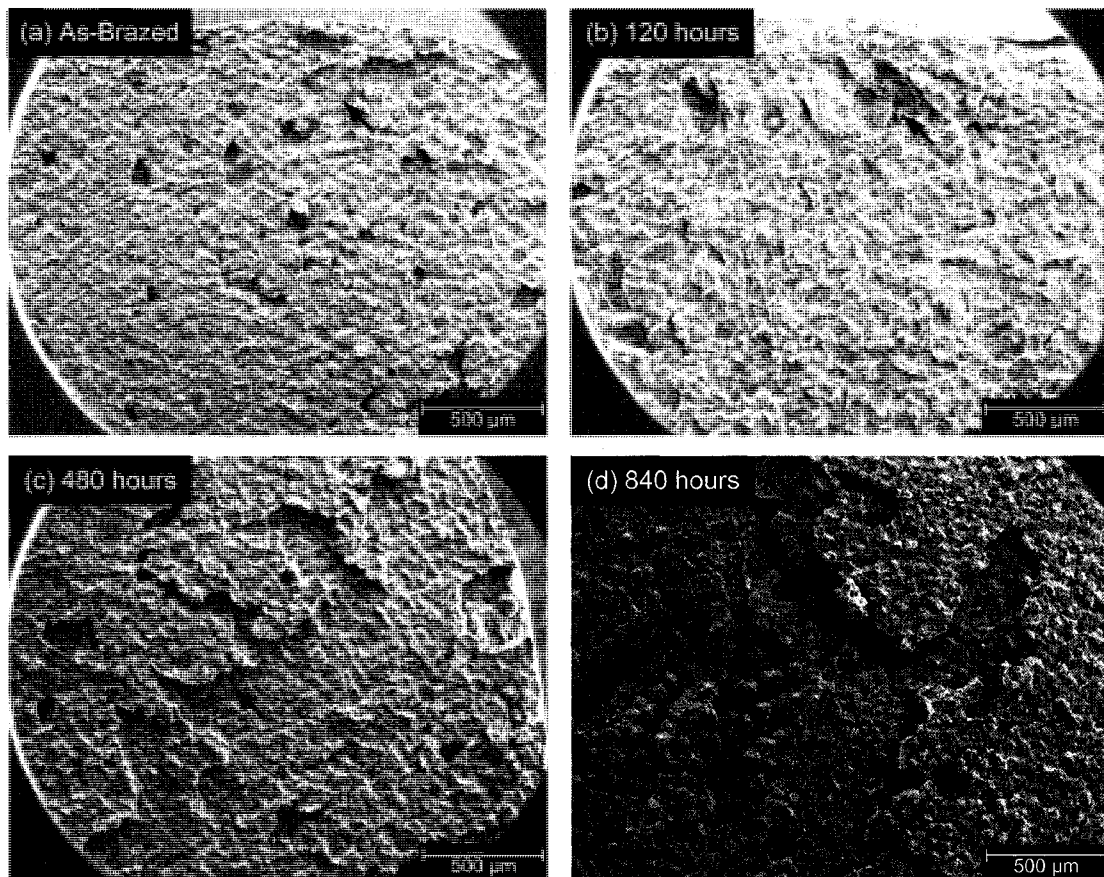
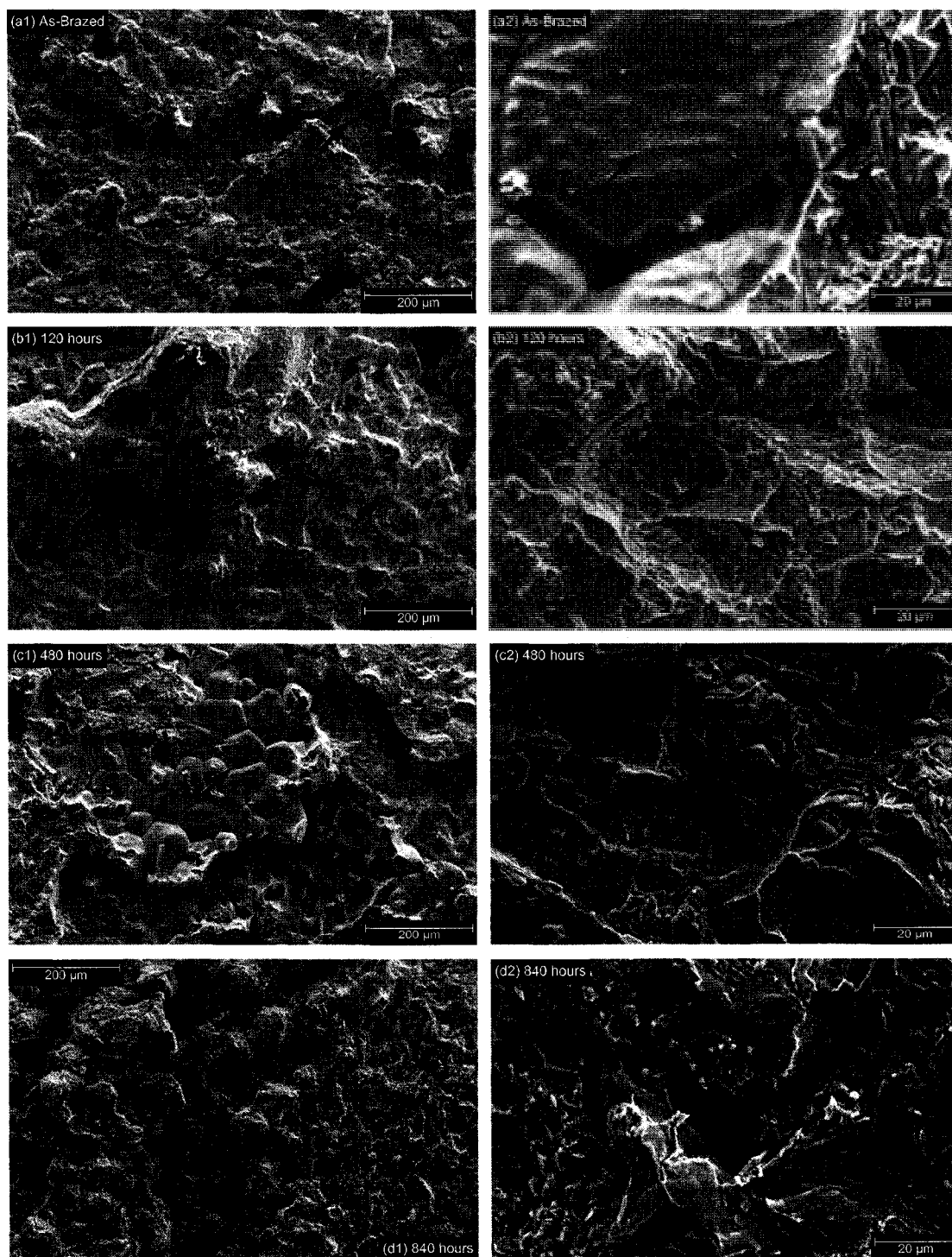


Figure 5-8 - Fracture Surfaces of Braze Specimens in the As-Brazed and Heat Treated Conditions, (a) As-Brazed, (b) 120 hours, (c) 480 hours, (d) 840 hours – Arrows Indicate Intergranular Failure Locations

Examination of the narrow gap braze tensile fracture surface at higher magnifications revealed two fracture modes, (i) intergranular (IG) fracture, occurring through the eutectic and not through the  $\gamma$ -Ni and, (ii) transgranular (TG) fracture, progressing through the  $\gamma$ -Ni phase. The intergranular phases (eutectics and discrete carbides) possess high hardness and therefore are quite brittle, rendering them susceptible to crack initiation during tensile testing.

Both IG and TG failure modes were observed in all narrow gap braze specimens, regardless of heat treatment condition, as identified for each condition in Figure 5-9. The exposed eutectic shown in Figure 5-9 a-2 suggests that the fracture path followed the interface between the  $\gamma$ -Ni and the eutectic phases. It was observed that heat treatment of the narrow gap braze specimens reduced the amount of IG failure mode observed on the fracture surface because of the reduction in size and quantity of the eutectic and carbide phases. This reduction may also account for the increased ductility in the heat treated specimens. However, unlike ductility, the proportion of fracture surface covered by IG or TG failure mode does not vary significantly when the heat treatment time is increased from 120 to 840 hours, as shown in Figure 5-9 b-1 through d-2.



**Figure 5-9 - Isothermal Tensile Test Fracture Surfaces of Narrow Gap Braze Specimens in the As-Brazed and Heat Treated Conditions, (a) As-Brazed Specimen Showing Mixed Mode IG and TG Fracture Modes, (b) 120 hour Heat Treated Sample Showing Predominantly TG Fracture Mode, (c) 480 hour Heat Treated Sample Showing Mixed TG and IG Fracture Modes, (d) 840 hour Heat Treated Sample Showing Mixed TG and IG Fracture Modes, Red Arrows Indicated IG Mode, Blue Arrows Indicated TG Mode**

### 5.2.6 Examination of the Tensile Fracture Surface Cross Sections

Following SEM analysis of the fracture surfaces, the IN-738 side of the narrow gap braze specimens were sectioned and prepared for further examination. Cracks were found to initiate in either the discrete carbide phases or the eutectic phases surrounding the primary  $\gamma$ -Ni phase, as shown in Figure 5-10.

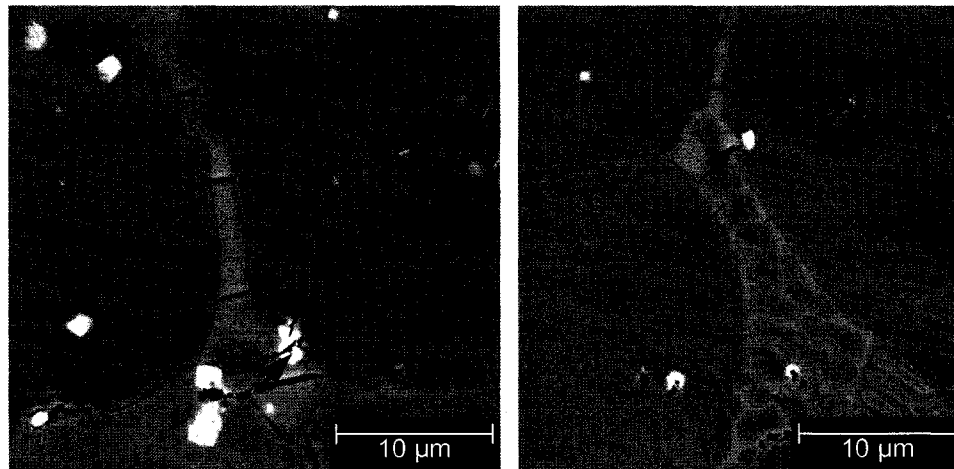


Figure 5-10 - Crack Initiation Within the Discrete Carbides (Blue Arrows) and Eutectic Phases Surrounding the Primary  $\gamma$ -Ni Phase (Red Arrows)

Further examination of the cross section of the as-brazed specimen suggested that the fracture occurred in the carbides and eutectics surrounding the primary  $\gamma$ -Ni. An example of the IG failure mode in the as-brazed condition is shown in Figure 5-11. The predominantly IG failure mode in the as-brazed specimens was likely the cause of the limited ductility observed during tensile testing.

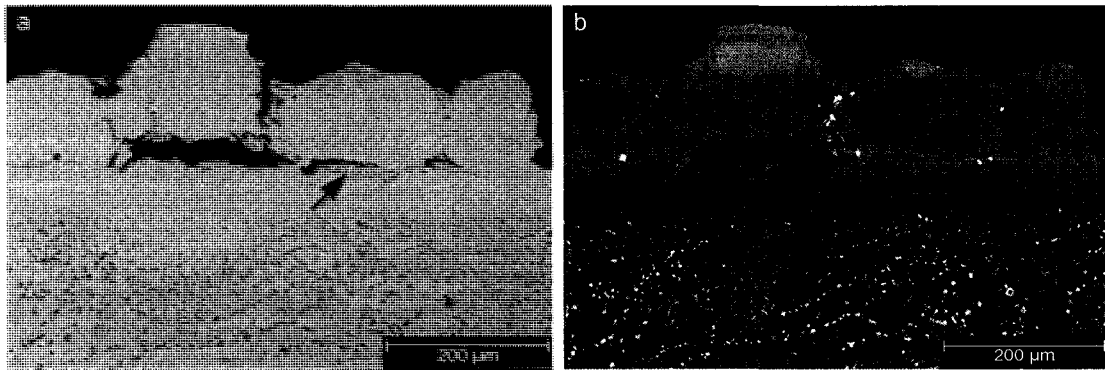


Figure 5-11 - IG Fracture in the As-Brazed Condition, (a) Optical, (b) SEM, Red Arrows Identify Eutectic Phases, Blue Arrows Identify Discrete Carbide Phases

Examination of the cross sections of the tensile fracture surfaces of the heat treated narrow gap braze specimens revealed similar cracking characteristics as the as-brazed specimens. The crack propagation in the heat treated specimens however consists of significantly more TG failure mode than the as-brazed specimens, as shown in Figure 5-12.

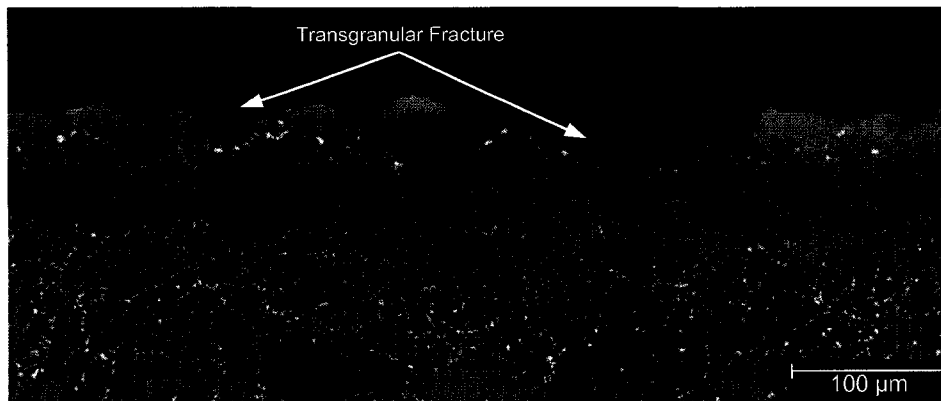
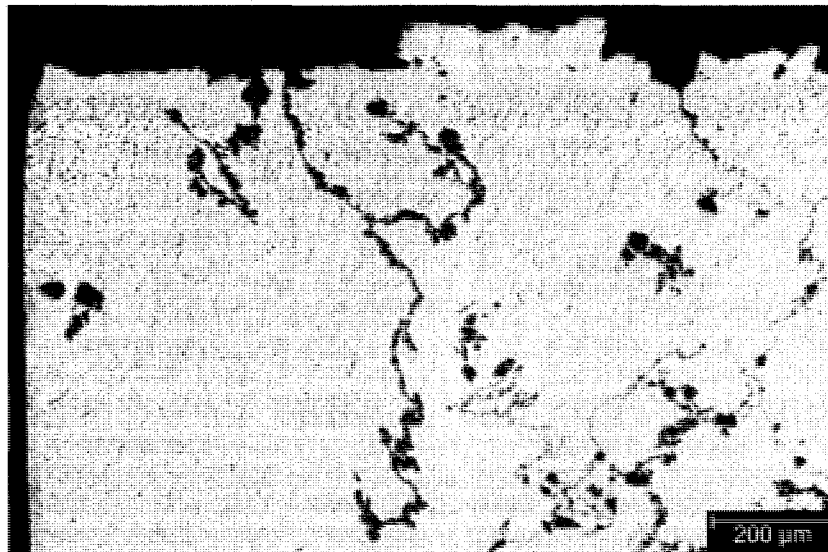


Figure 5-12 - Cross Section of the Tensile Fracture Surface of Specimen Heat Treated for 840 hours at 950°C

### 5.2.7 Oxidation During Isothermal Exposure

Isothermal exposure was found to be beneficial after narrow gap diffusion brazing as it generally reduced the amount and size of brittle phases, it is therefore reasonable to expect ductility to increase with heat treatment time. The ductility however was

observed to decrease from 9.43% in the 120 hour heat treated specimens to 6.21% in the 840 hour heat treated specimens, as shown in Table 5-3 and Figure 5-7. Examination of the cross section of the 840 hour heat treated tensile specimen near the circumference of the specimen suggests that this reduction in ductility is due to oxidation. The formation of brittle oxides in the braze region and in the IN-738 substrate, shown in Figure 5-13, and the inclusion of oxygen in the matrix likely contributed to the observed reduction in ductility with increased exposure to high temperature.



**Figure 5-13 - Cross Section of Tensile Fracture Surface of 840 hour Isothermally Exposed Narrow Gap Braze Specimen Illustrating Oxide Formation**

### **5.2.8 Summary of NGB Microstructure and Tensile Results**

The microstructure of the NGB joint between IN-738 and X-40 consisted of a primary  $\gamma$ -Ni phase surrounded by secondary discrete carbides/carborides and eutectic phases. The hardness of both the carbides and the eutectic was higher than that of the IN-738 substrate and the primary  $\gamma$ -Ni. As such, during tensile testing cracks were found to initiate in the secondary phases. Crack propagation, however was found to occur in

both the intergranular and transgranular modes. The yield strength of the as-brazed joints was greater than that of X-40, however the ductility of the joint was significantly lower. Post braze heat treatment at 950°C for 120 hours increased both the yield strength and the ductility due to a reduction in the size and quantity of the secondary phases. Increasing the heat treatment to 480 and 840 hours resulted in a loss of ductility and tensile strength due to oxidation.

### 5.3 Wide Gap Diffusion Brazing

#### 5.3.1 Microstructural Characteristics

For the purpose of microstructural evaluation, two regions of interest for the wide gap brazing joints, identified in Figure 5-14, were the midbrazed region and the interface region between the X-40 substrate and the braze region.

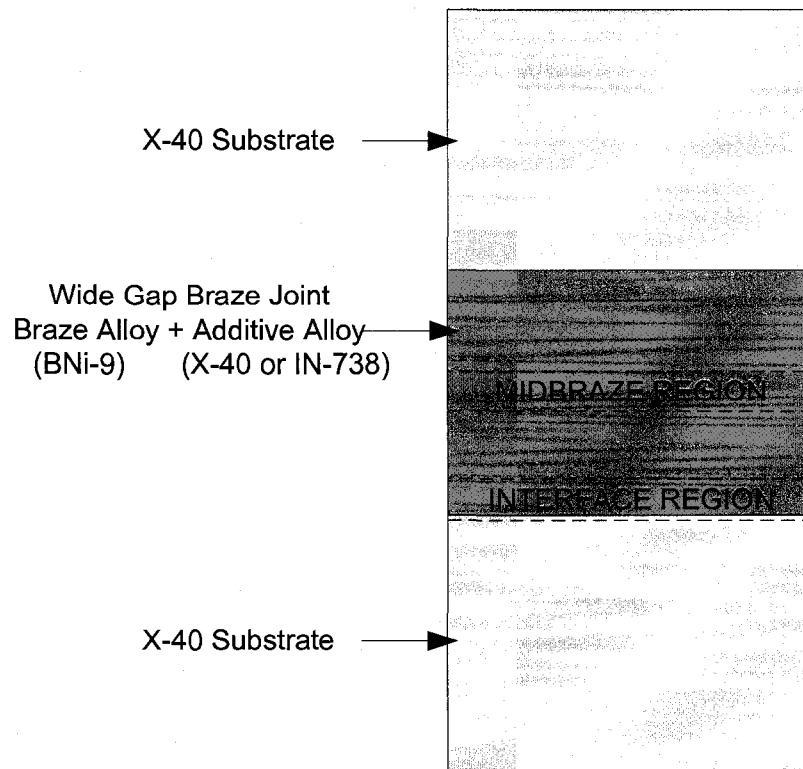


Figure 5-14 - Regions of Interest in Wide Gap Braze Specimens

### **5.3.1.1 Wide Gap Braze With X-40 Additive Alloy**

#### ***Porosity***

As shown in Figure 5-15, the porosity of the slurry filled wide gap braze joint with X-40 additive alloy was rather high. The porosity was determined by collecting and analyzing an array of SEM micrographs taken at 400x magnification. The porosity near the interface was determined to be approximately 0.11% volume fraction and the porosity midbraze was determined to be 2.9% volume fraction.

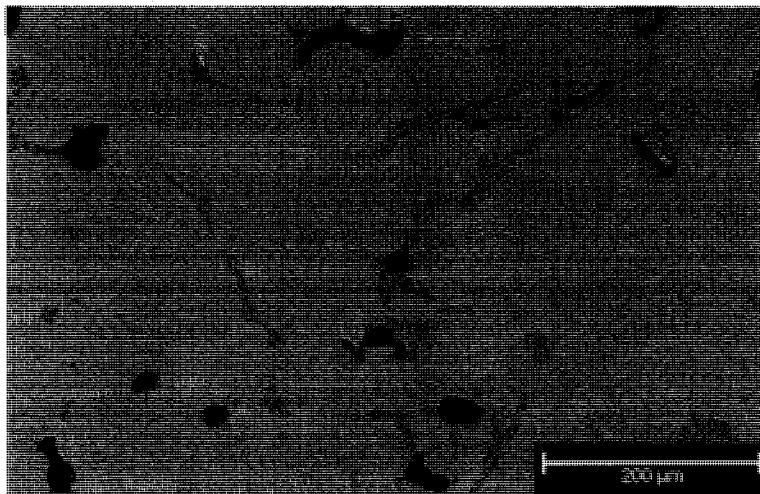


Figure 5-15 – Example of Porosity at the Midbraze of a WGB Joint with X-40 Additive

#### ***Midbraze Microstructure***

The microstructure at the midbraze of the wide gap braze with X-40 additive contained a primary cobalt-nickel (Co-Ni) matrix and ternary eutectic phases, as shown in Figure 5-16. No discrete carbides or borides were observed at the midbraze location. The average EDS results of the ternary eutectic phases, termed the eutectic matrix, tungsten rich chromium boride and chromium boride are shown in Table 5-4. All eutectic constituents contained significant boron and/or carbon, though as mentioned previously the EDS equipment used could not accurately distinguish between these two

elements. It can be seen from the element maps shown in Figure 5-17 that tungsten tends to draw into the eutectic phases while, as expected, nickel and cobalt levels were higher within the primary (Co-Ni) matrix.

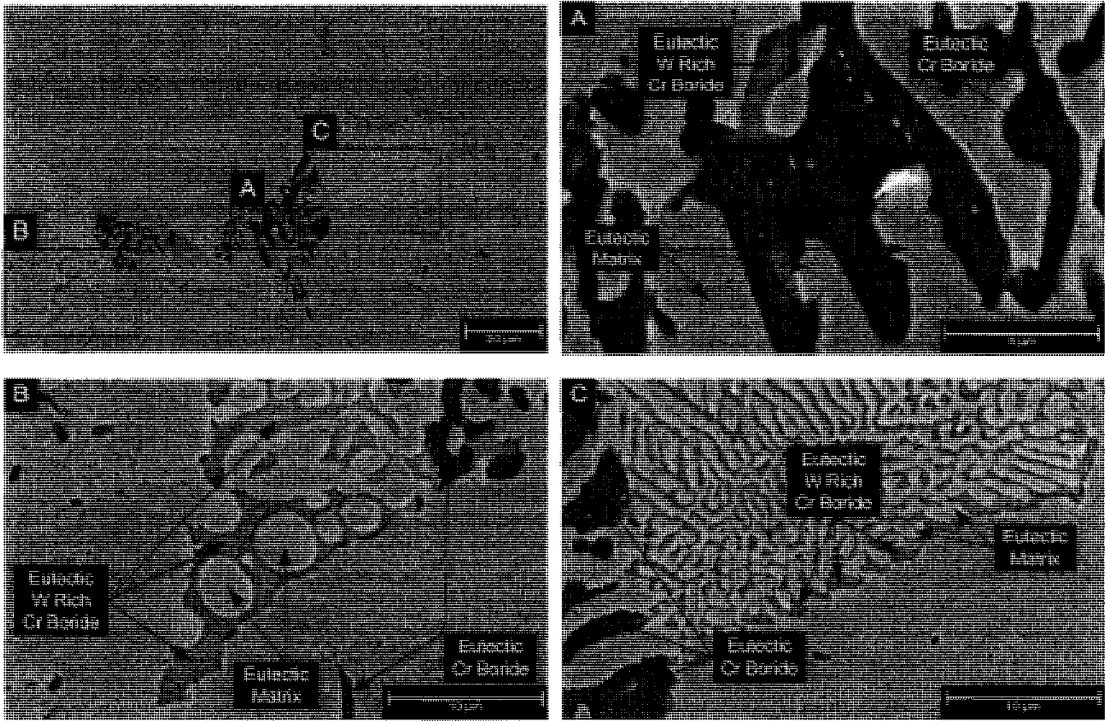
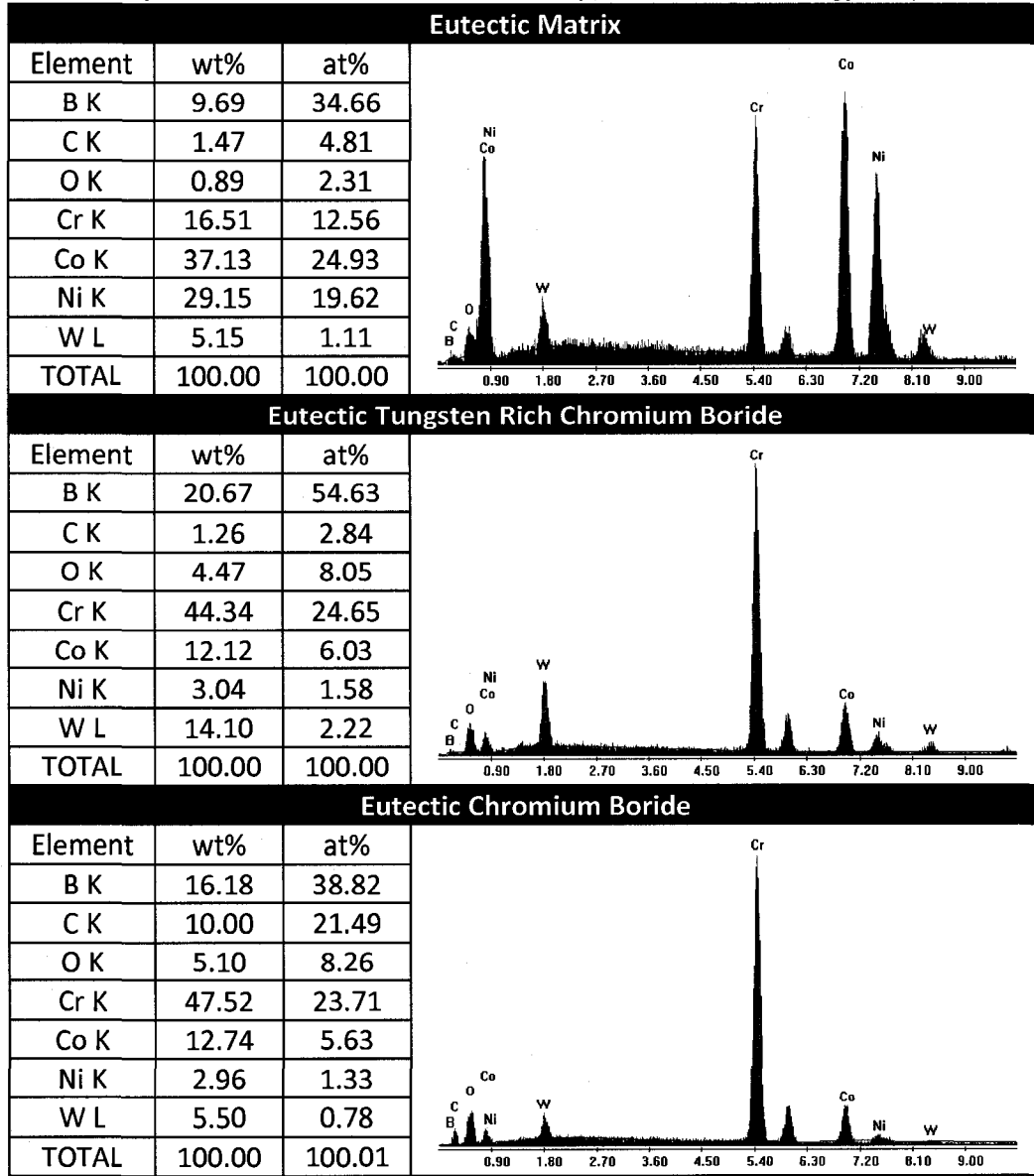


Figure 5-16 - Prominent Phases Found at Midbraze of WGB Specimen with X-40 Additive

Table 5-4 - Averaged EDS Results and Representative EDS Spectrum of WGB with X-40 Additive Specimen Midbraze Eutectic Constituents (L, K and M Denote Energy level)



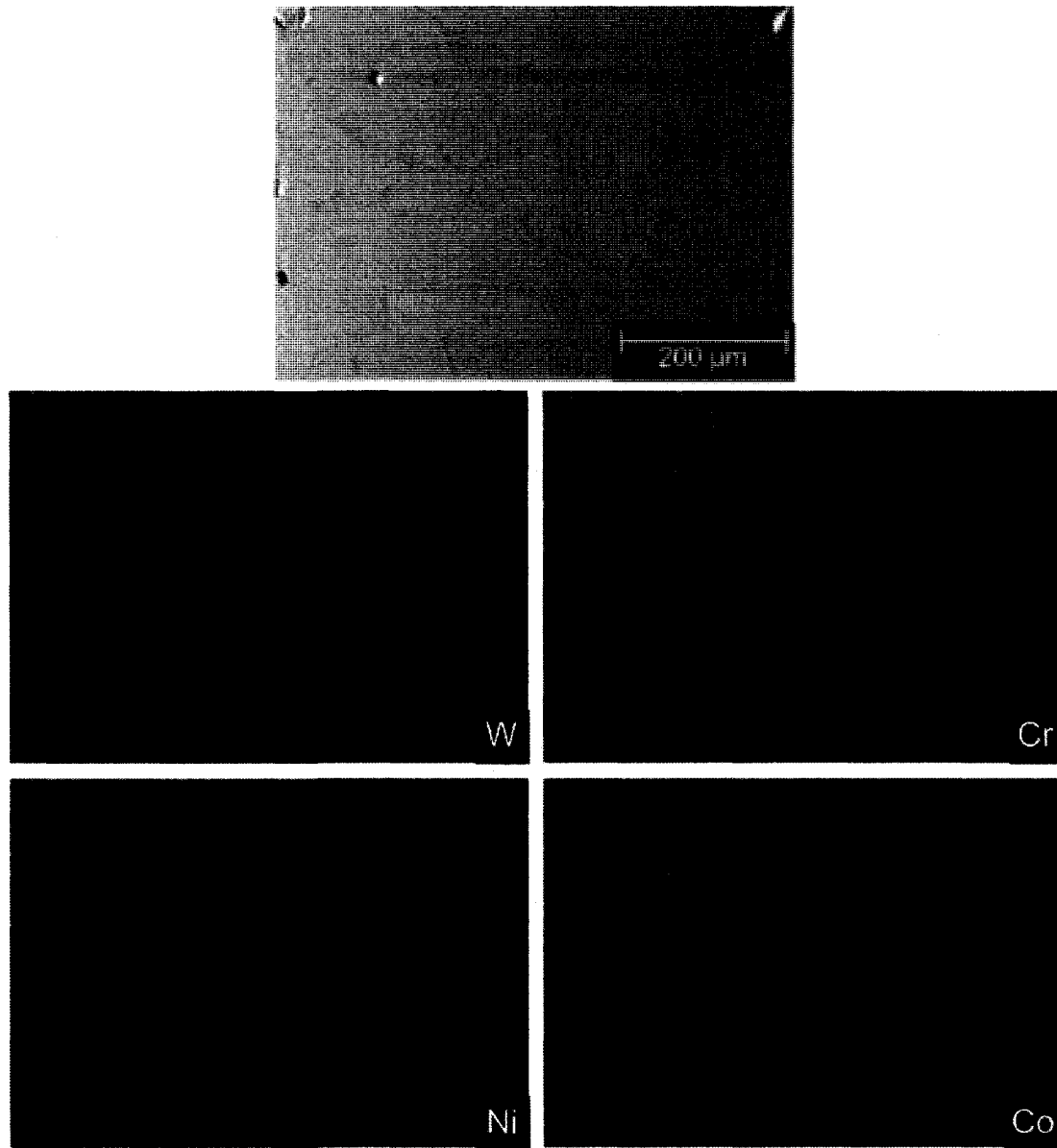


Figure 5-17 - Midbraze Element Maps of WGB Specimen with X-40 Additive Alloy

### ***Interface Microstructure***

The microstructure at the interface region of the WGB joint with X-40 additive consisted of the same ternary eutectic structures found at the midbraze location along with an additional white, tungsten rich cobalt boride phase, as shown in Figure 5-18. The average EDS results and a representative spectrum of this tungsten rich cobalt boride

phase are shown in Table 5-5. From the element maps for the interface shown in Figure 5-19, chromium appears more concentrated near the regions of the dark eutectic while tungsten appears more concentrated near the eutectic regions that contain the tungsten rich cobalt boride phase.

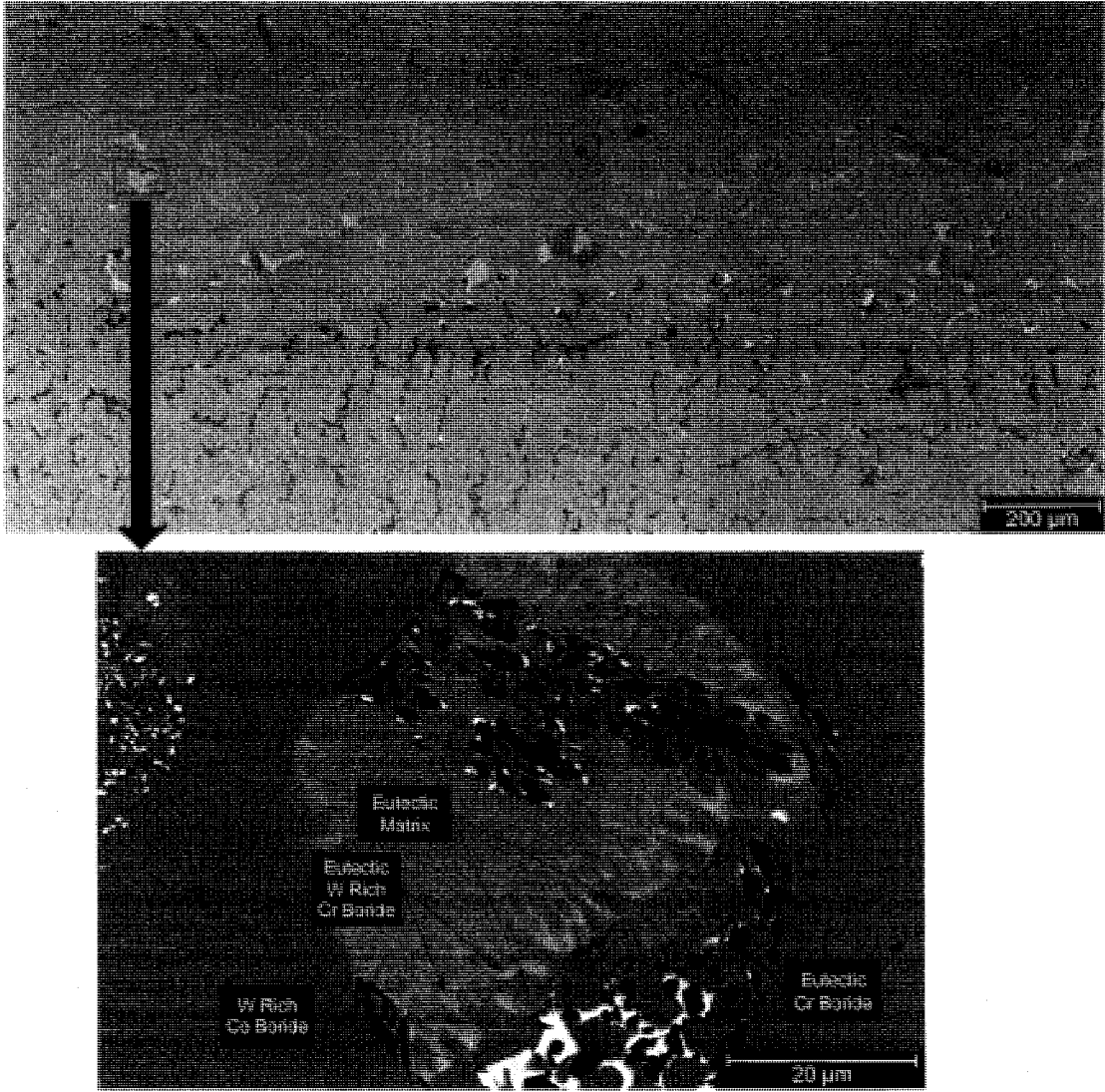


Figure 5-18 - Prominent Phases at Interface of WGB Specimen with X-40 Additive

Table 5-5 - Averaged EDS Results and Representative EDS Spectrum of Tungsten Boride Phase found at the X-40/Braze Interface in WGB with X-40 Additive Specimen (L, K and M Denote Energy level)

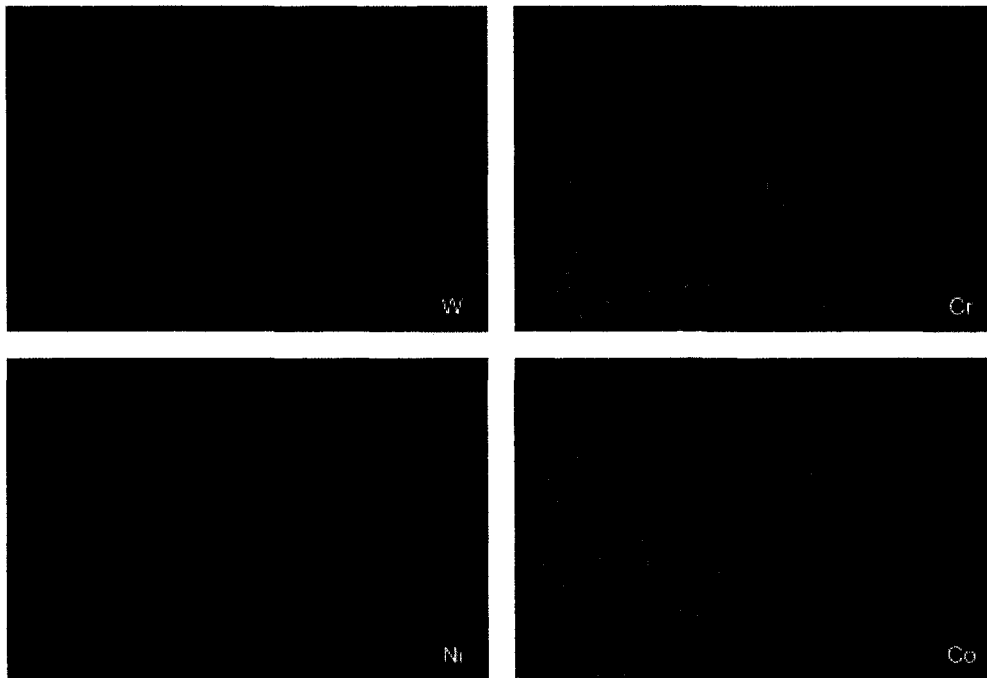
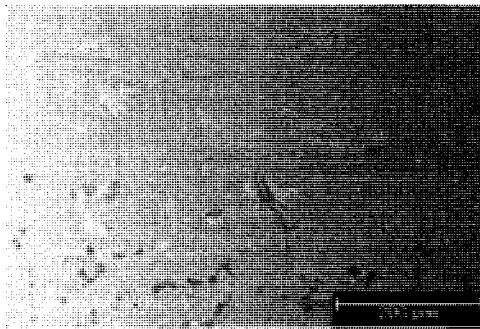
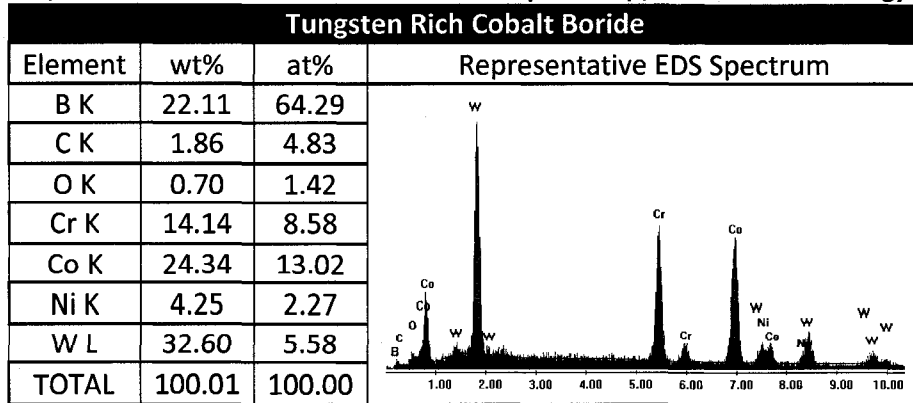


Figure 5-19 - Interface Element Maps of WGB Specimen with X-40 Additive

### ***Microhardness Measurement***

The hardness of the various phases found in the WGB joint with X-40 additive were assessed using nanoindentation. The average hardness of the phases observed on several indentations are shown in Table 5-6. It was found that the hardness of all phases observed in the braze were harder than the (Co-Ni) Matrix. The identity of the individual eutectics could not be determined when conducting nanoindentation testing and thus have been reported as eutectic 1 and eutectic 2.

**Table 5-6 - Average Nanoindentation Hardness of Phases Observed in WGB joint with X-40 Additive**

<b>Phase</b>	<b>Applied Load (mN)</b>	<b>Average Vickers Hardness</b>
(Co-Ni) Matrix	40	499
Eutectic 1	40	1007
Eutectic 2	40	1799
Fine Eutectic	150	665

#### ***5.3.1.2 Wide Gap Braze With IN-738 Additive Alloy***

##### ***Porosity***

As shown in Figure 5-20, the porosity of the tape filled wide gap braze joint with IN-738 additive alloy was very high. This porosity was not spread evenly throughout the braze but clustered in certain areas. Since the porosity in this case was highly localized, a specimen wide porosity volume fraction could not be determined and local porosity was determined instead. Several specimens were examined using the same process as previously described and the maximum local porosity area fraction on a single 400x micrograph was found to be approximately 20%. This highly localized porosity however did not cause the average volume fraction of porosity to be higher than that observed in the WGB with X-40 additive alloy configuration.

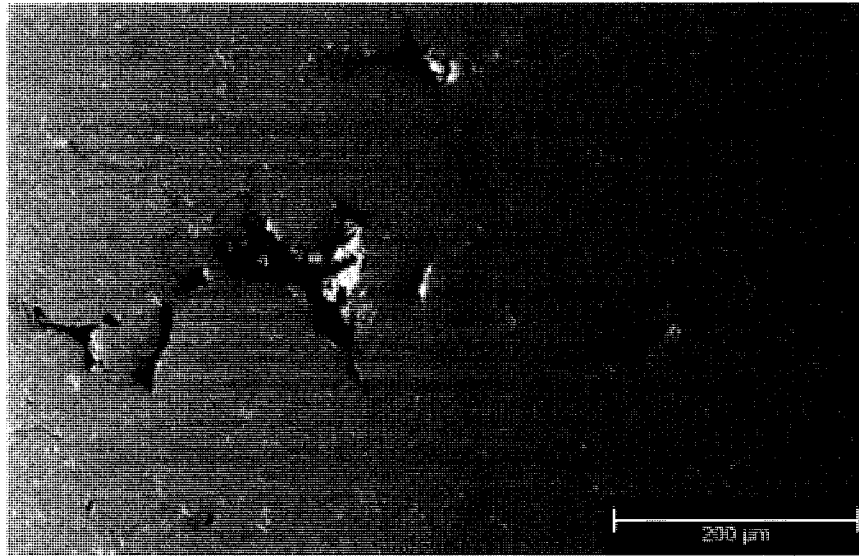


Figure 5-20 – Example of Porosity at the Midbrazed of WGB with IN-738 Additive Alloy

### ***Midbrazed Microstructure***

The microstructure of the WGB joint with IN-738 additive consisted of a primary  $\gamma$ -Ni matrix with a ternary eutectic structure and discrete borides, as shown in Figure 5-21. The ternary eutectic consisted of a light coloured nickel boride, a dark coloured chromium boride and primary  $\gamma$ -Ni. Two types of discrete boride phases were observed, a white, titanium and tantalum rich carboboride precipitate and a dark nickel and chromium boride precipitate. The averaged EDS results and representative spectrums of these phases are shown in Table 5-7. Element maps of the midbrazed region of the tape filled wide gap braze joint with IN-738 additive alloy are shown in Figure 5-22. The maps for tungsten and tantalum are combined as they were optically indistinguishable (tungsten map shown). As expected the level of nickel is higher in the primary  $\gamma$ -Ni phase and level of chromium, tungsten, titanium, niobium and molybdenum higher in the area surrounding the primary  $\gamma$ -Ni.

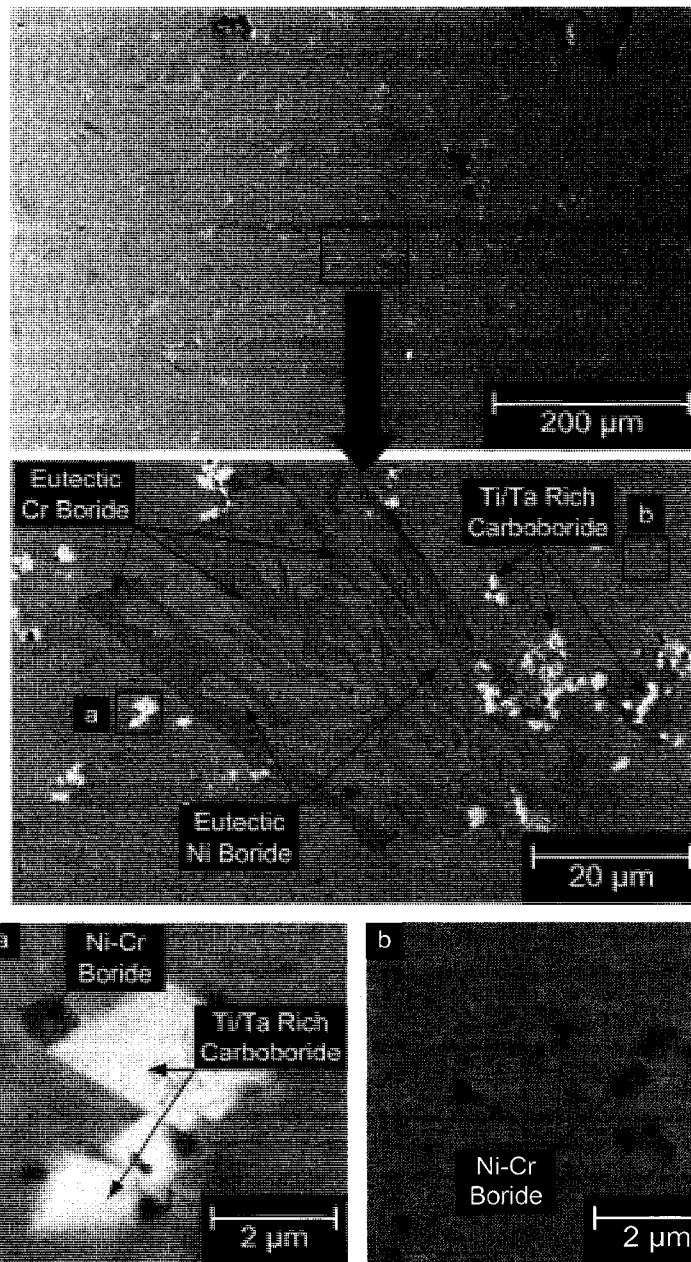
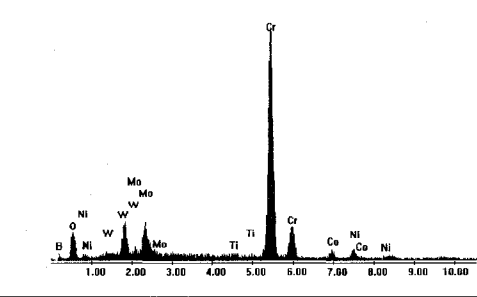


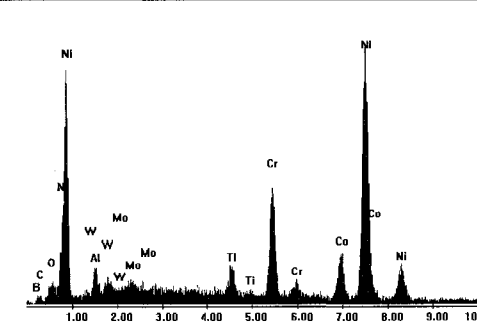
Figure 5-21 - Prominent Phases Found at Midbraze of WGB with IN-738 Additive

**Table 5-7 - Averaged EDS Results and Representative EDS Spectrum of WGB with IN-738 Additive Specimen Midbraze Eutectics and Discrete Phases (L, K and M Denote Energy level)**

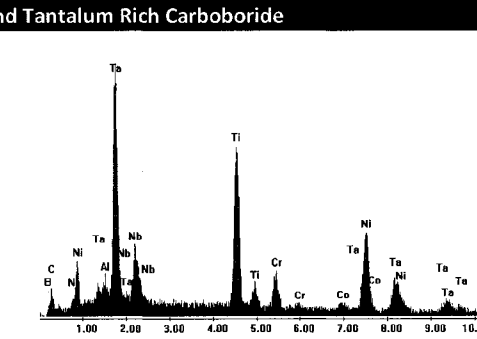
Eutectic Chromium Boride		
Element	wt%	at%
B K	20.10	54.46
O K	5.05	9.39
W M	10.93	1.77
Mo L	6.84	2.13
Ti K	0.50	0.31
Cr K	49.52	28.35
Co K	2.97	1.51
Ni K	4.09	2.08
TOTAL	100.01	100.00



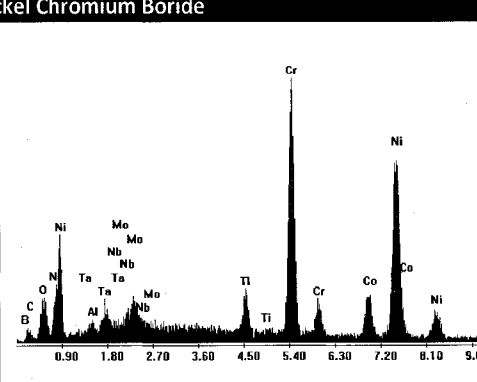
Eutectic Nickel Boride		
Element	wt%	at%
B K	13.93	44.46
C K	1.27	3.42
O K	0.09	0.23
AlK	2.16	2.81
W M	2.87	0.55
MoL	0.97	0.35
TiK	1.95	1.43
CrK	10.87	7.34
CoK	9.50	5.69
NiK	56.39	33.75
TOTAL	100.01	100.01



Titanium and Tantalum Rich Carboboride		
Element	wt%	at%
B K	17.92	46.75
C K	12.28	28.82
AlK	0.32	0.35
NbL	8.33	2.52
TiK	16.79	9.89
CrK	3.07	1.68
CoK	1.28	0.61
NiK	9.60	4.64
TaL	30.40	4.74
TOTAL	100.00	100.00



Nickel Chromium Boride		
Element	wt%	at%
B K	16.99	47.58
C K	1.75	4.27
O K	3.90	7.47
AlK	1.10	1.17
TaM	5.95	0.99
NbL	0.89	0.28
MoL	1.83	0.58
TiK	4.07	2.59
CrK	25.54	15.02
CoK	5.65	3.01
NiK	32.33	17.04
TOTAL	100.00	100.00



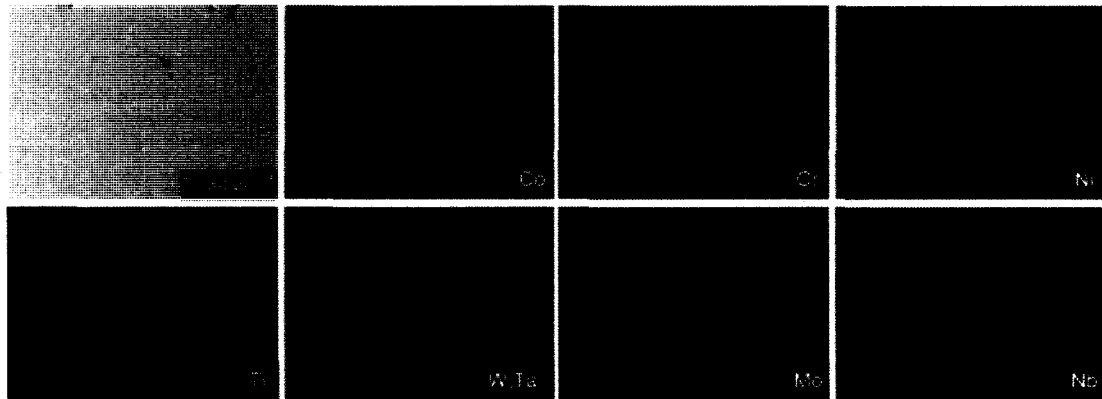


Figure 5-22 - Midbraze Element Maps of WGB with IN-78 Additive

### ***Interface Microstructure***

The phases observed at the interface of the WGB joint with IN-738 additive alloy were similar those observed at the midbraze location. The composition of these phases were found to vary only slightly from the midbraze though, as shown in Figure 5-23, they had different morphology. EDS results of the phases observed in the interface of the WGB joint with IN-738 additive were similar to those found for the midbraze location, shown in Table 5-7. Element maps at this location show a strong nickel and cobalt gradient moving from braze to the substrate, as shown in Figure 5-24. It can also be seen that titanium, tantalum, tungsten and niobium tend to amalgamate to a large extent in the region of the interface, suggesting diffusion through the braze alloy as X-40 does not contain tantalum, titanium or niobium.

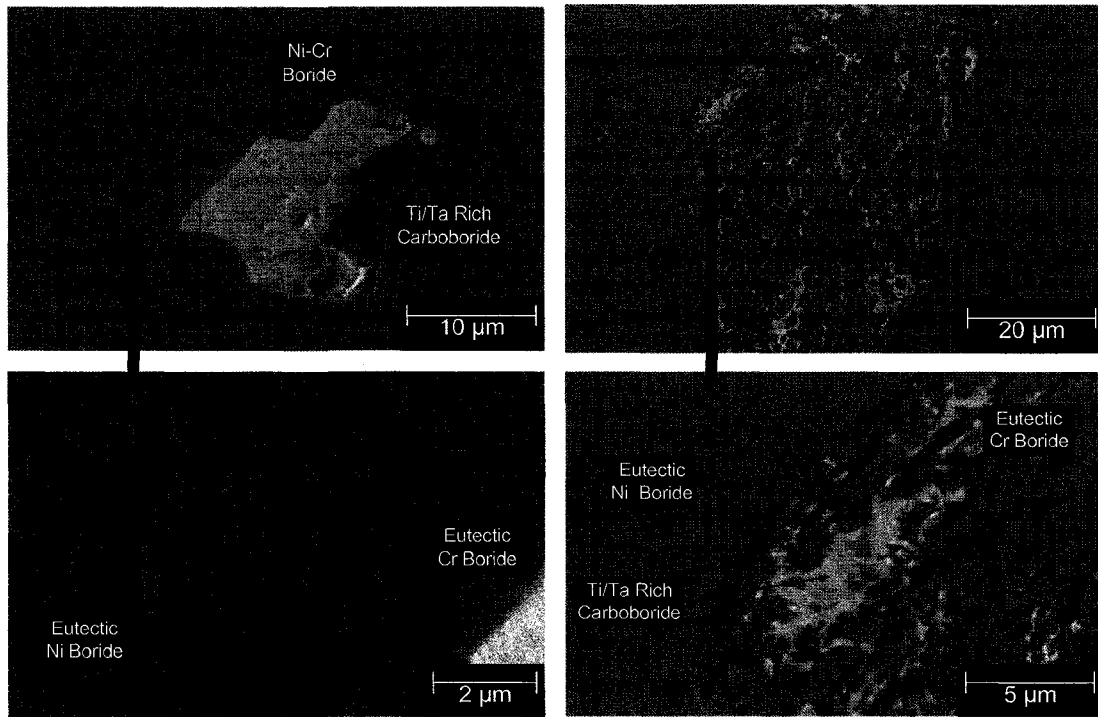


Figure 5-23 - Prominent Phases Found at Interface and in the Substrate of WGB Specimen with IN-738 Additive

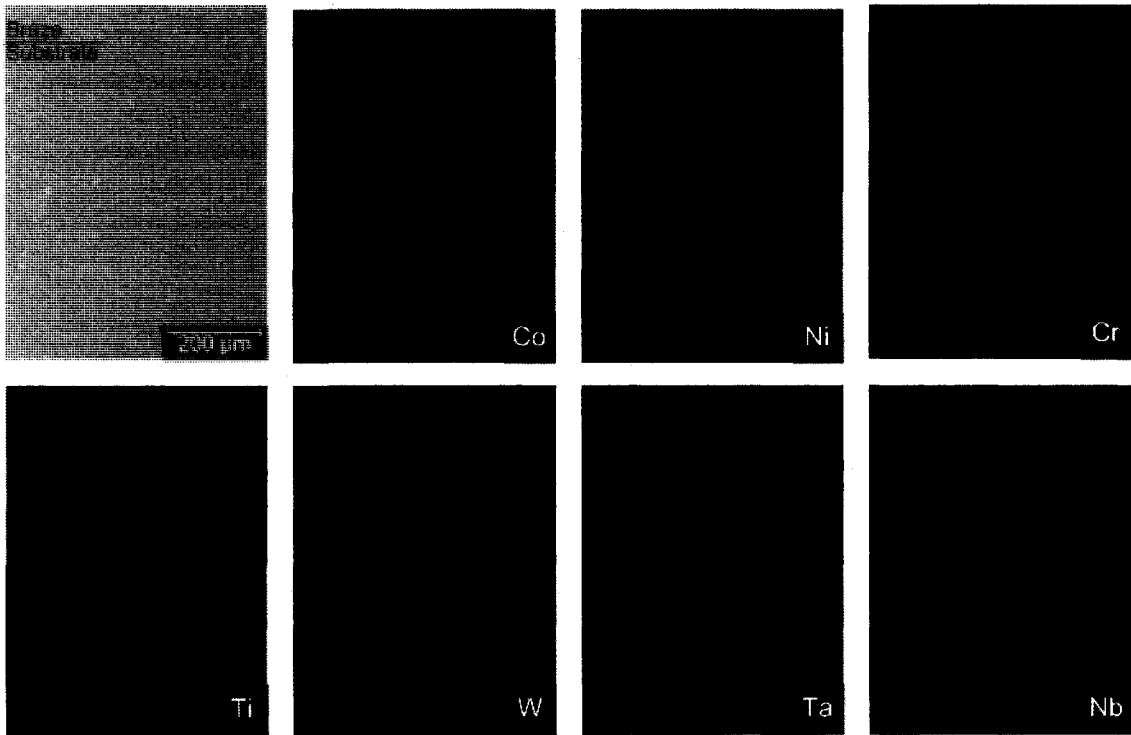


Figure 5-24 - Interface Element Maps of WGB Specimen with IN-738 Additive

### ***Microhardness Measurement***

The hardness of the phases found in the WGB joint with IN-738 additive were assessed using nanoindentation. The average hardness of several indentations of each type of phase are shown in Table 5-8. It was observed that the hardness of the eutectics and the discrete titanium and tantalum rich carboboride phase were higher than that of the primary  $\gamma$ -Ni matrix. The hardness of the nickel chrome boride precipitate could not be observed as it was too small to indent reliably.

**Table 5-8 - Average Nanohardness of Phases Observed in WGB joint with IN-738 Additive**

<b>Phase</b>	<b>Applied Load (mN)</b>	<b>Average Vickers Hardness</b>
Primary $\gamma$ -Ni Matrix	40	613
Eutectic 1	40	1477
Eutectic 2	40	2385
Ti/Ta Rich Carboboride	40	3438
Fine Eutectic	150	848

#### ***5.3.1.3 Summary of WGB Joint Microstructures***

The microstructure of the WGB joints consisted of a primary matrix that was surrounded by eutectic phases, and in the case of the WGB joint with IN-738 additive alloy, discrete boride and carboboride phases were also observed. These eutectics and discrete borides were found to be significantly harder than the primary matrix in both types WGB joint. Large amounts of porosity were observed in both types of WGB joint; the most severe localized porosity being noted in the WGB joint with IN-738 additive. No TCP phases were observed in either type of WGB joint.

### **5.3.2 Tensile Properties**

#### ***5.3.2.1 WGB with X-40 Additive***

The average yield strength and ultimate tensile strength of the WGB joint with X-40 additive were 177 MPa and 323 MPa respectively. As in the baseline specimens, extensometer saturation occurred before final failure of the test coupons, as shown in Figure 5-25, however extrapolation of the available data suggests an average elongation at failure of approximately 12%. This elongation at failure does not represent the braze region only, as the extensometer used in this work had a fixed gauge length, the elongation of a portion of X-40 substrate was also measure. Examination of the test coupons following failure showed an average reduction in area of approximately 22%. The tensile curves shown in Figure 5-25 appear to be quite wavy, this is believed to be due to secondary cracking in the eutectic between the primary (Co-Ni) matrix, shown in Figure 5-26.

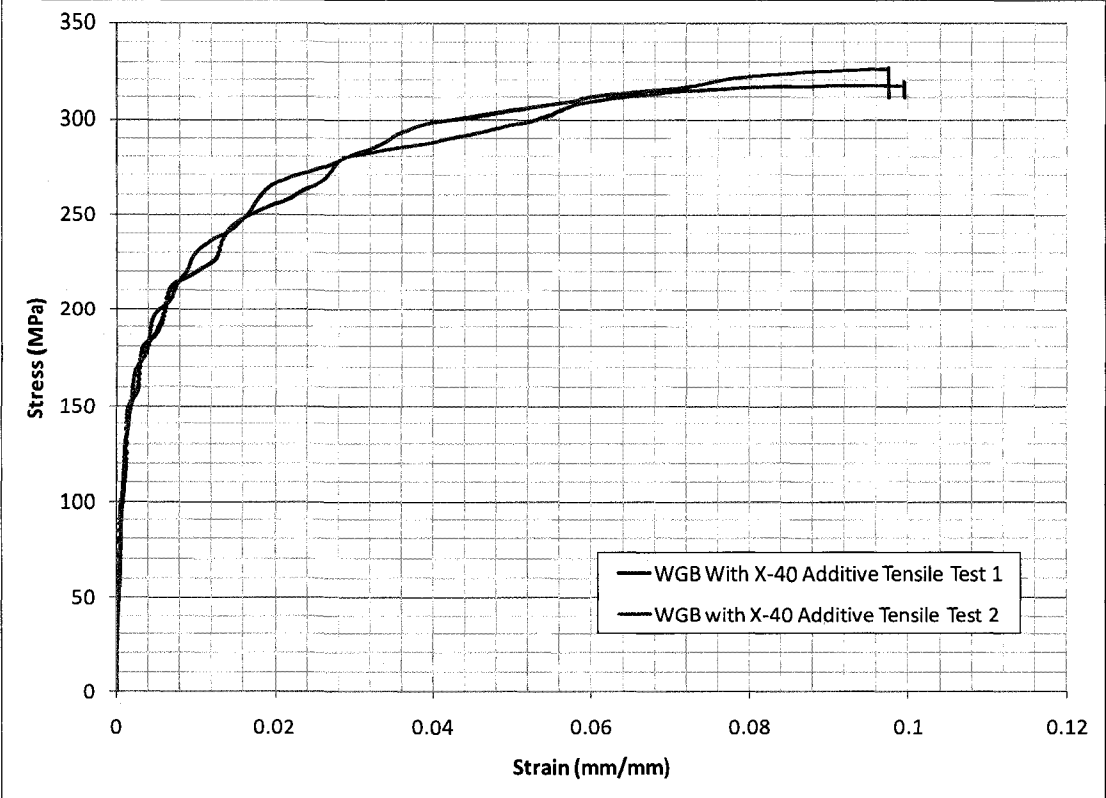


Figure 5-25 - Tensile Curves of WGB with X-40 Additive

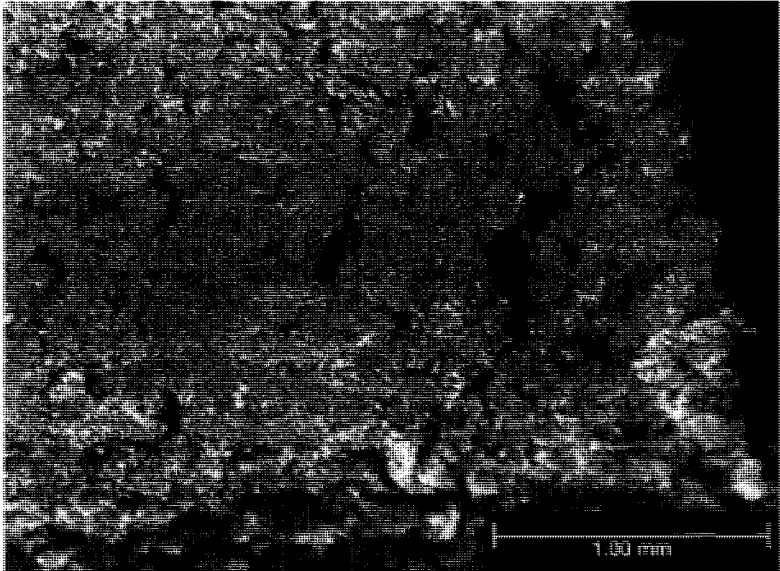


Figure 5-26 - Cracking in WGB with X-40 Additive Alloy Tensile Tested Coupon

### 5.3.2.2 WGB with IN-738 Additive

The average yield strength and ultimate tensile strength of the WGB joint with IN-738 additive alloy were 206 MPa and 276 MPa respectively. Unlike the baseline X-40 and WGB with X-40 additive alloy tests, the ductility of the tape filled wide gap braze joint with IN-738 additive alloy was quite low, as shown Figure 5-27. The average elongation at failure for this type of wide gap braze was measured to be approximately 2.3% (specimens failed at 0.6% and 4%, respectively). This elongation at failure does not represent the braze material by itself, as the extensometer had a fixed gauge length, the elongation of a portion of X-40 substrate was also measured. Examination of the test coupons following failure showed an average reduction in area of approximately 6.53%, (5.95% and 7.11% respectively).

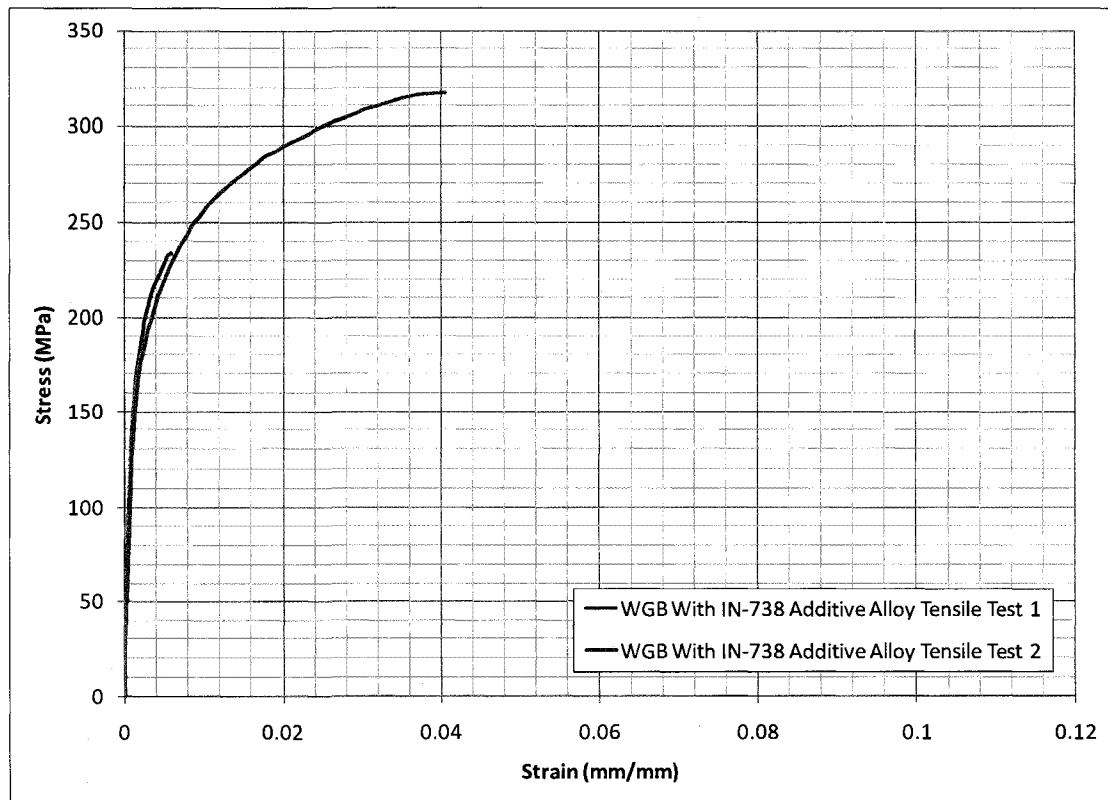


Figure 5-27 - Tensile Curves of WGB Joint, Tape Filled, IN-738 Additive

### 5.3.2.3 Summary of WGB Joint Tensile Properties

The tensile properties of the baseline X-40 bars and WGB joints are listed in Table 5-9 and the average results for each condition are shown graphically in Figure 5-28. It can be seen that the yield strength of both WGB joints was higher than that of the baseline specimens; however the ultimate tensile strength of the WGB joints was below that of the baseline. The ductility of the WGB joints was significantly inferior to that of the baseline X-40 bars, especially in the case of the WGB with IN-738 additive. This lack of ductility is believed to be due to incomplete wetting of the IN-738 powder particles by the BNi-9 braze alloy.

Table 5-9 - WGB Tensile Test at 950°C Results

Condition	Sample	Yield Strength (MPa)	Ultimate Tensile Strength (MPa)	% Elongation	% Reduction in Area
Baseline X-40 Bars	1	170	328	>10	50.2
	2	173	344	>10	44.0
	<i>Average</i>	<i>172</i>	<i>336</i>	<i>&gt;10</i>	<i>47.1</i>
WGB with X-40 Additive	1	179	319	>10	21.8
	2	175	327	>10	23.0
	<i>Average</i>	<i>177</i>	<i>323</i>	<i>&gt;10</i>	<i>22.4</i>
WGB with IN-738 Additive	1	213	234	0.609	5.95
	2	199	318	4.05	7.11
	<i>Average</i>	<i>206</i>	<i>276</i>	<i>2.33</i>	<i>6.53</i>

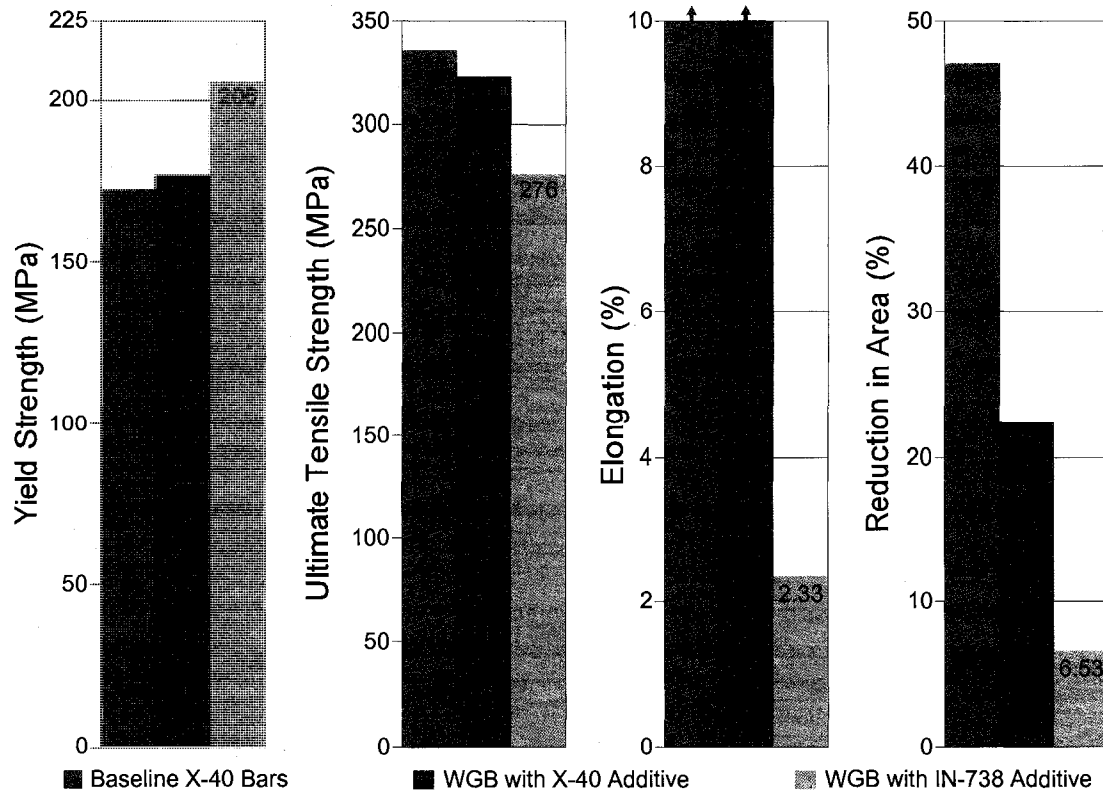


Figure 5-28 - Average WGB Tensile Test at 950°C Results

## 5.4 Fatigue Testing

### 5.4.1 Fatigue Properties of WGB and NGB Joints

The low cycle fatigue lives of the baseline X-40, NGB and WGB specimens tested in the as-brazed condition are shown in Figure 5-29. The low cycle fatigue life of the baseline X-40 bars varied significantly. Of the two specimens tested, one endured 103,607 cycles before failing while the other test was stopped at 250,000 cycles and identified as run out. The reason for this discrepancy may be due to scratches or residual stresses which remained from the machining and polishing processes. It is not uncommon to see a high degree of variability in fatigue life for the same stress level [27], and as such neither of the tests was discarded. The fatigue life of the as-brazed narrow gap braze specimens was quite low in comparison to the baseline specimens. The two as-brazed NGB fatigue

coupons endured 30,715 and 37,405 cycles respectively. This low life is deemed to be due to the limited ductility in the braze joint due to the presence of brittle borides and carbides in the braze region. The fatigue life of the WGB joint with X-40 additive ranged between 78,674 and 124,236 cycles, while WGB joint with IN-738 additive endured 27,614 to 37,816 cycles until failure. This difference is attributed to the higher ductility and reduced porosity observed in the WGB joint with X-40 additive. It can be said that fatigue crack nucleation did not occur in either of the wide gap braze configurations as the significant amount of porosity observed in each most likely caused immediate crack growth upon cyclic loading. As mentioned earlier the porosity in the WGB joint with IN-738 additive was highly localized resulting in macrovoids in certain areas and lower fatigue life.

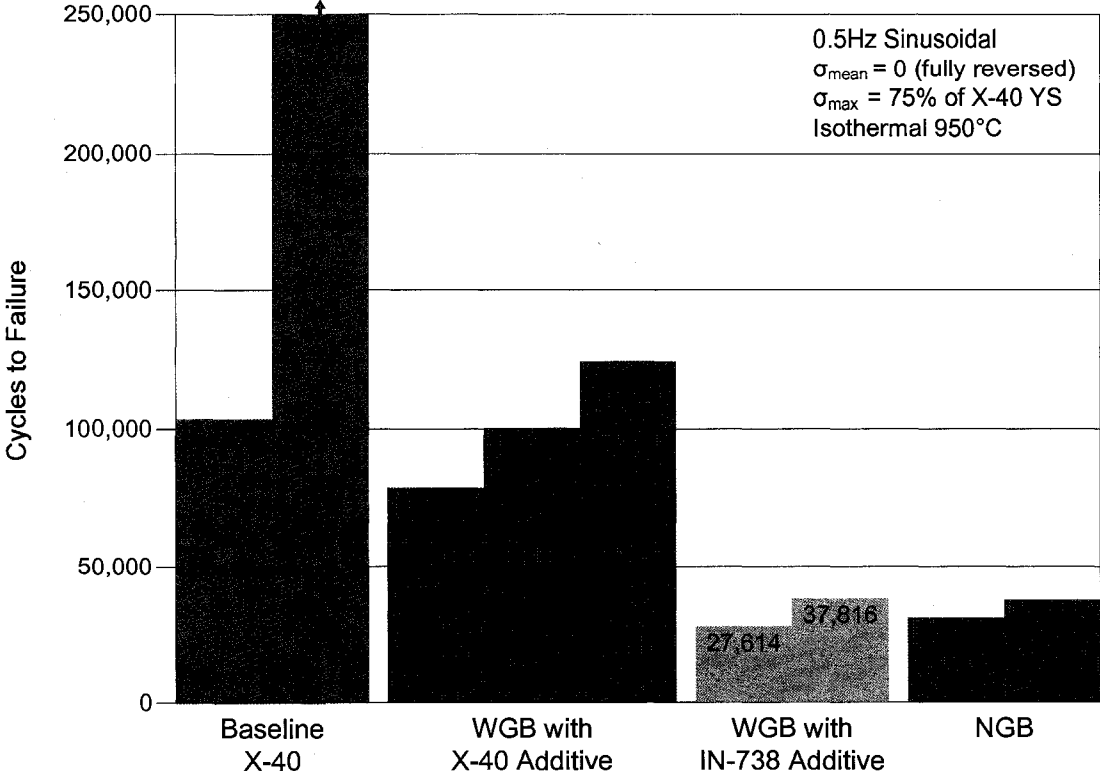


Figure 5-29 - WGB and NGB Fatigue Test Results

## **5.4.2 Fatigue Coupon Fractography**

### ***5.4.2.1 Baseline X-40 Coupons***

Figure 5-30 shows a representative low cycle fatigue fracture surface of the baseline X-40 bars. The bottom portion of the fracture surface, which shows a clear river pattern, is the fatigue region and the top portion of the fracture surface, which shows fracture along the dendrite arms of the material, is the overload region. Fatigue in the baseline X-40 bars was believed to be initiated at the surface of the coupon, via a surface imperfection or due to oxidation of the coupon, the initiation site is shown in Figure 5-31A. No fatigue striations were visible near the initiation site due to oxidation of the fracture surface however fatigue striations were evident in the high crack growth rate region of the fracture surface, shown in Figure 5-31B. The overload region of the fracture surface was characterized by cracks branching into the secondary dendrite arms, shown in Figure 5-31C, which were exposed upon fracture surface of the test coupon.

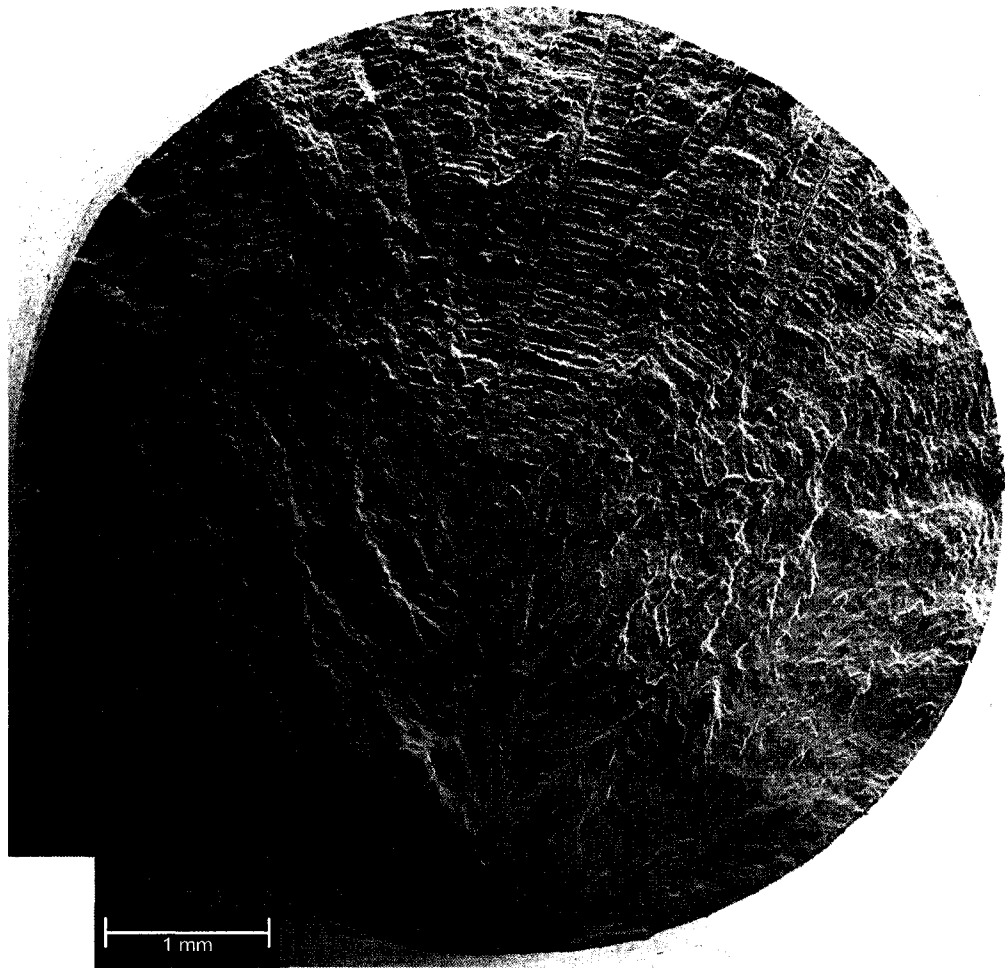
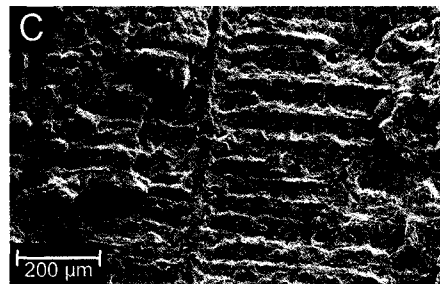
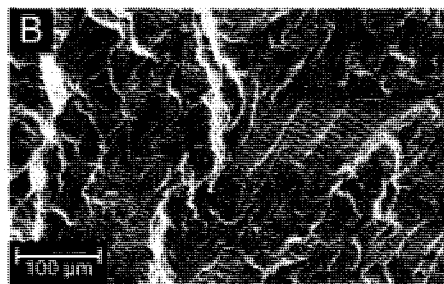
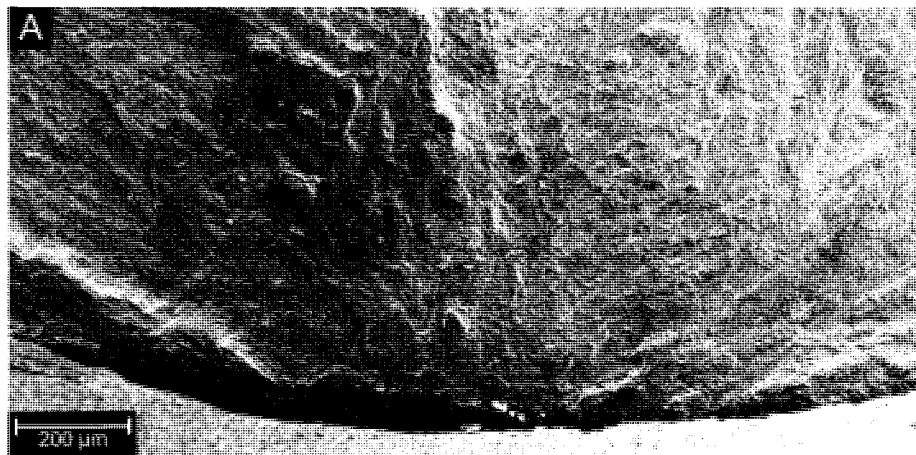
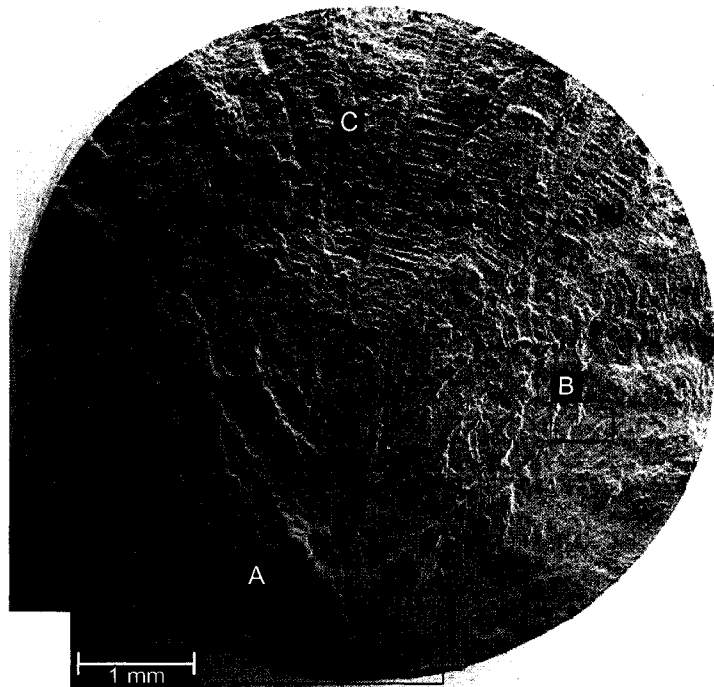


Figure 5-30 - Baseline X-40 Low Cycle Fatigue Coupon Fracture Surface



**Figure 5-31 - Features of Baseline X-40 Low Cycle Fatigue Coupon Fracture Surface (A) Possible Initiation Site, (B) Fatigue Striations In High Crack Growth Region, (C) Cracking Between Eutectic Arms in Overload Region of Fracture Surface**

#### ***5.4.2.2 As-Brazed NGB Coupons***

Fatigue striations were not found on any of the low cycle fatigue fracture surfaces of the as-brazed narrow gap braze coupons, as shown in Figure 5-32. However, the top portion of the fracture surface shown in Figure 5-32 is similar in appearance to the narrow gap braze tensile fracture surfaces, thus this portion of the fracture surface was assumed to be the overload region. Figure 5-33A shows the possible initiation point of one of the low cycle fatigue fracture surfaces of the narrow gap braze coupons. This location is believed to be the initiation site as it displays a high degree of discontinuity when compared to the rest of the fatigue portion of the fracture surface. As in the tensile coupons, significant interface separation occurred in the overload region of the fracture surface, as shown by the exposed braze alloy eutectic phases and unmelted braze alloy particles shown in Figure 5-33 B and C respectively.

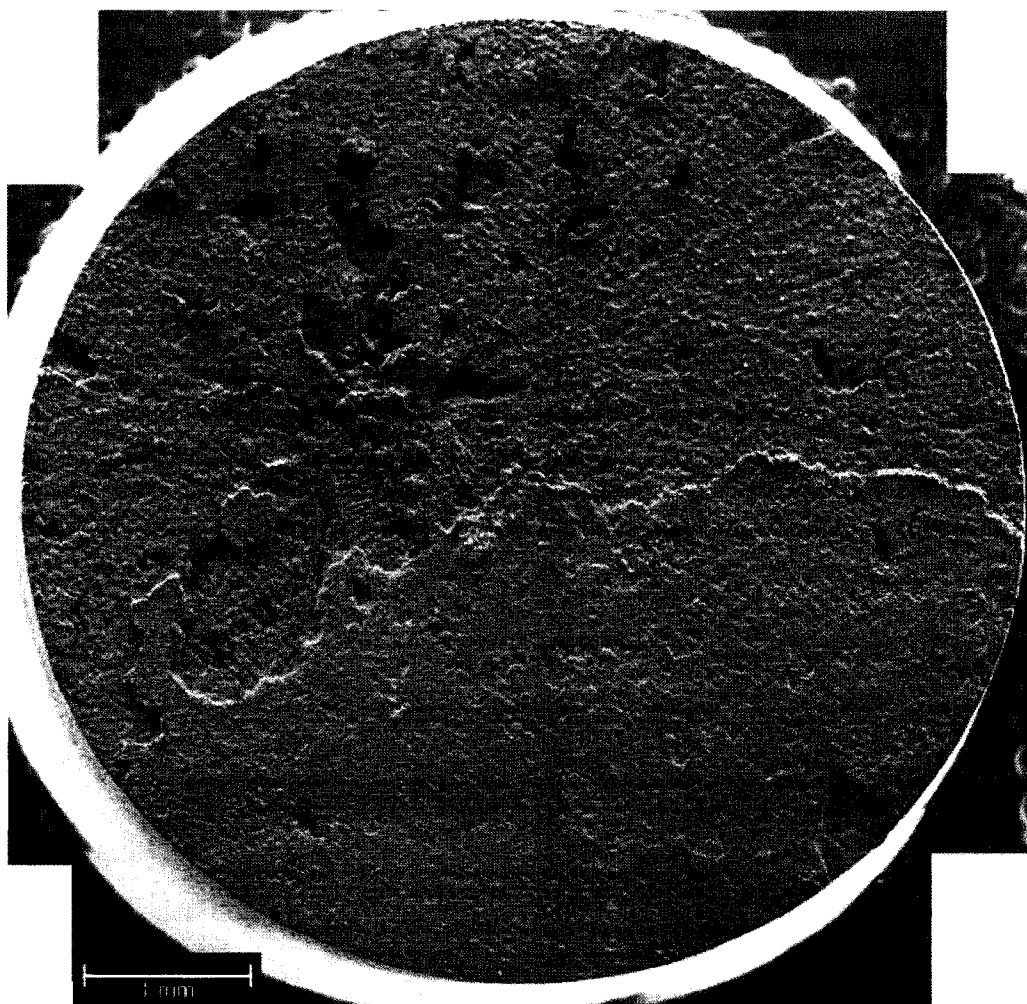


Figure 5-32 - As-brazed Narrow Gap Braze Low Cycle Fatigue Coupon Fracture Surface

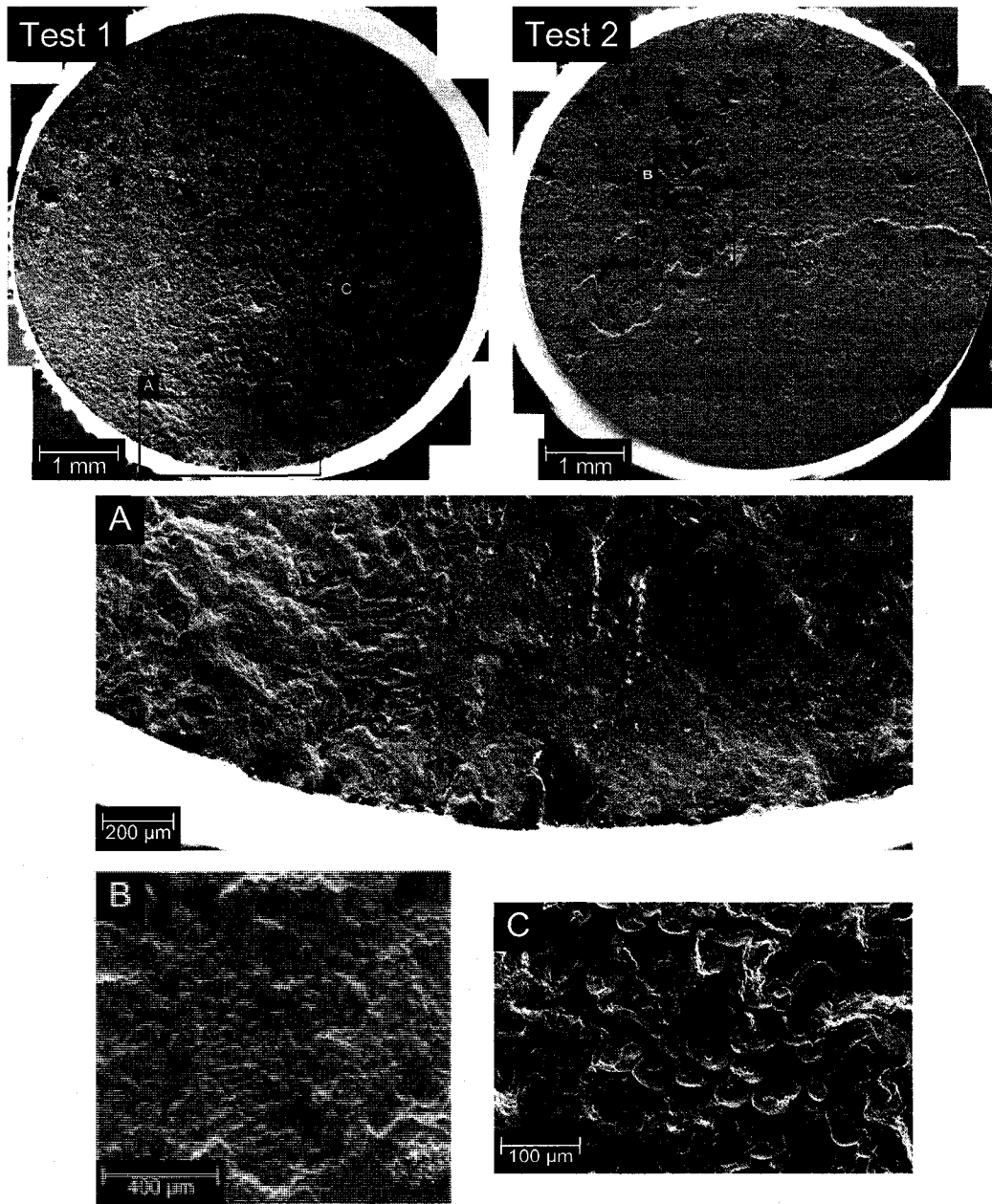
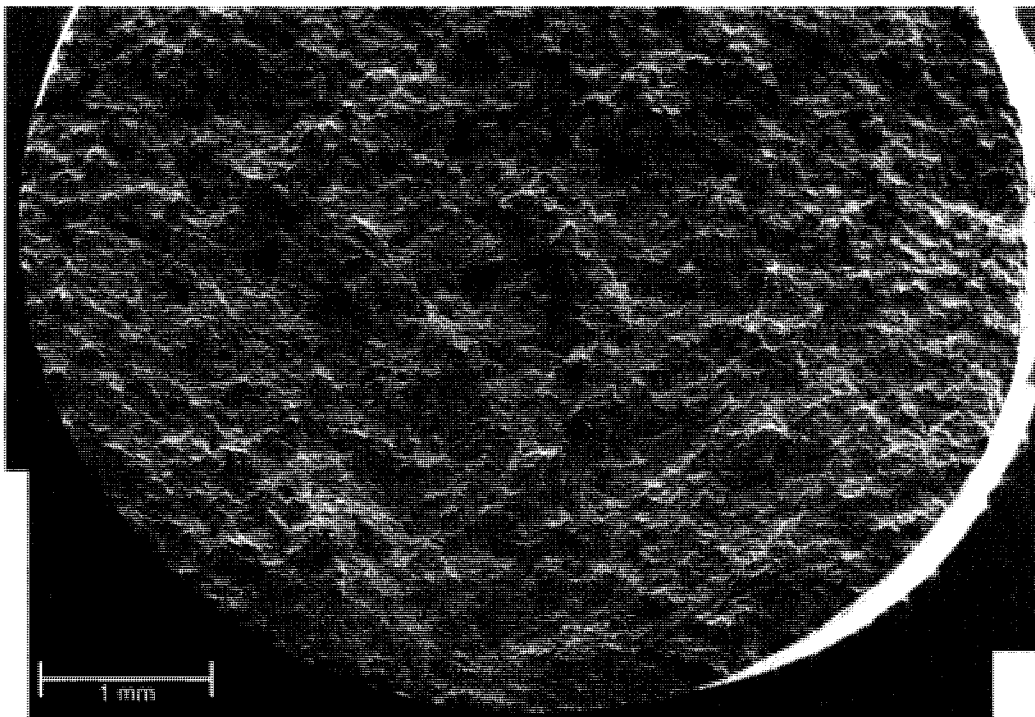


Figure 5-33 - Features of an As-brazed Narrow Gap Braze Low Cycle Fatigue Coupon Fracture Surface (A) Possible Initiation Site, (B) Exposed Eutectic in Overload Region of Fracture Surface, (C) Partially Unmelted Braze Alloy Powder Particles

#### 5.4.2.3 WGB with X-40 Additive

While no fatigue striations were found on the low cycle fatigue fracture surface of the WGB joint with X-40 additive alloy, a slight river pattern on the bottom and pullout type appearance on the top of Figure 5-34 suggests that the bottom portion of the fracture

surface is the fatigue region. The overload region of the low cycle fatigue fracture surface of this type of braze coupon appears to consist of fracture through the interface between the eutectic phases and the primary (Co-Ni), leaving the primary (Co-Ni) phase exposed. The initiation site of one test coupon is shown in Figure 5-35, this region shows a slight river pattern towards the outer surface of the test coupon. A significant amount of porosity and/or secondary cracking occurred in the braze alloy in this type of braze joint.



**Figure 5-34 - WGB Joint With X-40 Additive Alloy Low Cycle Fatigue Coupon Fracture Surface**

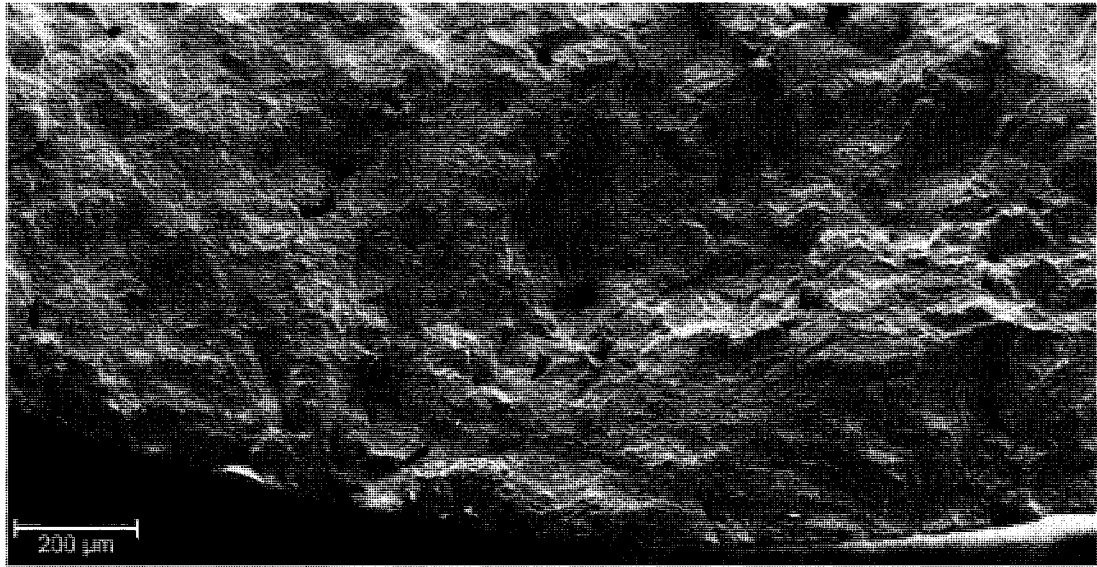
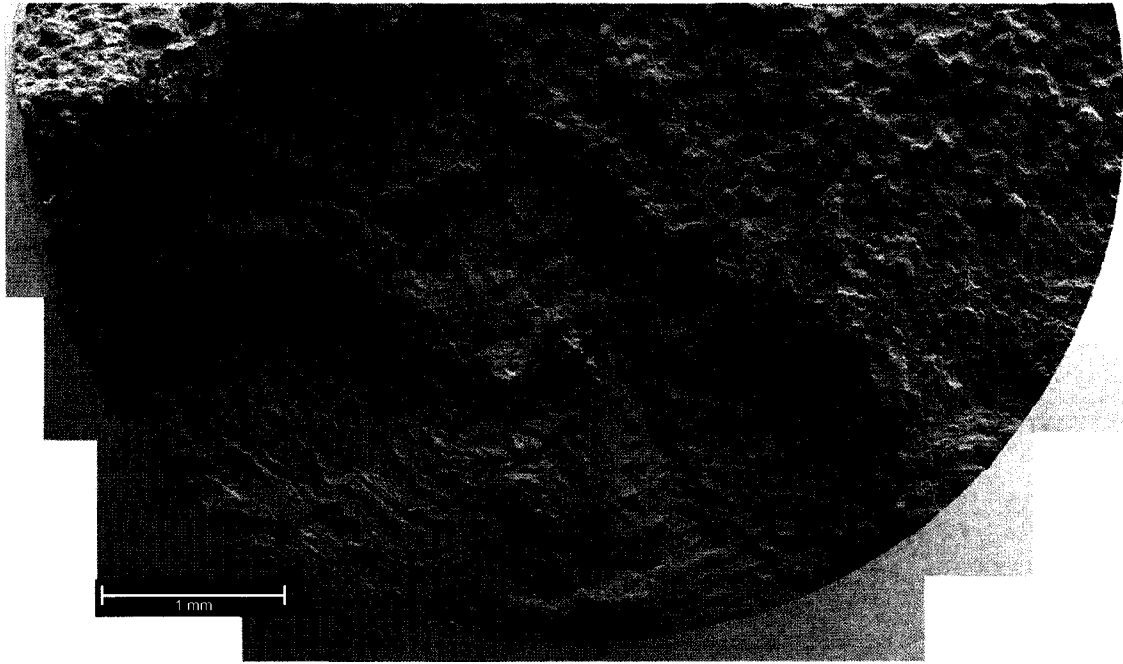


Figure 5-35 - Initiation Site of WGB Joint with X-40 Additive Alloy Low Cycle Fatigue Coupon Fracture Surface

#### ***5.4.2.4 WGB with IN-738 Additive***

The fatigue region of the fracture surface shows a clear river pattern, as shown in Figure 5-36. Crack initiation in this type of braze was believed to be internal, as shown in Figure 5-37A, areas of significant porosity served as excellent sites for crack initiation. While no fatigue striations were visible at the possible location of fatigue crack initiation due to oxidation of the fracture surface, near the high crack growth region, fatigue striations were easily recognizable, as shown in Figure 5-37B. Significant secondary cracking occurred in the fatigue region of the fracture surface of this type of braze coupon, as shown in Figure 5-37C. As in the WGB joint with X-40 additive, the overload region of low cycle fatigue fracture surface the WGB joint with IN-738 additive appears to fracture along the interface between the primary  $\gamma$ -Ni phase and eutectic phases due to the presence of brittle phases, shown in Figure 5-37D.



**Figure 5-36 - Fatigue Portion of WGB Joint with IN-738 Additive Alloy Low Cycle Fatigue Coupon Fracture Surface**

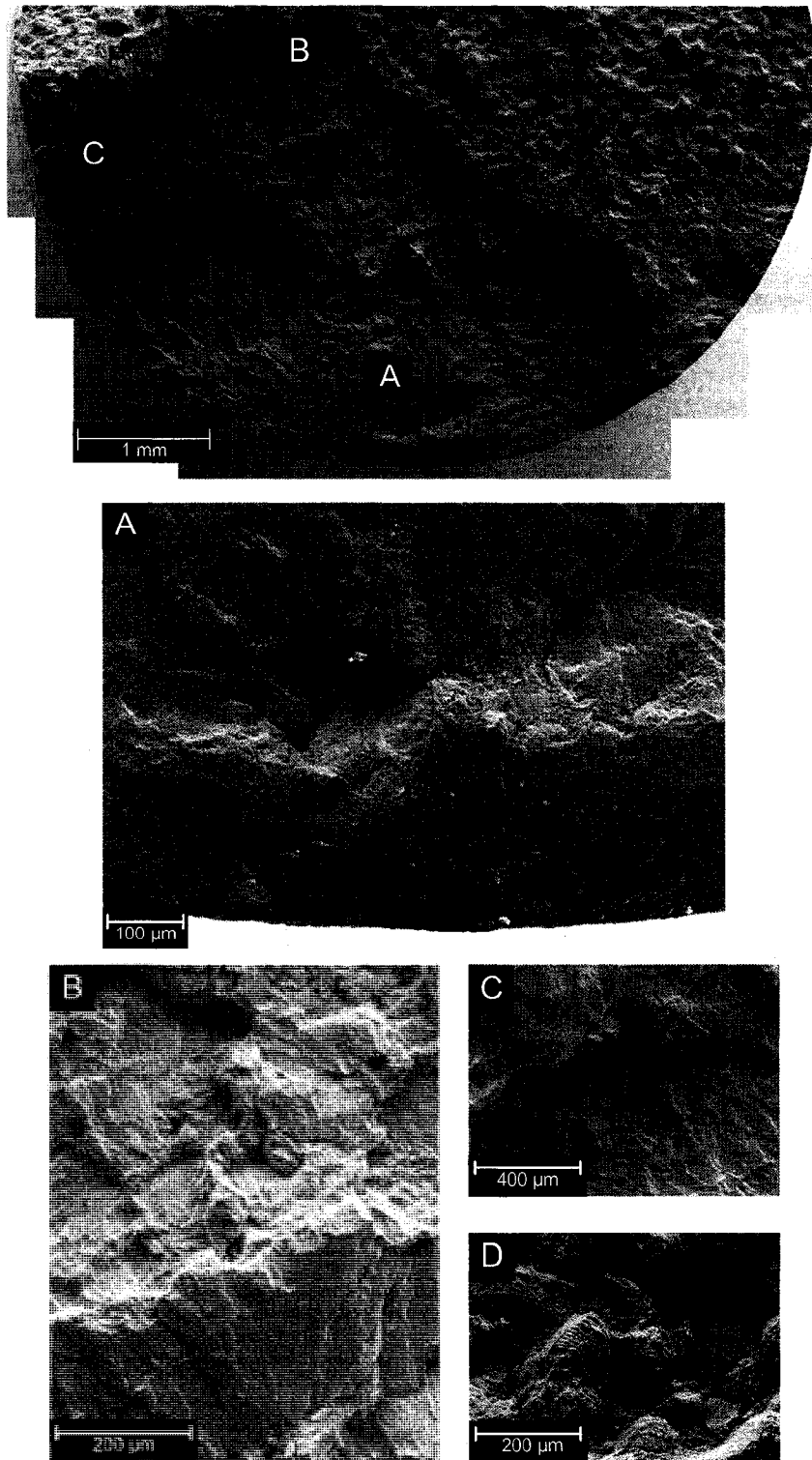


**Figure 5-37 - Features of a WGB Joint with IN-738 Additive Alloy Low Cycle Fatigue Coupon Fracture Surface (A) Possible Initiation Site Showing Fatigue River Pattern, (B) Fatigue Striations Near High Crack Growth Rate Zone, (C) Secondary Cracking in High Crack Growth Zone, (D) Exposed Eutectic Pattern in Overload Region of Fracture Surface (not shown in overview image)**

### **5.4.3 Summary of Fatigue Test Results**

The fatigue performance of the NGB and WGB specimens were substantially inferior to that of the baseline X-40. The low fatigue life of the as-brazed NGB specimens may be a result of the low ductility of the braze resulting from the presence of brittle eutectics and carbides/borides/carboborides in the braze, evident by the exposed eutectic pattern of Figure 5-33B. The difference in fatigue performance between the WGB joints with X-40 additive and IN-738 additive can be attributed largely to the higher ductility observed for the WGB joint with X-40 additive and the brittle borides and increased porosity observed in the braze region of the WGB joint with IN-738 additive.

## **Chapter 6. Conclusions and Recommendations for Future Work**

### **6.1 Conclusions**

In this research, repair methods based on both narrow and wide gap brazing were developed for stationary turbine airfoils, namely nozzle guide vanes, made from cobalt-base superalloy X-40. The main mode of failure for these X-40 nozzle guide vanes is thermal fatigue. Narrow gap braze repair can be utilized in crack healing and bonding of inserts. Wide gap braze repair on the other hand is employed when large voids, greater than 200  $\mu\text{m}$ , are to be filled in one braze operation. As IN-738 has been found to exhibit higher low cycle fatigue life than X-40, the level of utility of IN-738 additive alloys and nickel-base braze alloys was explored in this research.

Both repair methods were successfully developed, as detailed in the previous chapters. The repair methods were able to produce sound joints with minimal defects, particularly in the narrow gap braze joints. The microstructure of the narrow and wide gap joints were characterized using optical and scanning electron microscopy and microhardness testing to assess the hardness of the individual constituents of the joints. Finally, high temperature tensile and low cycle fatigue testing was conducted to evaluate the joint mechanical properties with respect to the performance of X-40 superalloy.

The occurrence of discrete borides/carbides and eutectic phases was observed in both the NGB and WGB joints. These phases were found to be significantly harder than the superalloy substrates, causing them to act as crack initiation sites during both tensile and fatigue testing.

The as-brazed NGB joints were found to have higher yield strength but slightly lower ultimate tensile strength than the baseline X-40. Although both the differences between yield strength and ultimate tensile strength of the as-brazed NGB joints were within +/-10% of X-40, the ductility of the joint was significantly lower than the baseline, resulting in low cycle fatigue life lower than the baseline.

Post-brazing heat treatments reduced the detrimental effects of the discrete borides/carbides and eutectic phases, however the length of the heat treatment required to remove these phases may not be feasible on a large scale. With proper post-brazing heat treatment, the ductility of the NGB joints was significantly improved. Although low cycle fatigue testing was not carried out on the heat treated samples it can be postulated that the fatigue life would increase accordingly due to the reduction of the secondary phases in the braze region.

The main conclusions that can be drawn from the narrow gap braze investigation are:

- The presence of eutectic phases and discrete carbides/carboborides along the grain boundaries of the primary  $\gamma$ -Ni phase is detrimental to the mechanical properties of a braze joint.
- Post-brazing heat treatment can reduce the quantity and size of the eutectic phases and discrete carbides/carboborides that surround the primary  $\gamma$ -Ni, though extended heat treatment at 950°C for 840 hours does not result in complete removal of these secondary phases. Reduction in the eutectic phases and discrete carbides/carboborides is beneficial to the tensile strength and

ductility of the braze joint, this improvement can be attributed to modification of the fracture mode from intergranular to transgranular.

- When post-brazing heat treatment is conducted in air, prolonged exposure will induce oxidation that adversely effects the tensile properties of the braze joint.

In the WGB research, joints were formed with a nominal 2:1 ratio of additive alloy (X-40 or IN-738) to braze alloy (BNi-9), using two different braze filler preplacement approaches. As IN-738 has poor wettability in WGB with slurry filler, resulting in large pores, sandwiched tape, a method found to improve the wetting of the IN-738 powder particles was used. The WGB joints made with X-40 and IN-738 additives were found to be free of macroscopic defects, although some small pores were found. As expected in all WGB joints, the midbraze region contained brittle discrete borides/carbides and eutectic phases. These secondary phases had a lower occurrence than observed in the NGB joints, where the secondary phases formed a continuous network around the primary  $\gamma$ -Ni phase. Microstructural evaluation showed that the utilization of nickel-base IN-738 additive alloy and BNi-9 braze alloy with cobalt-base X-40 substrate did not cause the formation of TCP phases in either midbraze or interface regions.

The tensile properties of the as-brazed WGB joints with X-40 additive showed lower yield strength than the WGB joint with IN-738 additive, however higher ductility was observed in the WGB joints with X-40 additive. The yield strength of both WGB braze joints was higher than the baseline X-40, however the ultimate tensile strength was lower and the ductility, as measured by elongation and reduction in area, was significantly lower in the WGB joints. The failure locations in the WGB joints were

identified as being the midbrazed region, further illustrating the brittle nature of the brazed joints. High temperature low cycle fatigue tests showed that the fatigue life of the WGB joints with X-40 and IN-738 additives were significantly lower than the baseline X-40. Failure locations were again found within the midbrazed region.

The main conclusions that can be drawn from the wide gap brazed investigation are:

- WGB joints with 2:1 ratio between additive (X-40 or IN-738) and braze alloy (BNi-9) produced a significant amount of brittle discrete boride/carbide and eutectic phases in the midbrazed region. The distribution of these phases was discontinuous.
- The use of nickel-base additive and braze alloys did not result in the formation of TCP phases in the midbrazed region and the interface region between X-40 and the braze joint.
- The high temperature tensile yield strength of the as-brazed WGB joints with X-40 and IN-738 additive were greater than baseline X-40, however the ultimate tensile strength was lower than the baseline and ductility was significantly lower. The reduced ductility was attributed to the presence of brittle secondary phases.
- The high temperature low cycle fatigue life of the as-brazed WGB joints with X-40 and IN-738 additives were significantly lower than that of the baseline X-40.
- As expected, high temperature tensile strength of the WGB joints did not show any correlation with the associated low cycle fatigue life, as repair joints are generally not homogeneous.

## 6.2 Recommendations for Future Work

Future work on this research should proceed in one or all of the following directions:

- **Reduction of porosity through sintering or hot isostatic pressure:** It was evident through this research that one limiting factor of the fatigue life of the wide gap braze joints was the extensive porosity observed regardless of the additive alloy used. Fatigue life improvements could possibly be made by applying filler to the braze joint in the form of a sintered or hot isostatically pressed preforms. While the costs associated with sintering or applying hot isostatic pressure to the filler alloy mixture may be high, the benefits from reduced porosity may justify the added expense. Follow-up research should involve production of a block of sintered braze filler and hot isostatically pressed braze filler. These blocks could then be cut to the required size for the braze joint that is to be formed and either cemented or tack welded into place prior to brazing.
- **Improved wetting of IN-738 additive alloy particles:** A limiting factor in the fatigue life of the wide gap braze joint with IN-738 additive alloy was the wetting of the IN-738 powder particles. Stable oxide formation on the surface of the IN-738 particles which did not dissociate in the vacuum furnace during brazing reduced the wettability of the powder particles by the liquid braze alloy. Resolution of this wetting issue should be a focus of future efforts in this research. Two possible solutions to this problem have been proposed, i) performing fluoride ion cleaning on the additive alloy particles, and ii) nickel

coating the additive alloy particles through vapour deposition shortly after they are formed. Both of these methods would most likely lead to improvements to the fatigue performance of braze joints containing the IN-738 additive alloy.

- **Examination of alternative alloys:** Future work on this research could involve investigation of other alternative nickel-base and perhaps newer cobalt-base additive alloys such as Mar-M 247 or Mar-M 509 respectively, as well as examination into the use of other, more complex braze alloys. The use of superior additive and braze alloys could lead to a braze joint with improved quality.
- **Baseline fatigue testing:** Several more fatigue tests should be performed on the baseline X-40 bars to determine the actual fatigue life for the loading conditions used in this work.

## References

- [1] Betteridge, W. (1982). COBALT and its Alloys. Toronto: John Wiley & Sons Inc.
- [2] Jurgens, W., & Hamburg, M. (1985). Wide Gap Brazing in the Maintenance of Turbine Guide Vanes. DVS Berichte , 98, 78-82.
- [3] Gove, K. (1989). Braze Repair of Aero Engine Components. Metals and Materials, 5, 341-345.
- [4] Mattheij, J. H. (1985). Role of Brazing in Repair of Superalloy Components - Advantages and Limitations. Materials Science and Technology, 1 (8), 608-612.
- [5] Heikinheimo, L. (2001). Repair Brazing of Gas Turbine Hot Parts - Methods and Joint Characterisation. VVT Symposium (211), 149-162.
- [6] Gandy, D. W., Frederick, G., Stover, J. T., & Viswanathan, R. (2001). Overview of Hot Section Component Repair Methods. Electric Power Research Institute, Repair and Replacement Application Center, Charlotte.
- [7] O'Neill, W. M. (9-12 October 2000). Braze Repair of Gas Turbine Components: Retrospective, Perspective, Prospective. ASM Heat Treating Society, (pp. 1040-1045).
- [8] Fritsche, B., & Satir-Kolorz, A. (2000). Repair Brazing of Nickel-Base Turbine Blades. Welding in the World, 44, 10-14.
- [9] Demo, W. A., & Ferrigno, S. J. (1992). Brazing Method Helps Repair Aircraft Gas Turbine Nozzles. Advanced Materials & Processes, 3 (92), 43-45.
- [10] Liburdi, J., & Ellison, K. A. (1993). Novel Approach to the Repair of Vane Segments. International Gas Turbine and Aero Engine Congress, (pp. 24-27).
- [11] McMurray, J., & Miller, J. (1983). Patent No. 4,394,347. U.S.
- [12] Au, P., & Dainty, R. V. (1989). Isothermal Low Cycle Fatigue Properties of Diffusion Aluminide Coated Nickel and Cobalt Based Superalloys. Surface Modification Technologies III, 729-748.
- [13] Cohen, H., Rogers, G., & Saravanamuttoo, H. (1996). Gas Turbine Theory (4th ed.). London, England: Longman Group Limited.
- [14] Moran, M. J., & Shapiro, H. N. (2004). Fundamentals of Engineering Thermodynamics (5th ed.). Hoboken, NJ, USA.

- [15] Rolls-Royce: Defence Aerospace. (2004). Retrieved 03 12, 2008, from Rolls-Royce Plc.: [http://www.rolls-royce.com/defence\\_aerospace/default.jsp](http://www.rolls-royce.com/defence_aerospace/default.jsp)
- [16] The Jet Engine (5th Ed. ed.). (1996). Derby: Rolls-Royce Plc.
- [17] Donachie, M. J., & Donachie, S. J. (2002). Superalloys: A Technical Guide. Materials Park: ASM International.
- [18] Reed, R. C. (2006). The Superalloys: Fundamentals and Applications. New York: Cambridge University Press.
- [19] Durand-Charre, M. (1997). The Microstructure of Superalloys. Amsterdam: Gordon and Breach Science Publishers.
- [20] Sims, C. T., Stoloff, N. S., & Hagel, W. C. (1987). Superalloys II. New York: John Wiley & Sons, Inc.
- [21] Sims, C. T., & Hagel, W. C. (1972). The Superalloys. New York: John Wiley & Sons Inc.
- [22] Sullivan, C. P., Donachie, J. M., & Morral, F. R. (1970). Cobalt-Base Superalloys-1970. Brussels: Centre D'information Du Cobalt.
- [23] Day, J. J. (2004). Gas Turbine Blade Hardfacing Process Development and Microstructural Study of the Interface. Ottawa: Carleton University Mechanical and Aerospace Engineering Department.
- [24] Bettge, D., Osterle, W., & Ziebs, J. (1995). Temperature Dependence of Yield Strength and Elongation of Nickel-Base Superalloy IN738LC and the Corresponding Microstructural Evolution. *Z. Metallkd*, 86 (3), 190-197.
- [25] Spera, D. A., & Mowbray, D. F. (1975). Thermal Fatigue of Materials and Components. Philadelphia: American Society for Testing and Materials.
- [26] Weronki, A., & Hejwowski, T. (1991). Thermal Fatigue of Metals. New York: Marcel Dekker, Inc.
- [27] Sandor, B. I. (1972). Fundamentals of Cyclic Stress and Strain. Madison: The University of Wisconsin Press.
- [28] Bressers, J. (1981). Creep and Fatigue in High Temperature Alloys. London: Applied Science Publishers Ltd.
- [29] Brandon, D., & Kaplan, W. D. (1997). Joining Processes: An Introduction. New York: John Wiley & Sons Inc.

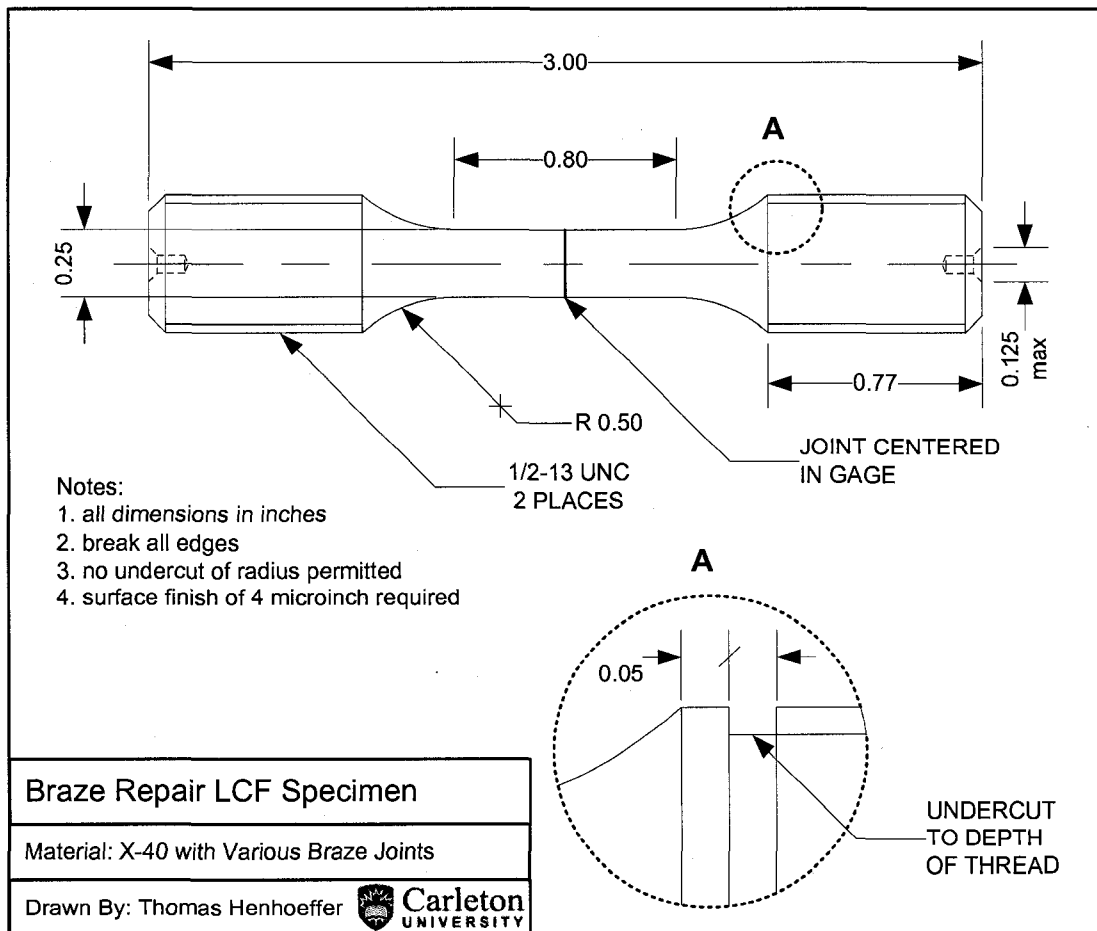
- [30] Johnson, R. (1987). Brazing - A High Technology Joining Process. *Welding & Metal Fabrication* , 55, 433-440.
- [31] Nicholas, M. G. (1998). *Joining Processes: Introduction to Brazing and Diffusion Bonding*. Boston: Kluwer Academic Publishers.
- [32] Handy & Harman (1997). *The Brazing Book*. New York, IRN10891201.
- [33] Schwartz, M. M. (1987). *Brazing*. Materials Park, Ohio: ASM International.
- [34] Messler, R. W. (1993). *Joining of Advanced Materials*. Boston: Butterworth-Heinemann.
- [35] Paponetti, C. (1993). *Introduction to Vacuum Thermal Processing. Vacuum Technology: Practical Heat Treating and Brazing* (pp. 25-44). ASM International.
- [36] Miglietti, W. M. (2000). Wide Gap Diffusion Braze Repair of Co-Based Industrial Turbine Vanes. *International Brazing & Soldering Conference*, (pp. 476-485).
- [37] Wall Colmonoy Corporation. (n.d.). *Nicrobraz(R) Filler Metal Selector Chart*. Retrieved October 2006, from <http://www.wallcolmonoy.com/>
- [38] Praxair Technology Inc. (n.d.). *Thermal Spray Products: Powders and Wires*. Retrieved October 2006, from <http://www.praxair.com/>
- [39] Sulzer Metco. (n.d.). *Thermal Spray and Braze Materials*. Retrieved October 2006, from <http://www.sulzermetco.com/>
- [40] Lim, L. C., Lee, W. Y., & Lai, M. O. (1995). Nickel Base Wide Gap Brazing With Preplacement Technique: Part 1 - Effect of Material Process Parameters on Formation of Macrovoids. *Material Science and Technology*, 11, 955-960.
- [41] Oyama, T. (2000). High Temperature Braze Repair of Aero-Engine Components. *IBSC 2000: International Brazing & Soldering Conference*, (pp. 486-493).
- [42] Moffat, W. G. (1984). *The Handbook of Binary Phase Diagrams*. New York: Genium Publishing Corporation.
- [43] Greaves, W. (2005). Cost-Effective Repairs for Turbine Vanes with Vacuum Brazing. *Sulzer Technical Review*, 1, 19-21.
- [44] Tung, S. K., Lim, L. C., & Lai, M. O. (1995). Microstructural Evolution and Control in BNi-4 Brazed Joints of Nickel 270. *Scripta Metallurgica et Materialia*, 33 (8), 1253-1259.

- [45] Lugscheider, E., & Humm, S. (2002). High-Temperature Brazing of Superalloys and Stainless Steels with Novel Ductile Ni-Hf-Based Filler Metals. *Advanced Engineering Materials*, 4 (3), 138-142.
- [46] Henhoeffler, T. R., Huang, X., Seo, D., Yandt, S., & Au, P. (n.d.). Microstructure and High Temperature Tensile Properties of Narrow Gap Braze Joint between X-40 and IN-738. *Journal of Materials Science and Technology*. Submitted May, 2008.
- [47] Liburdi Turbine Services Inc. (n.d.). Liburdi Turbine Services. Retrieved October 2006, from <http://www2.liburdi.com/liburditurbine/index.php>
- [48] Standard Aero Limited. (n.d.). Aerospace Engine Services. Retrieved October 2006, from <http://www.standardaero.com/>
- [49] Ellison, K., & Liburdi, J. (2003). Patent No. 6624225 B1. U.S.
- [50] Ellison, K., & Liburdi, J. (2004). Patent No. 6797759 B1. U.S.
- [51] Ellison, K., & Liburdi, J. (2006). Patent No. 7115679 B2. U.S.
- [52] White, R. A., & Lau, Y. C. (1998). Patent No. 5732467. U.S.
- [53] Beltran, A. M., & Kreischer, C. H. (1993). Patent No. 5182080. U.S.
- [54] Beltran, A. M., & Kreischer, C. H. (1994). Patent No. 5320690. U.S.
- [55] Miglietti, W. (1993). Correlation Between Microstructure and Mechanical Properties of Diffusion Brazed MAR-M-247. *International Gas Turbine and Aeroengine Congress and Exposition* (p. 10). Cincinnati: ASME.
- [56] Chaturvedi, M. C., Ojo, O. A., & Richards, N. L. (2005). Diffusion Brazing of Cast Inconel 738 Superalloy. *Journal of Materials Online*, 1, 1-12.
- [57] Su, C. Y., Lih, W. C., Chou, C. P., & Tsai, H. C. (2001). Activated Diffusion Brazed Repair For IN738 Hot Section Components of Gas Turbines. *Journal of Materials Processing Technology*, 115, 326-332.
- [58] Wu, X. W., Chandel, R. S., Seow, H. P., & Li, H. (2001). Wide Gap Brazing of Stainless Steel to Nickel-Based Superalloy. *Journal of Materials Processing Technology*, 113, 215-221.
- [59] Wu, X., Chandel, R. S., & Li, H. (2001). Evaluation of Transient Liquid Phase Bonding Between Nickel-Based Superalloys. *Journal of Materials Science*, 36, 1539-1546.

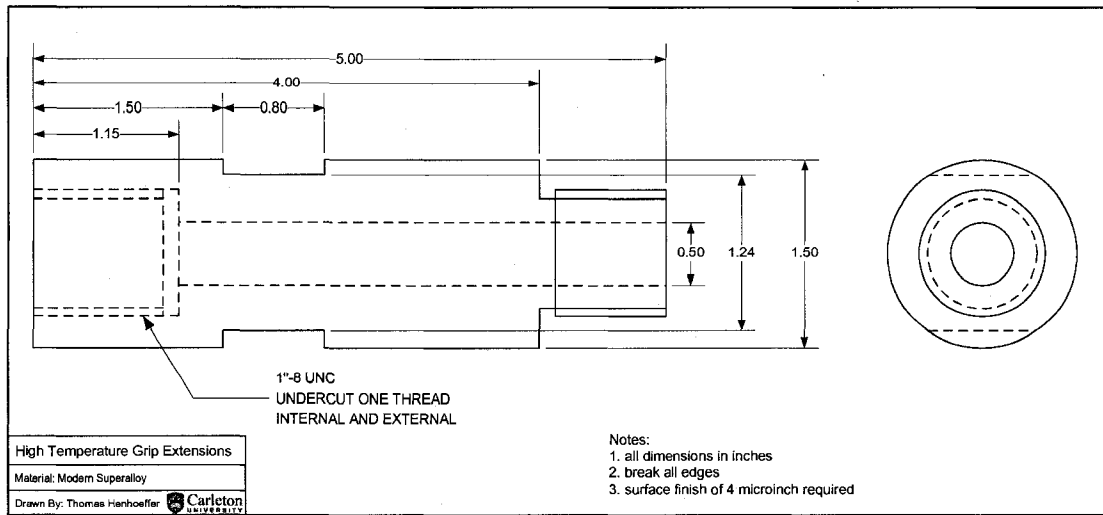
- [60] Li, W., Jin, T., Sun, X. F., Guo, Y., Guan, H. R., & Hu, Z. Q. (2003). Study of Ni-Cr-Co-W-Mo-B Interlayer Alloy and its Bonding Behaviour for a Ni-Base Single Crystal Superalloy. *Scripta Materiala*, 48, 1283-1288.
- [61] Idowu, O. A., Richards, N. L., & Chaturvedi, M. C. (2005). Effect of Bonding Temperature on Isothermal Solidification Rate During Transient Liquid Phase bonding of Inconel 738LC Superalloy. *Materials Science and Engineering A*, 397, 98-112.
- [62] Artemev, A. (Fall 2006). MAAE 4102 - Materials Strength and Fracture. Ottawa: Department of Mechanical and Aerospace Engineering, Carleton University.
- [63] Standard Practice for Strain-Controlled Fatigue Testing. (n.d.). ASTM International.
- [64] Ohsasa, K., Shinmura, T., & Narita, T. (1999). Numerical Modeling of the Transient Liquid Phase Bonding Process of Ni Using Ni-B-Cr Ternary Filler Metal. *Journal of Phase Equilibria*, 20, 199-206.
- [65] Idowu, O. A., Richards, N. L., & Chaturvedi, M. C. (2004). Effect of Gap Size and Process Parameters on Diffusion Brazing of Inconel 738. *Science and Technology of Welding and Joining*, 9 (3), 209-220.
- [66] Heikenheimo, L., Laukkanen, A., & Veivo, J. (2005). Joint Characterization for Repair Brazing of Superalloys. *Welding in the World*, 49 (5-6), 5-12.
- [67] Klopp, W. D. (1999). *Aerospace Structural Materials Handbook*. In W. F. Brown, Jr., & C. Gibson (Eds.). West Lafayette: Purdue University.

## **Appendix A: Part Drawings**

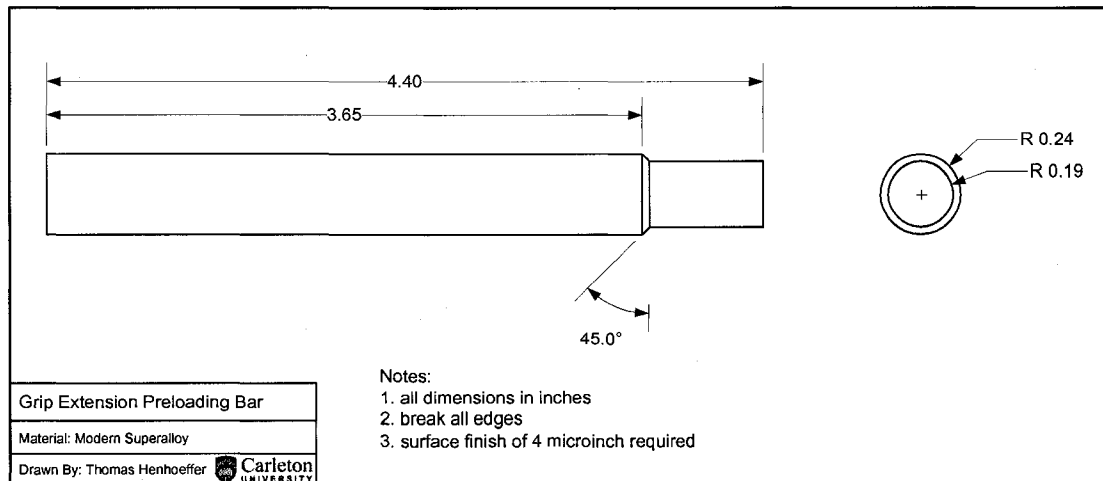
**Mechanical Test Coupon**



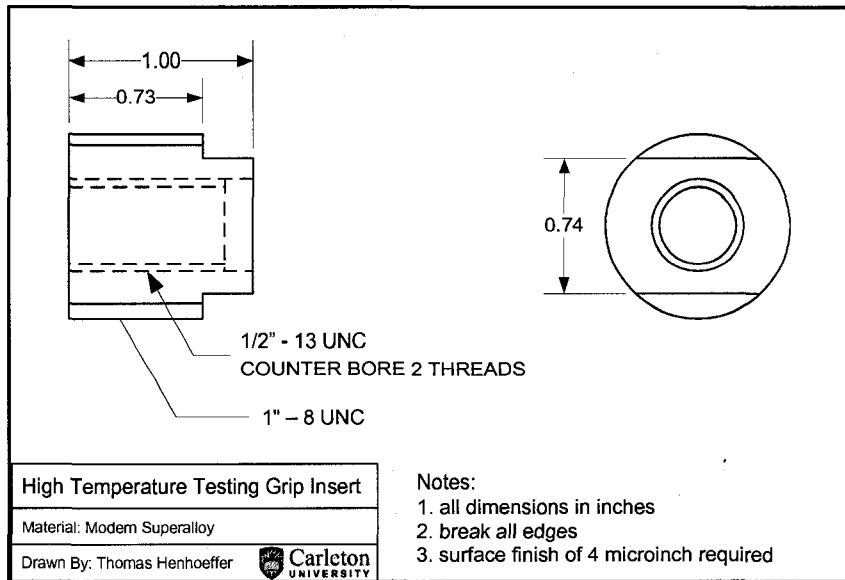
## Grip Extension



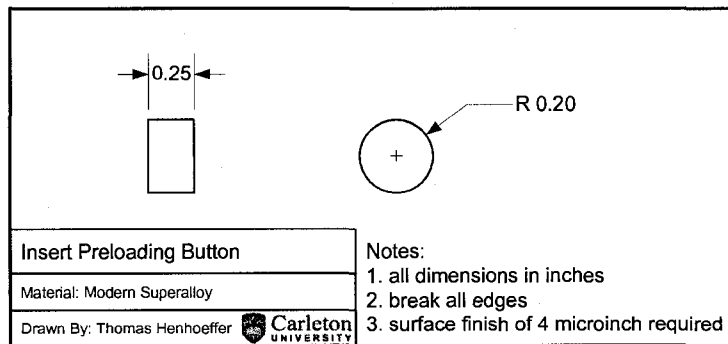
## Preload Bar



## Insert



## Preload Button



## **Appendix B: Extensometer Calibration Report**

Equipment	Model Number	Serial Number
Transducer	632.41C-11	318
Controller/Conditioner	N/A	N/A
Readout Device	MTS TestStar II	N/A

Length	
Range	10%
Travel	1.20 mm

Gauge	12.00 mm
-------	----------

Calibration Performed By: \_\_\_\_\_ Scott Yandt and Thomas Henhoeffler \_\_\_\_\_

### Calibration Equipment

Device Description \_\_ Mitutoyo extensometer calibration device \_\_\_\_\_

Model \_\_\_\_\_ Number model 3590 \_\_\_\_\_ Serial Number \_\_\_\_\_ N/A \_\_\_\_\_

### Calibration Data

Percent Range	Strain mm/mm	Disp. mm	RUN #1		RUN #2	
			Indicated Reading	Error % of Reading	Indicated Reading	Error % of Reading
100	0.1	1.2	0.10004	0.04	0.09993	-0.07
90	0.09	1.08	0.09007	0.08	0.09001	0.01
80	0.08	0.96	0.08005	0.06	0.08000	0.00
70	0.07	0.84	0.07013	0.19	0.07008	0.11
60	0.06	0.72	0.06007	0.12	0.06011	0.18
50	0.05	0.6	0.05007	0.14	0.05002	0.04
40	0.04	0.48	0.04010	0.25	0.04008	0.20
30	0.03	0.36	0.03008	0.27	0.03006	0.20
20	0.02	0.24	0.02003	0.15	0.02001	0.05
10	0.01	0.12	0.01006	0.60	0.01003	0.30
0	0	0	-0.00001	--	-0.00012	--
0	0	0	0.00016	--	0.00009	--
-10	-0.01	-0.12	-0.01000	0.00	-0.00998	-0.20
-20	-0.02	-0.24	-0.01999	-0.05	-0.02000	0.00
-30	-0.03	-0.36	-0.02996	-0.13	-0.03000	0.00
-40	-0.04	-0.48	-0.03997	-0.08	-0.04001	0.02
-50	-0.05	-0.6	-0.05001	0.02	-0.04999	-0.02
-60	-0.06	-0.72	-0.05998	-0.03	-0.06001	0.02
-70	-0.07	-0.84	-0.06998	-0.03	-0.06996	-0.06
-80	-0.08	-0.96	-0.07988	-0.15	-0.07996	-0.05
-90	-0.09	-1.08	-0.08985	-0.17	-0.08993	-0.08
-100	-0.1	-1.2	-0.09979	-0.21	-0.09981	-0.19

#### GAIN:

PREAMP                    260  
POSTAMP                   4.617  
TOTAL                        1200.4  
EXCITATION                9.5001  
DELTAK                     1.0002  
BALANCE OPTION         0  
FINE ZERO                 -0.1678